Swansea University
Prifysgol Abertawe

DOCTOR OF PHILOSOPHY

SWANSEA UNIVERSITY

FACULTY OF SCIENCE AND ENGINEERING

Ordering and Encapsulation in Viscoelastic Microfluidic Flows

---

Supervisor:
Dr Francesco Del Giudice

Author:
Anoshanth Jeyasountharan

Secondary Supervisor:
Prof Rhodri Williams

March 2, 2023

Abstract

Viscoelastic polymer solutions have been employed as suspending liquids for a myriad of microfluidic applications including particle or cell focusing and sorting. Very recently viscoelastic liquids have been shown to drive the formation of strings of equally spaced particles called "particle trains”. The formation of “particle trains” may have unprecedented benefits on important biomedical applications. For example single cell analysis benefit from encapsulation of a single cell or particle in a droplet for high throughput decoding and sequencing of cellular information. In flow cytometry particle or cell train formation is crucial for analysing their properties without interference from overlapping cells or particles. To date, limited experimental studies are available on viscoelastic particle train formation. In Chapter 4 of the thesis, we demonstrate that a viscoelastic shear thinning aqueous 0.1 wt% xanthan gum XG solution drives the self-assembly of particle trains on channel centerline in a serpentine microfluidic device. In addition, to account for the fluctuations in the number of flowing particles, we introduced the concept of local particle concentration, observing that an increase in local particle concentration led to an increase multi-particle string formation. Thereafter, we simplified the microfluidic configuration to drastically reduce multi-particle string formation. In Chapter 5, we successfully employed a microfluidic device with sixteen-trapezoidal elements to reduce multi-particle string formation down to 5 % and studied the effect of confinement ratio on ordering dynamics of particles in 0.2 wt% XG, where larger confinement ratios led to self-assembly at shorter distances. Subsequently, in Chapter 6 we studied the particle encapsulation in a T-junction microfluidic device, using a non-Newtonian viscoelastic 0.1 wt% hyaluronic acid HA solution in phosphate buffer saline as suspending liquid. We first studied the non-Newtonian droplet formation mechanisms, finding that the data for the normalised droplet length scaled as the Newtonian ones. We then performed viscoelastic encapsulation experiments and identified experimental conditions for which the single encapsulation efficiency was larger than the stochastic limit predicted by the Poisson statistics. Overall, our work provides insights into fluid characteristics, experimental conditions and microfluidic devices required to form particle trains and to encapsulate particles in droplets.

Declarations and Statements

- This work has not previously been accepted in substance for any degree and is not being concurrently submitted in candidature for any degree.

Signed: Anoshanth Jeyasountharan
Date: 29/09/2022

- This thesis is the result of my own investigations, except where otherwise stated. Other sources are acknowledged by footnotes giving explicit references. A bibliography is appended.

Signed: Anoshanth Jeyasountharan
Date: 29/09/2022

- I hereby give consent for my thesis, if accepted, to be available for photocopying and for interlibrary loan, and for the title and summary to be made available to outside organisations.

Signed: Anoshanth Jeyasountharan
Date: 29/09/2022

- The University's ethical procedures have been followed and, where appropriate, that ethical approval has been granted.

Signed: Anoshanth Jeyasountharan
Date: 29/09/2022

Acknowledgements

I would like to thank my parents, partner and supervisor for all the help and support during the PhD.

Contents

List of Figures

List of Tables

Abbreviations

GPC: Gas-phase chromatography
HPLC: High-pressure liquid chromatography
CTCs: Circulating tumour cells
HSCs: Hematopoietic stem cells
DNA: Deoxyribonucleic acid
SAV: Surface area to volume
3D: 3 Dimensional
PVP: Poly(vinyl pyrrolidone)
PEO: Polyethylene oxide
PCR:Polymerase-chain-reaction
PS: Polystyrene
XG: Xanthan gum
SAV: Surface area to volume ratio
mRNA: Messenger ribonucleic acid
RT: Reverse Transcription
Ca: Capillary number
γ: Interfacial tension
μ_d: Dynamic viscosity of dispersed phase μ_c: Dynamic viscosity of continuous phase
Q_d: Dispersed phase flow rate
Q_c: Continuous phase flow rate
W: Channel width
Ca: Capillary number
F_W: Wall induced lift force
F_S: Shear gradient lift force

Re: Reynolds number
N_1: First normal stress, difference between the streamwise normal stress σ_{xx} and the transverse normal stress σ_{yy}
N_2: Second normal stress, difference between both transverse normal stress components, namely σ_{yy} and σ_{zz}
F_E: Elastic force
F_{ST}: Shear thinning force
De_{cr}: Deborah number, defined as the ratio between the fluid and flow characteristic time
De_{cr}: Critical Deborah number
s: Initial distance
s_{cr}: Critical distance value
s_1 and s_2: Two relative distances between consecutive particles
El: Elasticity Number
λ: Longest relaxation time
D: Channel diameter
$Dean$: Dean number
Q: Volumetric flow rate
ρ: Fluid density
η: Shear viscosity
d: Particle diameter
H: Channel height
ϕ_l: Local particle concentration
L_f: Length of the observation window
N_p: Number of particles
η_∞: Infinite shear viscosity
η_0:Zero shear viscosity
$\dot{\gamma}$: Shear rate
m:Factor that modulates the transition between the constant and shear thinning region
G_{min}: Minimum value of modulus that is detectable by the rheometer
λ_{min}: Minimum value of viscosity that is detectable by the rheometer
T_{min}: Minimum detectable torque
β: Confinement ratio
ΔP : Imposed pressure drop
S^*: Normalized distance between particles
f_d: Frequency of droplet formation.
f_p: Frequency of particles arriving at the encapsulation site.

Chapter 1

Introduction

Microfluidics is a field that is focused on the manipulation of fluids and other micrometer sized objects such as cells and particles in micro channels. Micro channels are miniaturized devices with specially designed structures that have micro scale dimensions of 10 to 100 μm [1]. The orgin of microfluidics in chemical analysis stems from the need to minimise sample volume and increase analysis speed in analytical systems. Analytical methods such as gas-phase chromatography GPC, high-pressure liquid chromatography HPLC [2] are commonly used to separate chemical components in mixtures. In the late 1970s, "Micro-total analysis systems" were developed and incorporated into HPLC and GPC systems with benefits of low sample volumes and increased throughput [3]. In recent years, microfluidic technology has progressed towards analysis in fields ranging from biomedical engineering to medicine, such microfluidic devices employed for analysis are termed as "Lab-On-Chip" devices [4, 5, 6]. For instance, isolating, sorting, analysing cells or particles from heterogeneous mixtures represents a vital challenge in fields such as biology, biotechnology, and medicine [4, 7, 8]. In addition, cell or particle isolation and sorting is often used to obtain a homogeneous samples to improve sensitivity of end-point techniques that are used to measure the properties of target cells or particles such as flow cytometry [9], bio-marker detection and analysis [10]. In diagnostics isolation and analysis of rare target cells such as circulating tumour cells CTCs, and hematopoietic stem cells HSCs are vital for identifying optimal treatment methods [11, 12, 13]. Microfluidic technology also extends to molecular biology for applications involving molecular sequencing such as Deoxyribonucleic acid DNA extraction, purification, amplification, detection and analysis [14, 15]. The wide array of applications involving microfluidic technology results from miniaturised systems with large surface area to volume SAV ratio, which requires a small volume of sample or reagents to carry out analysis with a high resolution and sensitivity, where the analysis times are much shorter compared to conventional analytical laboratory techniques [16, 17, 18, 19].

The precise control of particle and cell flow trajectories is a flourishing field in microfluidics and has led to novel developments in fields, ranging from biomedicine [20] to tissue engineering [21, 22]. Biomedicine related particle and cell trajectory manipulation allows 3D particle focusing, which is achieved when particles lie on a specific position over the channel cross-section. 3D focusing is an essential component of flow cytometry for highly efficient particle or cell detection, separation [23], encapsulation (where particles or cells are confined in droplets) [24] and ordering (particles or cells are equally spaced along the flow direction) [25, 26, 27]. In tissue engineering, cell architecture can be generated by microfluidic networks embedded directly within the cell-seeded biomaterials, which is essential for 3D scaffold characterisation [21]. As mentioned previously, programmable control and manipulation of particles at a micro scale often provides major advantages over the conventional macro scale systems i.e. high surface area to volume ratio. This often leads to an enhanced mass transfer process, which improves the rate and feasibility of a reaction. In microfluidic systems, cell or particle ordering and separation according to biophysical parameters such as size, density, shape and deformability leads to highly precise particle ordering and separation mechanisms. This enables a systematic encapsulation of particles or cells in a confined manner for downstream applications such as micro flow cytometry. Particle flow can be manipulated with the use of active techniques that require external forces generated by electric, magnetic, acoustic fields, or sheath flows [28]. These methods often require highly functionalized particles that are responsive to the external fields and the strength of the external field may damage delicate particles or cells. In recent years, a more general solution has been proposed for this problem, which involves the use of passive techniques to manipulate particles or cells without damaging particles or delicate cells (see Figure 1.1 for more details) [29]. Unlike active techniques, passive techniques mainly rely on biophysical properties of cells or particles, such as the size, density, shape and deformability to manipulate their trajectories in microfluidic flow [30]. Inertial microfluidics is an emerging field in passive microfluidics that utilises inertial forces and secondary flow (minor flow perpendicular to the primary flow) to manipulate particle and cell trajectories [29, 31, 32, 33, 34, 35, 36, 37, 38]. Inertial microfluidics often employ large volumetric flow rates to manipulate the flow of particles and cells in an intermediate Reynolds number range $1 < \mathrm{Re} < 100$ [39] (refer to equation 3.3). High volumetric flow rates and large shear gradients can damage the structures of delicate cells [40]. In addition, complex geometry structures are required to couple inertial forces with geometry-induced secondary flows to manipulate particle and cell trajectories [41, 42, 43]. However, such complex structures are not compatible with downstream applications such as single cell analysis systems that benefit from simple microfluidic structures for efficient encapsulation of particles and cells in a single droplet [44]. In recent times, micro channels designed to focus, concentrate, or separate particles suspended in viscoelastic liquids are becoming a common form of passive microfluidic technique [45]. This field of microfluidics is often referred to as viscoelastic microfluidics. Viscoelastic fluids are non-Newtonian by nature with complex microstructures, which gives rise to unique properties such as: shear thinning or thickening phenomena where fluid viscosity decreases or increases as a function of shear rate [46]; cross flow migration, where neutrally buoyant particles suspended in viscoelastic fluids migrate laterally across the streamlines of the main flow [47]. The unique behaviour of viscoelastic fluids is attributed to their rheological properties, which consist of both viscous and elastic components [48]. More recently, the addition of polymers to aqueous suspensions promote viscoelastic-induced migration of suspended particles towards the centerline in straight micro channels due to viscoelastic forces acting on the particles [49, 50, 51, 52, 53, 54]. To date, very few works have focused on longitudinal ordering of particles in viscoelastic liquids. Especially, on the formation of particle trains (strings of equally spaced particles) in viscoelastic flows. Particle or cell train formation is crucial for biomedical applications such as micro flow cytometry, single cell analysis and encapsulation. For example, in micro flow cytometry particle train formation on channel centerline will enable efficient data acquisition of cell properties without the presence overlapping cells [40]. In single cell analysis, particle train formation is important to encapsulate and compartmentalize an individual particle or cell in a droplet for high-throughput sequencing methods such as Deoxyribonucleic acid DNA and Ribonucleic acid RNA sequencing [55, 56]. Shear thinning liquids have always been considered as detrimental for particle train formation, since particles tend to migrate towards the channel walls [57, 58, 59]. Very recently, Del Giudice et al in 2017 demonstrated that particles can be aligned on the centerline of a straight square shaped micro channel in a shear thinning liquid, by increasing confinement ratio (the ratio of the particle size to the channel height) $\beta \geq 0.2$ [59]. Since then few studies have employed shear thinning fluids to achieve particle train formation on channel centerline [27]. Particle train formation in shear thinning fluid offers several advantages over inertial microfluidics, such as particles trains form at channel centerline in shear thinning fluids as opposed to multi equilibrium position observed in inertial microfluidics [60]. In shear thinning fluids, the velocity profile in a micro channel is more flat around the centerline compared to the parabolic one observed in Newtonian liquids [30, 59]. Thus, smaller shear stresses act on objects flowing around the channel centerline which has advantages when processing delicate cells i.e. cells will not be damaged. Further investigations on viscoelastic (shear thinning) mediated particle train formation is a logical step in understanding the effect of shear thinning fluids on parameters such as inter particle distance (distance between adjacent particles) in particle trains. These investigations are crucial for further integrating viscoelastic microfluidics in biomedical applications such as micro flow cytometry and single cell analysis technologies such as drop sequencing [61].

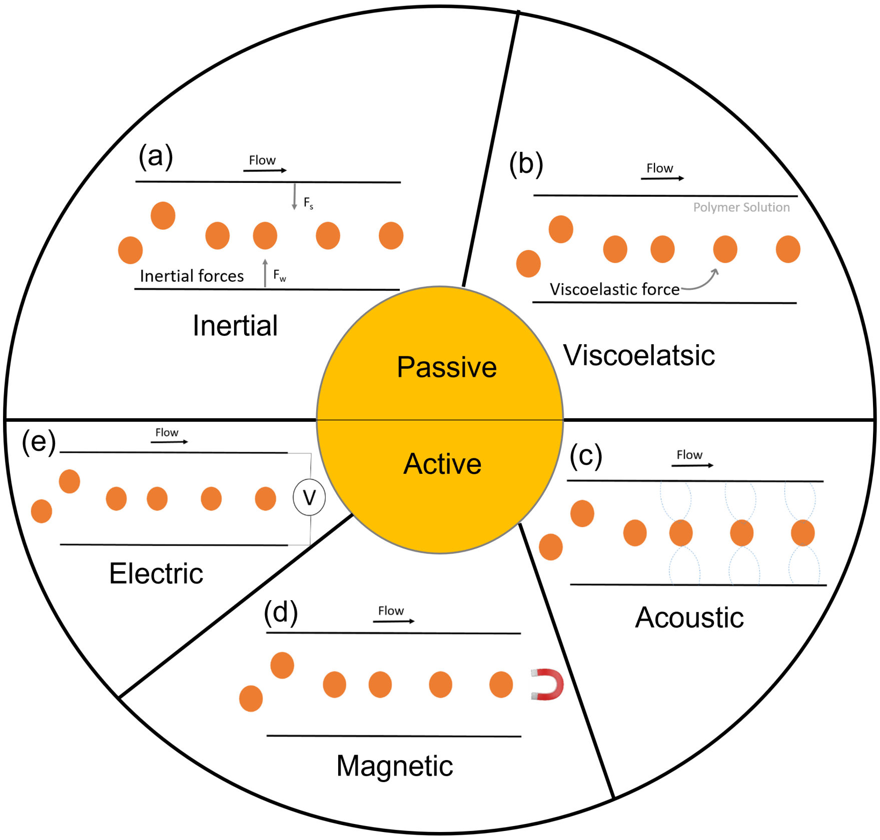

Figure 1.1: Schematic representation of active and passive methods employed in microfluidics to manipulate particle and cell trajectories. (a) Inertial microfluidics has been successfully used to manipulate particle or cell positions in microfluidic channels. Inertial microfluidics has been mainly employed for cell separation [62], sorting [41], rare cell (e.g. circulating tumour cells isolation [42]). (b) Viscoelastic microfluidics is often used in applications involving particle or cell focusing i.e. particles or cells lie on a single plane [63] and separation [64]. (c) Acoustic microfluidic devices employ sound waves to control particle and cell trajectories. It has been used to separate leukocytes, red blood cells and platelets [65]. (d) Magnetic fields have been used to control particles or cells in microfluidic channel by external magnets. Applications include: magnetic cell sorting i.e. assembly of cells into linear arrangements [66]. Continuous flow separation of cells (e.g. continuous separation of erythrocytes and leukocytes from the whole blood) [67]. To form three dimensional 3D cellular assemblies, to guide single cells or 3D building blocks into a desired pattern [68]. (e) Electric field mediated microfluidics has been used to manipulate cells through the process of Electrotaxis, where cells are mediated by an external electric field. Such applications involve separating T-lymphocytes from human peripheral blood [69], controlling the migration of cells by an applied electric field in a microfluidic device [70, 71].

1.1 Thesis aim: Viscoelastic particle train formation in microfluidic flows using a xanthan gum

Overall, existing studies have failed to identify and solve key limitations in shear thinning mediated particle train formation: (1) formation of particle trains in shear thinning fluids other than hyaluronic acid [27]; (2) the relevance of particle concentration fluctuations in microfluidic devices in the context of particle train formation, which is a widely present issue in microfluidics [31]; (3) approaches to reduce particle aggregate formation in flow i.e. by simplifying the microfluidic configuration, which may lead to a larger portfolio of applications in biomedical engineering. For example, flow cytometry [72], cell or particle separation [73] and cell or particle encapsulations [74]. Motivated by these limitations, in Chapter 4, we employed aqueous solution of viscoelastic shear thinning xanthan gum XG to successfully form particle trains on channel centerline in hydrophilic serpentine microchannel. Based on previous works, we choose 0.1 wt% XG in deionized water as the lead suspending liquid due to: its strong shear thinning properties at relatively low mass concentrations of the polymer (meaning smaller zero-shear viscosity values); low cost compared to other polymers such as hyaluronic acid; recent interest about using XG for different microfluidic applications based on biocomapability [75]. We also introduced the concept of local particle concentration in an attempt to clarify the effect of particle concentration on train formation as if there were no concentration fluctuations. As mentioned in previous works, we also observed the formation of doublets and triplets of attached particles that disturbed the continuity of train formation. Thus, we showed that a simplified microfluidic device involving the least number of connections between the reservoir and the microfluidic device led to the formation of a more uniform train with minimal doublet formation.

1.2 Thesis aim: Microfluidic device to reduce multi-particle string formation and self-assemble particles in microfluidic flow

Based on our findings from Chapter 4, in Chapter 5 we experimentally demonstrated that a microfluidic device made of a series of elements with trapezoidal shapes was capable of significantly reducing the amount of particle aggregates in flow, thus leading to a more uniform particle train without the need to simplify the microfluidic configuration. In addition, we experimentally elucidated the effect of confinement ratio on the self-assembly dynamics of particle trains in viscoelastic liquids flowing in a straight micro channel. Here we employed two different sized particles to manipulate

β, namely particles with diameters of 20 μm and 45 μm corresponding to the β values of 0.2 and 0.45 suspended in 0.2 wt% XG.

1.3 Thesis aim: Viscoelastic droplet generation and particle encapsulation in a T-junction microfluidic device

In Chapter 6, we employed 0.1 wt% hyaluronic acid HA solution in PBS to study the viscoelastic encapsulation of particles in a T-junction microfluidic device. At variance with standard T-junction devices, our microfluidic device featured the addition of several trapezoidal elements to break the particle aggregates (see Figure 2.6c). We employed HA as the suspending liquid rather than xanthan gum because we observed that xanthan gum solutions tend to degrade more easily than the hyaluronic acid. In Chapter 6, we first studied the viscoelastic droplet formation mechanism for both Newtonian (PBS) and non-Newtonian (HA) cases and then the viscoelastic encapsulation of particles at various dispersed to continuous phase flow rate ratios. Finally, we identified some optimal experimental conditions for which the single particle encapsulation efficiency was larger than the Poisson limit. Overall, our work has relevance in controlled encapsulation of particles or cells in T-junction devices to optimise single cell analysis applications such as Drop sequencing [76].

Chapter 2

State of the Art

2.1 The use of Inertial Microfluidics to manipulate particles

Inertial microfluidics has been successfully employed as a passive technique to manipulate particle trajectories with inertial forces in microfluidic flow [77]. The effect of inertial forces on particles and cells lead to migration along a specific streamline and establishes several equilibrium positions across the channel cross section [31, 72]. The exact underlying mechanism behind inertial phenomena is still unclear. It is widely accepted that two opposing lateral lift forces are responsible: (1) the wall lift force, F_W, where flow field interaction between the suspended particles and the adjacent walls, repel the particles away from the wall; (2) the shear gradient lift force F_S, that arises due to the curved fluid velocity profile, where shear gradient is minimal at channel centerline (see Figure 2.1). Thus, particles migrate towards the channel wall [60]. The balance between inertial lift forces results in a dynamic equilibrium position within the channel cross section [78]. Parameters that influence the balance between such inertial forces include channel geometry [60], Reynolds number [78], particle shape [79], and cell deformability [80].

A pioneering work by Segre and Silberberg in 1961 reported that particles with diameters of $0.32 < d < 1.7$ mm suspended in 1,3-butanediol and water mixture displayed regularly spaced ordered structures in a cylindrical pipe with ($\sim$1 cm diameter) and found that particles migrated to an annulus between the pipe centerline and the wall [81]. Many years later, Di Carlo and colleagues investigated the formation of ordered particle structures in inertial flow. They attributed particle migration to inertial lift forces acting on particles, which led to the particles being focused on the channel centerline i.e. particles lie on a specific plane along the flow direction. They also employed symmetric and asymmetric channel geometries to provide additional inertial forces and achieved continuous streams of strings of equally spaced particle structures termed as particle trains [29]. Since then, inertial flow of dilute suspensions has been used to focus particles and form ordered particle structures at multiple equilibrium positions [29, 31, 32, 33, 34, 35, 36, 37, 38], where alterations in channel geometry and fluid inertia led to multiple streams of ordered structures in flow [29, 31, 82]. The formation of these structures was elucidated by the coupled effects of inertial forces and channel geometry on particle-particle hydrodynamic interactions [36, 43, 83]. Although, these studies reported the formation of multiple streams of particle trains [29, 81]. They did not investigate how the distance between adjacent particle in a single stream, that is the inter-particle distance can be manipulated. Controlling the inter-particle distance is important for understanding the hydrodynamic interactions between particles [49]. For instance, manipulating the inter-particle distance between adjacent particles is vital for the encapsulation of particles or cells in droplets for applications such as Drop-sequencing [84] and micro flow cytometry [74], where deterministic encapsulation with 100% efficiency is critical for efficient data acquisition and analysis. Matas and colleagues [85] showed that 425 and 825 μm particle trains i.e. strings of equally spaced particles can be formed on multiple streamlines in 8 and 14 mm internal diameter tubes [85]. Whereby, an increase in Reynolds number Re led to an increase in the size of the reversing flow regions, which led to a monotonic reduction of the average inter-particle spacing in trains. Complete understanding of this inertial phenomenon on inter-particle distance remains currently out of reach. In addition, previous works show that inertial forces can be manipulated to form particle trains in complex channel structures [81, 85, 86], microfluidic applications such as micro flow cytometry require simple straight micro channels for endpoint analysis, where lasers independently acquire critical information from flowing particles or cells. However, under inertial flow particles are focused to multi equilibrium positions depending on the channel geometry, as displayed in Figure 2.1c [87]. Particles or cells focused near the channel walls display high rotations and may be affected by large shear gradient forces. These forces may damage the cells and negatively impact microfluidic applications [88]. To rectify the problem of multi-equilibrium positions, it is important to form particle trains at a single equilibrium position i.e. at channel centerline, where particle rotation and local shear gradients are minimal (see Figure 2.1b) [89].

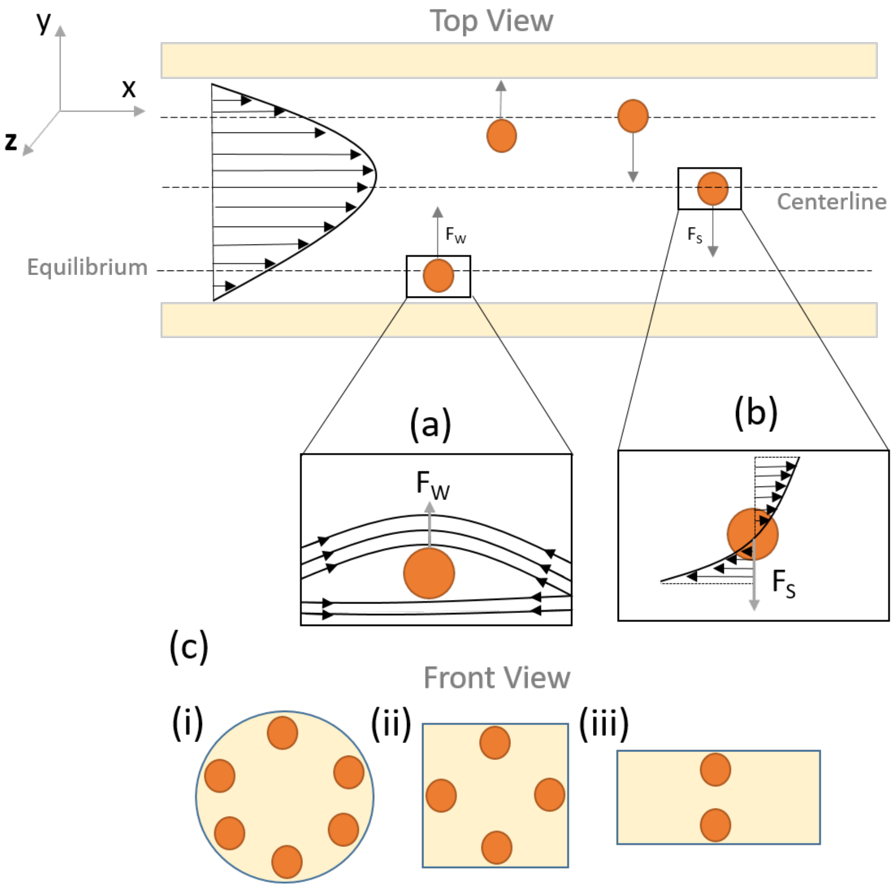

Figure 2.1: Inertial lift forces acting particles and the equilibrium position of particles in micro channels with various cross sections. (a) Wall induced lift force F_W arises from the asymmetry in the flow field around the particle due to the presence of a channel wall, the direction of the particle migration is towards the channel centerline (b) Shear gradient induced lift force F_S arising from a curved Poiseuille velocity profile, where shear-gradient is minimal in the centerline, particles migrate towards the wall. Equilibrium position of particles in micro channels with: (i) circular cross-section, (ii) square cross-section, and (iii) rectangular cross-section [78, 85]. Flow is along the x-direction and shear is in y-direction.

2.1.1 Applications of Inertial Microfluidics

Inertial microfluidics has emerged as a promising field in recent years, due to its several advantages, including high-throughput processing, precise manipulation, and cost-effectiveness [83]. The primary focus of inertial microfluidics has been on particle and cell manipulation applications in microfluidic devices. The use of inertial microfluidics has enabled the isolation, alignment and separation of targeted cells and particles. Size-based particle separation in microfluidic system has been developed based on the principles of inertial migration [29, 90]. The precise alignment of particles or cells is a key requirement for biological detection systems, such as on-chip flow cytometry. In these systems, particles or cells are positioned near a detector and aligned along a specific path for analysis of their properties. The achievement of 3D focusing, where particles or cells lie on a specific plane, is crucial for precise alignment. Conventionally, a sheath flow is used to surround the sample flow for 3D focusing, resulting in a complex setup with multiple sheath flows. However, the use of inertial microfluidics enables sheathless 3D focusing, which provides a simpler setup that can be easily scaled. Inertial microfluidics has been applied in on-chip flow cytometry, enabling high-throughput analysis at higher flow rates [40, 72, 90, 91, 92]. Inertial microfluidics has been widely used for particle separation based on particle size and shape. In inertial microfluidics, the separation and sorting of particles are generally based on the effect of inertial force on particles, where particles tend to occupy different equilibrium positions based on the effect of inertial forces acting on the particles, which leads to size-based separation. For example, size-based separation has been employed to filter bacteria from dilute blood with $>$80% removal of pathogenic bacteria from blood [93], for isolating platelets and blood plasma [94]. Di Carlo et al used asymmetric channels with curves to achieve differential inertial focusing for the separation of larger blood cells from platelets. The size of blood cells varied with spherical leukocytes (WBCs) being 7 to 15 μm, red blood cells being 6-8 μm, and platelets being 2 to 4 μm in diameter [95]. Lee et al 2011 used a spiral geometry for size-based fractionation of mammalian cell lines and primary cell bone marrow-derived human mesenchymal stem cells and achieved high-resolution separation of cell populations as a function of cell diameter. The channel had a 500 mm wide section prior to the outlet [96]. In addition, inertial microfluidics has been used for isolating circulating tumour cells from the blood [97]. Shen et al 2014 isolated circulating tumour cells, from a heterogeneous cell population with a $>$ 90% cell recovery [98]. Abdulla et al 2018 employed a microfluidic device consisting of two spiral channels and successfully separated red blood cells, white blood cells and two different types of tumour cells (human lung cancer cells (A549) and human breast cancer cells (MCF-7), where 80.75 % and 73.75% of tumour cells were separated from the blood cells respectively [99]. High throughput inertial focusing can also be combined with single-cell encapsulation technologies, where a single cell or particle is encapsulated in a droplet. This is crucial for analysing and quantifying the genetic make-up of cells using polymerase chain reaction. By synchronising the frequency of cells in the longitudinal direction and the production of droplets, single-cell encapsulation can be optimised. Inertial microfluidics can be used to align particles prior to encapsulation and drastically improve the encapsulation efficiency of single cells in a droplet [74, 100].

2.2 Viscoelastic Microfluidics to manipulate particle trajectories

Viscoelastic microfluidics provides an alternative option to manipulate particle trajectories in microfluidic flow. Recently, the addition of viscoelastic polymer to aqueous suspensions was found to promote transversal migration of suspended particles towards the channel centerline [49, 50, 51, 52]. Viscoelastic microfluidics has been shown to sort/separate particles and cells with sizes smaller than < 1 μm by viscoelastic forces generated in flow. Such as separating/sorting DNA [101], bacteria [102], CTCs [103] and excosomes [104]. While inertial forces tend to drop in magnitude when the diameter of particles decrease below 1 μm [101, 105]. In addition, achieving a single equilibrium position i.e. on the channel centerline is optimal for applications such as flow cytometry, which requires a single line of equally spaced particles or cells to reach the end-point analytic system i.e. laser to avoid cell or particle overlaps [92]. In viscoelastic microfluidics, transversal migration of particles is due to the deformation of viscoelastic polymer chains induced by unequal normal stress differences, which are forces that act perpendicular or normal to flowing the particles [106, 107]. Two unequal normal stress differences arise from three normal stress components [108, 109]. First normal stress difference N_1 is the difference between the streamwise normal stress σ_{xx} and the transverse normal stress σ_{yy}, $N_1 = \sigma_{xx} - \sigma_{yy}$ [110]. It is first normal stress difference that is responsible for the transversal migration of particles and cells in viscoelastic liquids [51]. The second normal stress difference N_2 is the difference between the both transverse normal stresses $N_2 = \sigma_{yy}$ - σ_{zz}, where σ_{yy} and σ_{zz} are the transverse normal stress components [110]. N_2 is an order of magnitude smaller than N_1 and causes secondary flows orthogonal to the flow direction in curved channels [111]. However, in Newtonian fluids, N_1 is zero, as normal stresses are the same in all directions. So there is no transversal migration of particles or cells in Newtonian fluids when inertial forces are negligible [10, 81, 110, 112, 113]. In a pressure driven Poiseuille flow with a curved velocity profile, the elastic force F_E arsing from N_1 transversely drives particles towards the centerline, where shear rate is minimal (Figure 2.2a). In contrast, when fluid shear thinning forces become relevant particles migrate towards the region of high-shear rate i.e. towards the channel walls (Figure 2.2b). In a purley viscoelatsic inertialess flow ($Re \leq 1$), the balance between competing forces, that is either shear thinning and elastic forces leads to a stable equilibrium position near the channel centerline or walls [51, 114, 115]. For instance, when the effect of shear thinning forces become relevant, particles tend to migrate towards the channel wall and defocus, leading to four equilibrium positions near the wall [57]. Numerical simulations have shown that the effect of shear thinning forces on migration of particles in Poiseuille flow depends on parameters such as particle diameter, volumetric flow rate, channel size and geometry [59, 116]. On the contrary, when elastic forces dominate particles focus and migrate towards the channel centerline. This leads to a single equilibrium position on the channel centerline (Figure 2.2) [52, 107]. In addition to the elastic force stemming from unequal normal stress differences, both experimental and numerical studies have demonstrated that the transversal migration of particles suspended in viscoelatsic medium is governed by parameters such as fluid rheology, channel geometry, particle size and volumetric flow rate [50, 51, 52, 53, 58, 117, 118]. Interplay among these parameters results in transversal migration of particles towards the channel centerline or walls. 3D particle focusing occurs when particles are focused along a specific stream i.e. the channel centerline. In the 1960's, Karnis and colleagues observed 3D focusing of particles for sub-millimeter particles suspended in viscolelatsic fluids in circular pipes with millimeter-diameter [106]. Kang et al 2013 demonstrated a particle-focusing phenomenon towards the channel centerline in an extremely dilute DNA solution (5 ppm). They employed a 50 μm diameter tube to achieve 3D focusing [119]. Leshansky and colleagues reported that microfluidics can be used to demonstrate 3D particle focusing induced by fluid viscoelasticity. They employed a shallow micro channel with 8 μm diameter polystyrene particles PS suspended in Poly(vinyl pyrrolidone) PVP solution and observed centerline particle alignment [51]. In contrast, Yang and colleagues demonstrated that in a 50 μm wide square channel, 8 μm diameter particles suspended in 0.01 wt% polyethylene oxide PEO migrated towards the centerline without any particle train formation [50]. Xiang et al, 2018 found that in a spiral channel, particles flowing in solutions with high polymer concentrations 8 wt% PVP were focused at the channel centerline due to fluid elasticity at high polymer concentration. But, with decreasing polymer concentration, the particles migrated to the outer channel walls under the balance of inertial lift forces and elastic forces. Other works on viscoelatsic induced 3D particle focusing recently appeared, where particle migration was always towards the channel centerline at a single equilibrium position [52, 53, 107, 117]. Dominant elastic forces arsing from normal stress differences in viscoelastic suspending liquids lead to transversal migration of particles to a single equilibrium position, termed as viscoelatsic focusing. By employing an elastic liquid with a constant viscosity, a single equilibrium at the channel centerline is achieved. This leads to a 3D focusing mechanism in a simple straight channel without any further complications in the microfluidic device design, where particles or cells with a wider size range (from submicrometer to even nanometer) can be manipulated and focused (Figure 2.2a and Figure 2.3b) [58, 102, 103].

Although, viscoelastic particle focusing allows the manipulation of particle and cells in 3D space, where a centerline equilibrium position is achieved. There is another dimension of particle and cell trajectory manipulation that previous studies have failed to address, namely longitudinal ordering. In longitudinal ordering particle and cells are equally spaced and ordered along the flow direction, as displayed in Figure 2.3c. In microfluidic applications such as micro flow cytometry, equally spaced particle and cells are critical for high-throughput and parallel endpoint analysis of cells and particles properties [40]. Several encapsulation applications involving single-cell analysis benefit particle train formation. For example, controlled sequences of cells in droplets with varied volumes is desirable in multi-volume droplet based digital polymerase-chain-reaction PCR for accurate detection of genetic information in cells [120]. Drop-sequencing for single-cell analysis requires particles and cells to be equally spaced for deterministic encapsulation (100% efficiency) [121], where encapsulation of a target cell or particle in a droplet is significant to analyze genetic material in a highly parallel manner [122]. Particles in viscoelastic liquids become equally spaced at a single equilibrium position on channel centerline, where the shear rate is minimal and the velocity is maximum. This differs with the inertial ordering where particles are either ordered on multiple equilibrium positions, as shown in Figure 2.1c [31, 35] or on a single line near the channel wall where large particle or cell rotation rates may result in blurred images in flow cytometry applications that employ line scan based interrogation [83]. Furthermore, viscoelastic ordering tends to occur in shear thinning liquids. In shear thinning liquids, particles can be aligned on channel centerline at confinement ratio (ratio between particle diameter and channel height) $\beta \geq 0.2$ [59] and the velocity profile in a micro channel is more flat around the centerline compared to the parabolic one observed in Newtonian liquids [10]. This results in smaller shear stresses acting on objects flowing around the channel centerline, which has obvious advantages when processing delicate cells [59]. The capability of viscoelastic fluids to promote particle ordering has been also demonstrated through recent numerical simulations [123], where different values of the particle volume fraction led to different particle structures: at very low volume fractions, the particles did not significantly interact and the distribution of the inter-particle distances did not change from the initial random one; at intermediate values of the particle concentration, the formation of nearly equally spaced trains was observed; at high volume fractions, strings of nearly touching particles were formed. Experimental works, have demonstrated that particle ordering occurs in liquids with shear thinning behaviour i.e. hyaluronic acid on channel centerline [27].

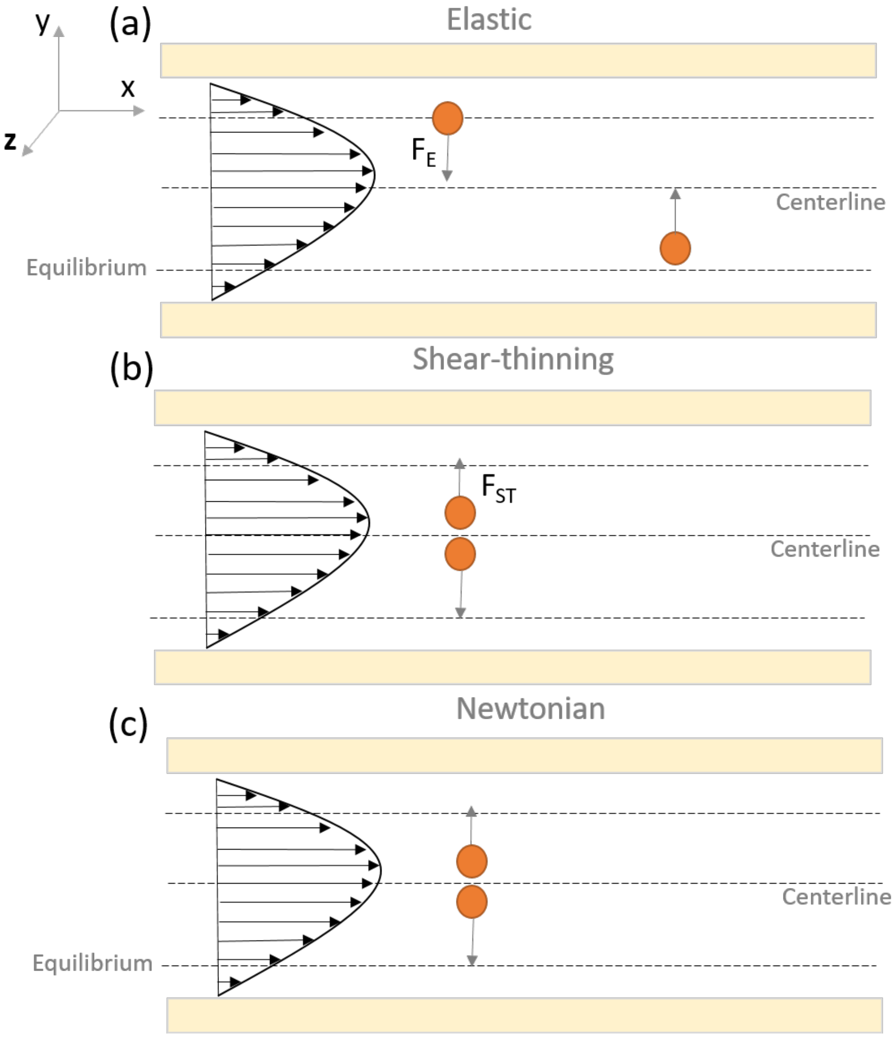

Figure 2.2: Particle migration in a Poiseuille flow with curved velocity profile in an elastic, shear thinning and Newtonian suspending liquids. (a) Particles transversely migrate to a centerline equilibrium position due to elastic force F_E stemming from unequal normal stress differences [51, 110]. (b) Shear thinning force F_{ST} leads to outward migration of particles towards the channel corners [59]. (c) Particles migrate towards the wall in Newtonian fluids, where inertial forces become relevant [10, 81].

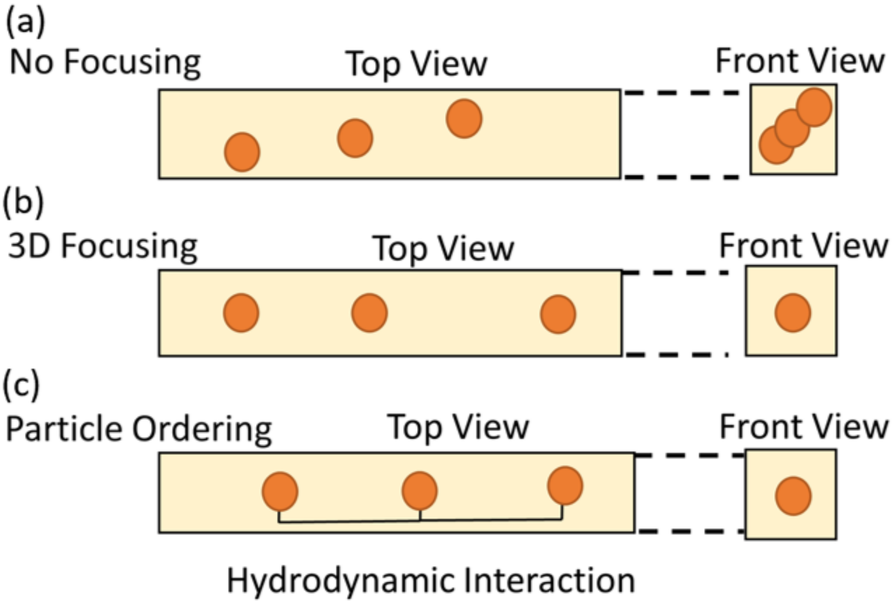

Figure 2.3: Degree of particle trajectory manipulation in a simple rectangular micro channel. (a) No focusing, where particles do not lie on a single plane and are not equally spaced or ordered. (b) 3D focusing, where particles all lie on a single plane i.e. on the channel centerline. (c) 3D focused and equally spaced particle structures, termed as particle trains.

2.2.1 Applications of Viscoelastic microfluidics

Viscoelastic microfluidics has a broad range of applications, including particle or cell focusing and separation in microfluidic devices. Compared to inertial microfluidics, particle manipulation using viscoelastic microfluidics has advantages, such as single-plane particle focusing, which is useful for applications like flow cytometry that require efficient data acquisition of individual particle or cell properties using lasers. Viscoelastic microfluidic systems typically utilize a sheathless system to manipulate particles or cells. Numerous studies have employed viscoelastic fluids to manipulate particle and cell trajectories in microfluidic flows. For example, Nam et al 2012 successfully separated 1 and 5 μm particles suspended in PEO (500 ppm). Due to the elastic force, the 5 μm particles migrated to the centerline, while the 1 μm particles migrated to the channel walls. They also achieved size-dependent separation of blood cells suspended in viscoelastic fluids with a separation efficiency of 99% [64]. They utilized a channel that was 25 mm long and 50 μm wide. Another study by Liu et al 2017 used a viscoelastic microfluidic system to continuously separate exosomes from large extracellular vesicles (EVs) suspended in 0.1 wt% PEO based on their sizes. Exosomes ranged in size from 30 to 200 nm, while large EVs ranged from 200 to 1000 nm. The larger EVs migrated to the centerline, while the smaller exosomes migrated toward the walls. They achieved a recovery rate of over 80% for exosomes using a high-aspect-ratio straight microchannel with a height of 50 μm and a width of 20 μm [104]. Liu et al 2015 used viscoelastic microfluidics to separate MCF-7 (cancer cells) from red blood cells (RBCs) in a straight microchannel with a rectangular cross-section of (100 x 50 μm), and RBCs from Escherichia coli (E. coli) in a microchannel with a different cross-section (40 x 10 μm) [124]. Other applications include manipulations of macromolecules such as DNA to purify or separate DNA for downstream sequencing processes [101]. Ongoing innovative research in the field of viscoelastic microfluidics is continuously offering benefits to industries such as biology and medicine. Particularly, the utilization of simple viscoelastic microfluidic systems to manipulate small cells or particles in biological fluids for various applications provides numerous advantages and is an area that is continuously being developed.

2.3 Particle train formation in Viscoelastic liquids

The next logical step in viscoelastic microfluidics is to achieve equally spaced particle or cell trains on channel centerline. Potential existence of viscoelastic particle trains was first theorized in a numerical simulation by D'Avino et al, 2013 [49]. They employed numerical simulations on pairs and triplets of particles, and demonstrated that particles experienced either an attractive or repulsive forces depending on the flow conditions and the initial distance between consecutive particles [49]. They suggested that repulsion dynamics between consecutive particles in a multi-particle system leads to the formation of particle trains. Thereafter, the first experimental work by Del Giudice and colleagues in 2018 demonstrated that in a square-shaped glass microchannel with a height of 100 μm, PS particles with a diameter of 20 μm, suspended in shear thinning 1 wt% hyaluronic acid biopolymer transversely migrated to the centerline [125] and were equally spaced. In their work, a greater fraction of equally spaced particles was observed at high Deborah number *De* (ratio between the time of relaxation and time of observation) $De = 31$ and $De = 62$, where the volumetric particle concentration was $\phi = 1$ wt%. However, at a lower volumetric particle concentration $\phi = 0.3$ wt%, the inter-particle distances were large, so no particle ordering was observed. It is well established that particle ordering is due to particle-particle hydrodynamic interactions at relatively high particle concentrations [36, 49, 58], which elucidates, the lack of particle ordering observed at low volumetric concentration $\phi = 0.3$ wt%. In contrast, a higher volume concentration $\phi = 1$ wt% led to equally spaced particles with occasional doublet formation [49, 125]. In the same study, strings of attached particles were observed for a fluid with negligible shear thinning features [27]. In brief, the results from Del Giudice and colleagues demonstrated that the shear thinning behaviour of the suspending fluid is essential to achieve particle ordering. However, they did not investigate the dependency of inter-particle distance on forming equally spaced particle trains. In order to achieve equally spaced particle trains, it is logical to control the inter-particle spacing between adjacent particles. We know that particle-particle hydrodynamic interactions can change according to the inter-particle distance, where particle-particle attraction or repulsion occurs at inter-particle distance values lower or higher than the critical inter-particle value [49, 125]. More recently, Liu et al, 2020 employed a microfluidic device to control the spacing between particles. The device consisted of constitutive inverted triangle elements to break particle aggregates followed by a system to uniformly distribute and self-assemble particles. They suspended PS particles with a diameter of 20 μm in 0.3 wt% HA. However, in their work they did not account for particle concentration fluctuations, which is a very common issue observed in viscoelastic microfluidics [31].

Despite the relevance and the potential impact of viscoelastic particle train formation in variety of microfluidic applications, to date, limited experimental works have demonstrated the formation of particle trains in viscoelastic fluids. The only two previously mentioned experimental studies [27, 126] considered aqueous solutions of hyaluronic acid as a suspending fluid. It is still not clear whether different polymer solutions displaying shear thinning features are able to drive the formation of particle trains on channel centerline. Furthermore, hyaluronic acid solution employed by Del Giudice et al, 2018 presented a large zero-shear viscosity, which can cause problems during particle or cell mixing. Employing fluids with high zero-shear viscosity in applications could in fact make particle concentration fluctuations even worse, since particles may not mix well in a highly vicious solution. In addition, very few numerical simulations have demonstrated the effect of viscoelastic liquids on particle ordering. Very recently, numerical simulations by D'Avino and co-workers shed some insights into the underlying dynamics of particle train formation in viscoelastic flow.

For particle pairs, D'Avino and colleagues reported that inter-particle distance is dependent on the initial inter-particle distance, De and fluid rheology [49, 123]. They found that in shear thinning liquids, particles experience a repulsive force that leads to train formation, due to a lowering of critical value s_{cr} below the initial distance s between two particles, so particles repel as displayed in Figure 2.4 and Figure 2.5. For instance, when De is lower than a threshold critical Deborah number De_{cr}, two particles with an initial distance s below s_{cr} experience an attractive force, So particles form aggregates such as doublets and triplets (Figure 2.4a). In contrast, particles with an initial distance of $s > s_{cr}$ experience a repulsive force, which leads to particle train formation. For De values larger than De_{cr}, the two particles only experience a repulsive force at any initial distance (Figure 2.4c and d). The attraction and repulsion dynamics between particle pairs depend on rheological properties of suspending liquid: shear thinning or constant viscosity. Shear thinning suspending liquids led to decreasing critical distance compared with near constant-viscosity liquids (as displayed in Figure 2.4f).

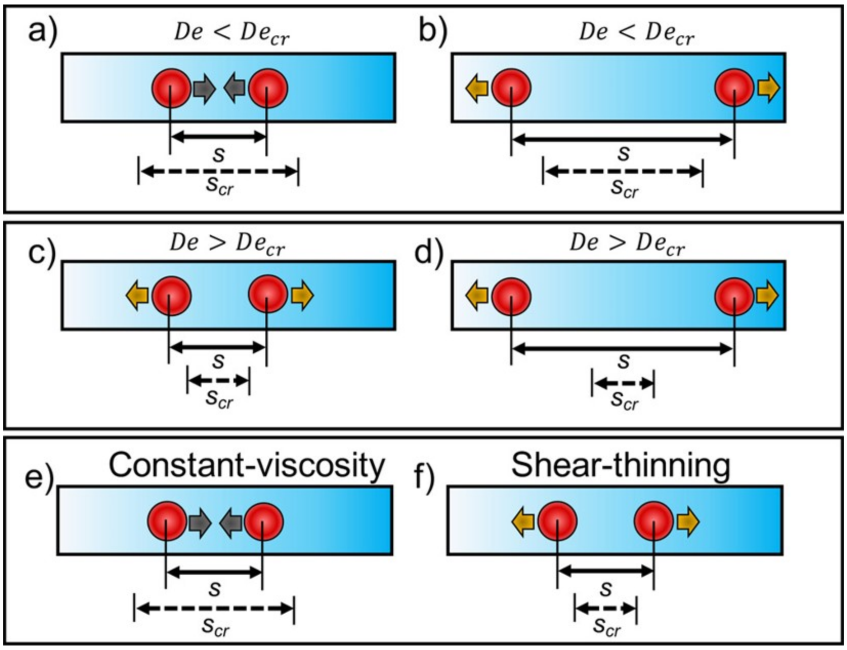

Figure 2.4: Schematic representation of attraction and repulsion dynamics of particle pairs in a viscoelastic suspending liquid based on numerical simulations [49]. (a) For a Deborah number De lower than a threshold De, $De < De_{cr}$ and when initial distance s is lower than critical distance s_{cr}. Particles experience an attractive force and form doublets. (b) For $De < De_{cr}$, and when $s > s_{cr}$. Particles tend to experience a repulsive force and form particle trains. (c) and (d) For $De > De_{cr}$, critical distance $s > s_{cr}$ particles experience a repulsive force. (e) For a suspending liquid with constant-viscosity, $s < s_{cr}$, particles experience an attractive force. (f) In a shear thinning liquid, value of s_{cr} becomes lower than s, $s_{cr} < s$. So particles repel each other. This figure was reprinted from Jeyasountharan et al 2021 [26].

For a system with three aligned particles, attraction or repulsion dynamics depend on the two relative distances between consecutive particles s_1 and s_2 and De number (Figure 2.4). For a De number lower than the critical value De_{cr} and when at least one of the two relative distances is lower than the critical value s_{c_r}, the trailing and middle particle form a pair while the leading particle repels and become isolated (Figure 2.4a). When De is greater than De_{cr}, if the two inter-particle distances s_1 and s_2 are both larger than the critical value s_{cr}. Then, particle repulsion dynamics dominate and trains are formed (Figure 2.4d) [26, 49, 125]. In agreement with D'Avino, very recently, Hu et al, 2022 presented a numerical study featuring the self-assembly dynamics of particle chains in a straight micro channel, observing that viscoelastic liquids with a negligible shear thinning features were responsible for particle chaining [127], in other words multi-particle string formation occurs at constant viscosity liquids. This is in agreement with numerical simulations by D'Avino and colleagues, who found that particles suspended in constant viscosity liquids experience an attractive force due to $s < s_{cr}$, which leads to multi-particle string formation [49, 123]. The first experimental evidence of particle ordering phenomenon reported by Giudice et al 2018, strings of attached particles were instead observed for a fluid with negligible shear thinning features. In general, the formation of particle aggregates tend to be detrimental for the continuity of trains, since doublet or triplet formation can alter the hydrodynamic interactions between particle trains. Such aggregates also have detrimental effect on downstream applications. For example, in flow cytometry aggregated cells or particles may lead to blurred images during data analysis, since flow cytometry requires isolated cells or particles to be focused on channel centerline [9]. In addition, single-cell analysis, which is critical for understanding key changes in single-cell level requires isolated cells to be encapsulated in compartmentalized systems i.e. in droplets to effectively decode cellular information [121]. A potential solution to reduce the number of aggregates in microfluidic flow is to employ microfluidic devices capable of breaking particle aggregates. Recently, Liu et al 2020, proposed a microfluidic device to control the spacing between consecutive particles, which consisted of a first element aimed at breaking particle aggregates followed by a system to make the local concentration of particles more uniform [126]. Despite the relevance of a microfluidic system to form minimal particle aggregates in flow. Very few studies have modified microfluidic device designs to break particle aggregates in flow. For instance, the device employed by Liu et al, 2020 consisted of inlet structures to break particle aggregates based on fluid velocity differences and may be optimal for applications that require a compact microfluidic device set-ups. For example Drop-sequencing, which requires isolated cells to be encapsulated in droplets (with 100% efficiency) for single-cell analysis [121].

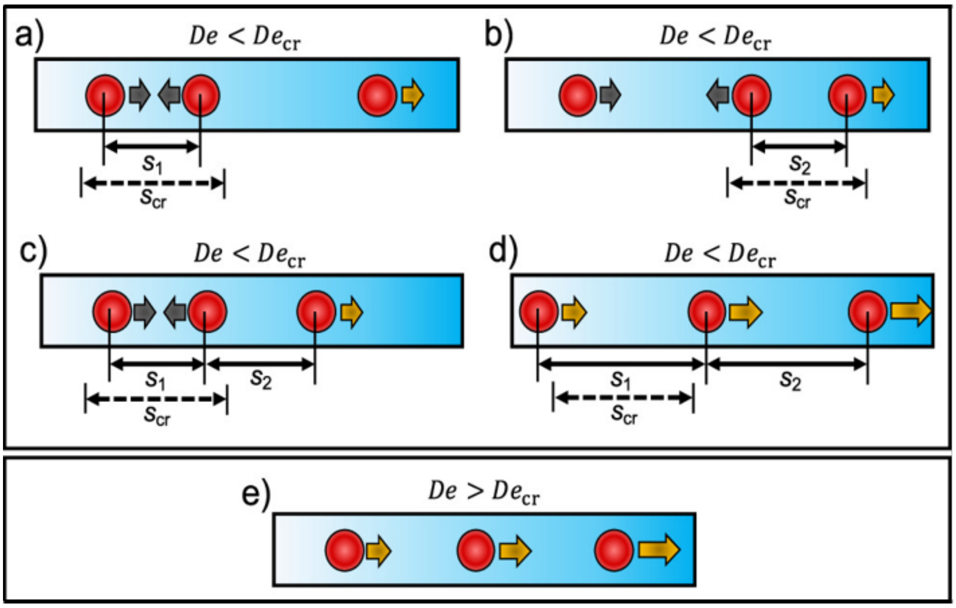

Figure 2.5: Schematic representation of attraction and repulsion dynamics between three flowing particles suspended in a viscoelastic liquid based on the numerical simulation results by D'Avino et al, 2013. Critical distance s_{cr} depends upon a number of parameters including the Deborah number De and fluid rheological properties. (a–c) For a De lower than a threshold $De < De_{cr}$, if at least one inter-particle distance (s_1 or s_2) is lower than s_{cr}, the trailing and middle particles form a doublet while the trailing one moves away, becoming isolated. (d) For $De < De_{cr}$, if both inter-particle distances (s1 and s2) are higher than s_{cr}, the three particles separate and become isolated. (e) For $De > De_{cr}$, the three particles separate regardless of the inter-particle distances. The flow goes from the left to the right. This figure was reprinted from Jeyasountharan et al 2021 [26].

2.4 Droplet Microfludics

Recent progress in microfluidics technology has led to a wide array of applications. As discussed previously, particle and cell manipulation is a single branch applications that has been extensively employed in fields ranging from Biomedicine [6] to Tissue Engineering [7]. In Biomedical research, microfluidics has been employed to sort, separate and characterise cells and particles based on parameters such as size [128], density [129], charge [130], and antigenic surface properties [12] in miniaturised "Lab On Chip" devices [20, 37, 131]. In Tissue Engineering, microfluidics has been used to achieve greater degree of spatiotemporal controllability over fluid flow and tissue scaffolds for high-throughput analysis. To either replace or repair tissue scaffolds [7]. A large portfolio of microfluidic applications are made possible due to the principle of large surface area to volume ratio SAV, which essentially means reagent volume and length required to complete a reaction is drastically reduced in a microfluidic device with continuous flow system [132, 133]. This allows highly parallel reactions to be performed in a high-throughput manner with great degree of fluid manipulation [134].

Based on SAV principle and the advantages that miniaturised systems offer such as high-throughput systems capable of parallel analysis. Droplet microfluidics consists of generating and manipulating micron sized uniform droplets [135] and has been recognised as an emerging field in Biomedical research [136], mainly due to the ability to generate high frequency droplets with minimal reagents. This is suitable for applications which require a large number of particles and cells to be encapsulated in droplets, e.g. for singe-cell sequencing and encapsulation [137]. Single-cell sequencing of messenger ribonucleic acid mRNA is a useful tool for mapping cellular heterogeneity in different cell types i.e. diseased and healthy tissues. This allows comprehensive data sets on cell-to-cell interactions rather than at a multi-cell level. Droplet microfluidic technology is a leading candidate in achieving high-throughput and parallel single-cell analysis [121]. For example, target cells encapsulated in droplets with barcoding DNA primers, where cells are lysed and mRNA is barcoded by a reverse transcription RT reaction, in a high-throughput manner [121, 138, 139]. In addition, Droplet microfluidics has been successfully used as multi-functionalized carriers [140] for drug encapsulation [141] and delivery [142] in Biomedicine for efficacious controlled drug release mechanisms with site-specific distribution [142]. Other common applications of droplet microfluidics include antibody screening [143], enzyme screening [144] and other cell to cell interaction analysis [145].

Over the years, techniques have been developed to control droplet generation frequency, size and shape [146, 147]. As previously mentioned, just like particles and cell manipulation methods in microfluidics. Droplet manipulation techniques can be either active or passive, the latter technique adds an extra level controllability in forming droplets with the use of external fields in addition to the pressure driven flows often imposed with syringe pump in passive techniques [148]. Similar to active particle and cell manipulation techniques that are mentioned above. Active droplet manipulation often uses electrical [149], magnetic [150], acoustic [151] and even centrifugal fields [152] to form droplets in microfluidic devices. However, these approaches require complex microfluidic external configuration setups, which may be time consuming and expensive especially for highly parallel applications. In addition, high field strengths from active methods can damage delicate cell structures inside droplets [153]. Thus, previous works have mainly focused on passive methods to form droplets. Passive techniques generate droplets by dispersing one phase (dispersed phase) into the another immiscible phase, often called the continuous phase [130]. In general, dispersed and continuous phase is independently bought into contact by a pressure-driven flow in various channel geometries [154]. Flow of dispersed phase is broken up by the immiscible continuous phase. At the droplet formation site, local flow field deforms the dispersed phase at the interface, which leads to interfacial instabilities. This causes the droplets to pinch off from the dispersed phase. This approach allows molecular reactions and processes to be confined in a volume of a single droplet, which reduces reagent volume and reaction time while allowing a compartmentalised reaction system to develop in a droplet. More specifically, as mentioned above droplet microfluidics finds applications in particle or cell encapsulation and in single-cell resolution analysis that requires a target cell to be encapsulated inside a droplet with a high efficiency [121].

2.5 Droplet generation in Microfluidic devices

In droplet microfludics, three kind of structures are commonly used for droplet generation: (1) Flow focusing; (2) Co-Flow and (3) T-junction devices (Figure 2.6). In a flow focusing device, the dispersed phase, contained is in the middle channel, and is squeezed by continuous phase flows from above and below [155, 156]. As both phases pass an 'orifice' that is located downstream, droplets break off (Figure 2.6a). Drop formation in the flow focusing geometry depends on the Capillary number Ca, viscous forces and interfacial tension [155]. One major disadvantage of flow focusing device is that large number of flow streams are required to generate the droplets, which makes the system more complex, since there are more than one continuous phase streams. In Co-flow geometries, the dispersed phase is injected through a small capillary that is located inside a larger capillary, once the vicious shear stresses of continuous phase overcome the interfacial tension. The base of the droplet, that is adhered to the small capillary tip break and form a droplet Figure 2.6b [157]. A disadvantage of Co-flow geometry is that, it's relatively difficult to fabricate devices with a small capillaries embedded inside a large outer ones. As a result, this geometry is not suitable for high-throughput biomedical applications. T-junction geometries are commonly employed to form droplets, continuous and dispersed phase intersect at the T-junction and droplets form at the point of intersection due to shear vicious forces acting on dispersed phase (Figure 2.6c) [158]. One major advantage of T-junction geometries is that only one continuous and dispersed phase flow stream is required to generate droplets as compared to flow focusing device, which makes T-junction geometries suitable for highly parallel applications such as single cell or particle encapsulation droplets. Furthermore, T-junction geometries have been shown to cause a lower variation in droplet size [159], which is beneficial for developing controlled cell or particle encapsulation systems with uniformly sized droplets.

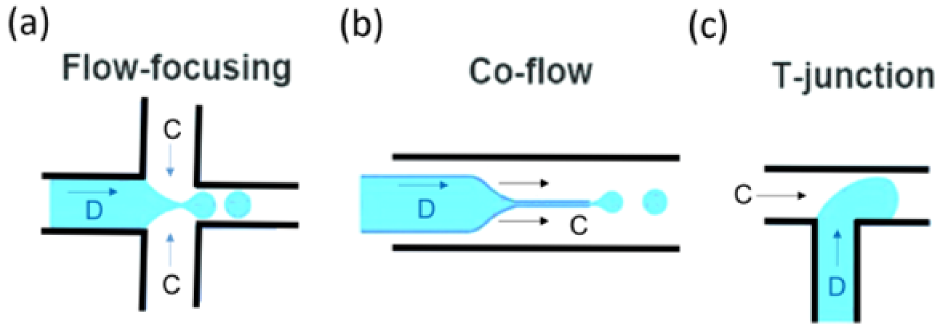

Figure 2.6: Microfluidic devices with various geometries used for droplet generation. (a) Flow-focusing structure, (b) Co-flow structure and (c) T-junction structure. Flow of continues C phase and dispersed phase D are presented for each geometry.

2.6 T-junction geometry in droplet microfluidics

A T-junction configuration, was first demonstrated by Thorsen et al, 2008 who produced monodisperse droplets using a pressure driven flow [158]. In a typical T-junction device, two immiscible liquids namely continuous and dispersed phases flow orthogonally and meet at the T-junction (Figure 2.6c). At the T-junction, viscous shear forces of the continuous phase elongate the head of the dispersed phase, so the dispersed phase adopts a spherical structure and form droplets due differences in interfacial tension between both phases [160]. Since the pioneering work by Thorsen et al in 2008, extensive studies have focused on T-junction geometries, to better understand the droplet formation mechanisms [130, 159, 160, 161, 162]. Based on previous works, it is well-established that the size, shape and frequency of the droplets depend on parameters such as the flow rate ratio of the two phases [158, 160, 163, 164], channel geometry [165], viscosity between the two phases [166, 167] and the presence of any surfactant that may affect the interfacial tension between both phases [24, 168, 169]. Mechanism by which monodisperse drops are formed also depend on *Ca* number (the ratio of viscosity to interfacial tension) equation (3.6). For instance, at high *Ca* values, large viscous drag of the continuous phase shears the dispersed phase and form droplets that are smaller than the channel diameter. At low *Ca* values, dispersed phase cause the hydrodynamic pressure to rise upstream in the continuous phase. which squeezes on the dispersed phase to form a droplet [160, 170].

Based on the parameters that influence droplet size, shape and frequency of generation. In a T-junction configuration, four main regimes develop: (1) squeezing; (2) dripping; (3) jetting; and (4) parallel flow [160, 171]. In squeezing regime, which occurs at low *Ca*. The viscous stresses do not overcome the interfacial tension, so droplet at the junction tend to obstruct the channel and restrict the continuous phase flow. This in turn causes an increase in hydrodynamic pressure upstream, which leads to the droplet pinch off. In dripping regime, viscous shear stresses of the continuous phase cut the dispersed phase, which leads to the breakup of spherical droplets. Dripping regime occurs at moderate Ca numbers [160]. Transition from squeezing to dripping regime depends on the Ca number and fluid viscosity [172]. At very high Ca numbers, a long stream of dispersed phase jets up steam of T-junction, which is continually cut by the shear forces from the continuous phase. Finally, in parallel flow the Ca number exceeds a critical value, both phases flow parallel to each other (no droplet formation) [171]. For applications concerning delicate particles or cells, it's more suitable to use the T-junction dripping or the squeezing regimes at low to moderate Ca numbers, where the flow rate ratios of both phases and the velocities are not large enough to cause cell damage (refer to equation 3.6).

2.7 Importance of droplet Microfluidics in single-cell analysis

The most relevant applications concerning droplet microfluidics involve the ability to carry out parallel analysis on large single cell populations, where single cells are encapsulated in droplets to determine cellular properties or to decode genetic information. Multi-level cell characterisation methods such as gene profiling, protein and other bio-marker expression profiling only provides global insights of multi-cellular function [173]. In addition, for a given cell population, heterogeneity can be found in the morphology [174], composition [175], genetic behaviours and even in phenotypes of cells from the same population [176, 177]. Such variations are common amongst diseased cells i.e. cancer cells. For example, Zhao et al 2018, implanted human tumour xenografts in mice and detected tumour heterogeneity in endothelial and mesenchymal cells [178]. Lambrechts et al 2018, made a lung cancer model in mice, separating stromal cells into 52 different subsets with unique gene expression signatures [179]. Jamal-Hanjani and colleagues, sampled of 327 tumour regions from 100 early stage Non-small cell lung cancer cells and revealed a high level of intratumoural heterogeneity, with 30 % of somatic mutations in samples [180]. These works only present few hectrogentoic variations that are present in tumour cells and many other heterogeneity variabilities are yet to be discovered [181]. Logically, heterogeneities among diseased cells from the same population presents a huge challenge in biology and medicine for diagnostics and treatment [182]. It is critical to understand how such cellular diversity is generated from a single-cell population for example: in cellular expression; homeostasis regulation and, even variations in responses to external stimuli between normal vs diseased tissues. This will help to develop optimal treatment approaches to target diseased tissues. To understand variations in cell types, analysing a population of cells at a single-cell level will help to gain valuable insights into unique cell to cell interactions. Therefore, single-cell analysis has become an emerging yet challenging field in modern biomedical research.

As mentioned previously, droplet microfluidics is a critical platform required for single-cell analysis i.e. mRNA-sequencing to understand cells at a single level resolution. Single-cell analysis was first demonstrated by Tang et al 2009, who studied the heterogeneity of gene expression within a cell population and detected 75 % more gene expression in mouse blastomere embryo cells. However, the throughput for analysis was relatively low [55]. The development of droplet based microfluidics led to commercialized single-cell analysis platforms, including DropSeq, inDrop, Nadia instrument and 10x Genomic [148, 183]. These technologies often employ miniaturised microfluidic devices to capture target single cells in droplets [56]. For example, Macosko et al 2015, utilised Drop Sequencing platform to profile genome-wide expression of individual cells [76]. In their work, mRNA of encapsulated cells were tagged with barcoded beads and reverse transcription-polymerase chain reaction was used for mRNA isolation, detection and quantification, where each cell was encapsulated inside a droplet with barcoded beads. They categorised 39 cell populations from nearly 45,000 mouse retinal cells [76]. It is very clear that heterogeneities among cells of the same population exist and require novel microfluidic approaches to encapsulate particles and cells in droplets for single-cell analysis to decode genetic information. Understanding the complex genetic information of heterogenic cells such as diseased cells may provide insights into optimal treatment methods for a better clinical outcome.

Microfluidic devices allow control and manipulation of small volumes of liquid. In terms of single-cell analysis. The separation and partitioning of single cells from a complex heterogeneous population provide some benefits. For example, partitioned cells can be used as templates for individual PCR reactions using primers and probes for the amplification of small-subunit ribosomal RNA (rRNA) and metabolic genes. This enables a greater degree of understanding of single-cell genomics in relation to the overall cell population, which is crucial for applications such as highly parallel diagnostic assays, biomarker detection, and disease management [184]. The coupling of microfluidic technology with PCR provides key benefits such as a reduction in reagent volume and high-throughput analysis. Warren et al 2006 utilised a commercially available microfluidic chip (Fluidigm) to partition individual complementary DNA molecules into discrete reaction chambers before PCR amplification to allow parallel analysis [185]. More recently, droplet microfluidic systems have been combined with PCR to fine-tune PCR technology to achieve a compartmentalised system, where individual cells are confined in a volume of droplets. Monodisperse droplets with tuneable volumes can be generated using various microfluidic chip designs, where the droplet size is adjusted by varying channel geometry, flow rate, and dispersed-phase viscosity

[158, 160]. A study by Beer et al 2007, employed a T-junction in a silicon device to generate 1000 monodisperse picoliter droplets per second. The device had a width of 60μm. They used an off-chip valving system and stopped the droplets on-chip, which allowed the droplets to be thermally analysed. With this system, a 10 picoliter droplet, encapsulated less than one ($\sim$0.06) copy of viral genomic DNA, whereas real-time PCR amplification curves with a cycle threshold of $\sim$18 [186]. Hindson et al, 2011 achieved $\sim$2 million PCR reactions using a high-throughput droplet-based digital PCR system, which included a droplet generation device to generate water-in-oil droplets and a 96-well PCR plate with a conventional thermal cycler for application [187].

2.8 Controlled particle encapsulation in droplets

Droplet microfluidics often provides a critical step in single-cell analysis to compartmentalise particles or cells in droplets, which is generally obtained within microfluidic devices, as they allow a precise control of the experimental parameters required to produce droplets with a uniform size and shape [188, 189]. However, one of the main limitations that effect several encapsulation and single-cell analysis applications is the uncontrolled stochastic nature of cell or particle encapsulation, where multiple cells or particles are encapsulated in the same droplet. To reduce multiple particles from being encapsulated in the same droplet, the dispersed phase containing the suspended particles can be diluted. This approach presents another problem, where empty droplets are formed. The uncontrolled stochastic nature of particle encapsulation in a droplet is governed by Poisson statistics [74, 100]. The probability $P(k,n)$ of finding a droplet containing n particles is $P(k,n) = k^n \exp(k)/(n!)$, where k is the average number of particles per droplet [24, 100]. The encapsulation of one particle per droplet is around 37 %, meaning that the remaining droplets will either be empty or contain multiple particles in the same droplet [24]. The reason for the existence of such limit is the fact that particles approaching the encapsulation area do not arrive at a constant frequency, at variance with droplets that are instead generated at a constant frequency governed by the volumetric flow rate values of both continuous and dispersed liquid phases [189]. To achieve controlled encapsulation, it is required to attain single particle encapsulation efficiencies above the Poisson limit. Very few studies have achieved controlled encapsulation. The requirement of improving the encapsulation efficiency above the Poisson limit has attracted significant interest in the recent years.

A pioneering work by Edd et al, 2008 introduced a methodology to ‘beat’ the Poisson limit by using the particle ordering phenomenon [100], where particles were equally spaced on one or more streamlines before approaching the encapsulation area. In general, when flowing particles are equally spaced, the frequency of particles approaching the encapsulation area becomes constant [190]: the authors synchronised this frequency to the one of droplet formation, thus achieving single encapsulation efficiency above the Poisson limit. Several other works [74, 191, 192] have followed this original idea and designed microfluidic devices to take advantage of the inertial particle ordering phenomenon [29, 31] to overcome the Poisson statistic limit.

2.9 Controlled encapsulation in viscoelastic microfluidic flows

Very recently, the same principle originally introduced by Edd et al, 2008 [100] was employed within the framework of particle encapsulation using non-Newtonian viscoelastic liquids [24, 169]. In these works, the authors took advantage of the recently discovered viscoelastic particle ordering phenomenon [26, 27, 126] to demonstrate a viscoelastic particle encapsulation up to 2-folds larger than the Poisson limit. Shahriver et al, 2021 employed a commercial T-junction glass microfluidic devise together with an aqueous shear thinning xanthan gum suspending liquid [24]. In another work, Shahriver and colleagues designed a microfluidic device with a flow-focusing configuration and employed aqueous solutions of hyaluronic acid, demonstrating viscoelastic encapsulation and co-encapsulation of particles up to 2-folds larger than the Poisson limit [169] . To date, the two manuscripts from Shahrivar and colleagues are the only ones featuring viscoelastic encapsulation of particles [24, 169], with several questions remaining unanswered. For instance, the suspending liquids employed so far were not appropriate to work with cells, as cells require phosphate buffer saline (PBS) in order to survive. The addition of PBS to the suspending liquids reported in the previous works, however, could result in changes of the suspending fluids rheological properties. Notably, a reduction in the magnitude of the shear thinning behaviour [59, 193], which in turn would lead to the suppression of particle ordering, in favour of particle string formation (i.e., particles attached to each other) [27, 49, 123]. Furthermore, the devices introduced so far were still affected by the problem of particle aggregates (e.g., doublets or triplets) that were breaking the continuity of the particle trains [26, 123]. Therefore, it is important to study whether the addition of PBS to viscoelastic liquids would first lead to particle train formation and then controlled encapsulation in droplets. Equally, it is also very important to design microfluidic devices to reduce the occurrence of particle aggregates, which are detrimental to train formation in viscoelastic microfluidics.

Chapter 3

Methodology

The methodology chapter details the materials and methods employed to conduct all the experimental work involved in corresponding chapters: 4, 5, and 6. Hereafter, an overview is presented prior to each methodology section to provide a basic outline of the experimental procedures in relation to the main research framework.

3.1 Dimensionless parameters

In both viscoelastic and inertial flow, particle migration and longitudinal ordering mechanisms are dependent on parameters such as forces acting on particles, interactions between particles, fluid rheology, volumetric flow rate, channel and particle size [49, 50, 51, 52, 53, 58, 117, 118]. To identify and quantify the interplay among these mechanisms and parameters, we use dimensionless parameters employed in literature [59, 116, 194].

Deborah number *De*

Reiner proposed that difference between solids and liquids is characterised by the magnitude of *De*. Reiner defined *De* as the ratio between the time of relaxation and the time of observation [195]. If the time of observation is long or the relaxation time of the material is short, then the material under observation will exhibit a fluid-like behaviour. Conversely, if the relaxation time of the material is large, or the time of observation is short, then the Deborah number is high and the material behaves as a solid. Metzner and colleagues altered the definition of *De* from the “time of observation” to the “time scale of the process” within a complex flow field [196]. Thereafter, microfluidic works further altered the definition of *De*. For example, the original definition proposed by Reiner has been altered from "time of observation" to “characteristic time scale” to reflect the short experimental time scales observed in microfluidic flows [49, 50, 64, 116, 197].

For a micro channel with circular diameter D, Deborah number *De* is used to characterise fluid viscoelasticty and governs the degree to which elasticity manifests itself in response to a transient deformation. *De* is the ratio between the time of relaxation and the time of observation. The time of relaxation is often referred to as the longest relaxation time of fluid λ, and the time of observation, which can be quantified through flow characteristic time $\frac{D^3}{Q}$ where D is the channel diameter and Q is the volumetric flow rate.

$$De = \frac{4\lambda Q}{\pi D^3} \tag{3.1}$$

For a square shaped micro channel, *De* is represented as:

$$De = \frac{\lambda Q}{H^3} \tag{3.2}$$

Newtonian fluid, with $\lambda = 0$ due to instantaneous relaxation, has a $De = 0$, whereas $De > 0$ is true for more elastic non-Newtonian fluids with $\lambda > 0$. Our study employed *De* values in the range of 2 to 15.

Reynolds Number *Re*

Reynolds number *Re* is the ratio of inertial forces to viscous forces in a fluid, where ρ is the fluid density, Q is the volumetric flow rate, H is the channel height and η is the shear viscosity.

$$Re = \frac{\rho U D}{\eta} = \frac{\rho Q}{\eta H} \tag{3.3}$$

Higher *Re* correlates to larger fluid inertia. In contrast, lower $Re << 1$ corresponds to negligible inertia. Our study had a negligible *Re* number. Therefore, inertial effects are insignificant.

Elasticity Number *El*

Elasticity number (El) is the ratio between De and Re.

$$El = \frac{De}{Re}$$

Where *De* is the Deborah number and *Re* is the Reynolds number.

Confinement ratio β

Confinement ratio β is the ratio between particle diameter and channel height.

$$\beta = \frac{d}{H} \tag{3.4}$$

Where d is the particle diameter and H is the channel height.

Local Particle Concentration ϕ_l

Local particle concentration ϕ_l accounts for the number of particles observed in a single frame and was defined as:

$$\phi_l = \frac{N_p d}{L_f} \tag{3.5}$$

where L_f = 64d is the length of the observation window, d is the particle diameter. N_p is the number of particles in the observation window for a specific frame. Local particle concentration ϕ_l varies between 0 (no particle in the frame) and 1 (the aligned particles were in contact and formed a string with length equal to the observation window).

Capillary Number Ca

The main properties of two immiscible fluids that determine the droplet size are the interfacial tension γ, dynamic viscosity of dispersed phase μ_d, continuous phase μ_c, the flow rate ratios of dispersed Q_d and continuous Q_c phase. In general, the Capillary number Ca of continuous phase is define as:

$$Ca = \frac{\mu U_c}{\gamma} \tag{3.6}$$

For square-shaped micro channel, $U_c = Q_c/WH$ is the average velocity of continuous phase fluid with W being the channel width and H being the channel height.

3.2 Particle ordering in viscoelastic xanthan gum solution

In this section, we developed a methodology to achieve equally spaced particles i.e. particle trains in a hydrophilic commercial T-junction microfluidic device (Dolomite Microfluidics) made of glass. Firstly, we identified Xanthan Gum (XG) as a suitable inexpensive viscoelastic polymer with shear thinning properties [26, 198]. XG was suspended in deionized water and rheologically characterised at various mass concentrations to confirm the shear thinning and viscoelastic properties. Then, a wide range of volumetric concentrations of polystyrene particles was suspended in the 0.1 wt% XG to observe particle train formation. Particle flow was tracked using microfluidic apparatus and videos were taken at specific points along the microfluidic device. Finally, the data was analysed using a homemade MatLab software and presented as probability histogram plots.

3.2.1 Sample Preparation

An aqueous XG solution was prepared at mass concentration of 0.1 wt% by dissolving Xanthomonas campestris (Sigma Aldrich UK) in deionized water. For the purposes of the experimental work, 0.1 wt% was used as the lead suspending liquid due to the shear thinning behaviour, low shear viscosity and experimental advantages at low mass concentration as detailed in following section [26]. The prepared solution of 0.1 wt% XG was mixed using a magnetic stirrer (Fisherbrand) for 12 hours to allow full dissolution of the polymer in deionized water.

3.2.2 Rheological Characterisation

The rheological measurements were conducted on a stress-controlled rheometer (TA AR2000ex) with a truncated (60 mm diameter, 1° angle) acrylic cone at constant temperature (T = 22 $^\circ C$). A home-made solvent trap was used to prevent excess evaporation of XG solution during the rheological measurements. In the shear rate region 10^{-1} to 10^3, we observed shear thinning behaviour. At shear rate values below 10^2, there is a tendency to approach a plateau region, which is not observed in our experiment (Figure 3.1a). Since, we did not observe a clear terminal region for G' and G'', we used cross model to obtain a reference relaxation time of 1.55 ms. Here, the fitted parameters are: λ = 1.55 s, η_0 = 0.22 Pas, η_∞= 0.00165 Pas and n= 0.605 Pas. The shear thinning behaviour of XG solution was also determined by fitting viscosity curve with the cross-model.

$$\eta = \eta_\infty + \frac{\eta_0 - \eta_\infty}{1 + (\lambda\dot{\gamma})^n} \tag{3.7}$$

where η_∞ is the infinite shear viscosity, η_0 is the zero shear viscosity, λ is the longest relaxation time, $\dot{\gamma}$ is the shear rate and n is the factor that modulates the transition between the constant region above. Here, the fitted parameters are: λ = 1.55 s, η_0 = 0.22 Pa.s, η_∞= 0.00165 Pa.s and n= 0.605 Pa.s.

The elasticity of XG solution was quantified with a small angle oscillatory shear rheological test, where G' and G'' was evaluated as a function of angular frequency ω (Figure 3.1b). The minimum value of modulus G$_{min}$ and viscosity λ_{min} that are detectable by the rheometer due to torque limits is represented by [27, 199]:

$$G_{min} = \frac{2T_{min}}{\pi R^3 \gamma} \tag{3.8}$$

where, T$_{min}$ is the minimum detectable torque, R = 60 mm is the diameter of the cone, γ is the strain amplitude.

To determine the rheological properties of polymers in oscillatory measurements. Cox and Merz came up with an empirical relationship, which states that the shear rate ($\dot{\gamma}$) dependence of shear viscosity (η) is equivalent to the frequency (ω) dependence of the complex viscosity (η^*) [200].

$$\eta(\dot{\gamma}) = \eta^*(\omega) \tag{3.9}$$

3.2.3 Particle suspension preparation

Polystyrene particles (Polysciences Inc.) with a diameter d of 20 ±2 μm was added to 0.1 wt % XG polymer solution at three different volumetric concentrations ϕ = [0.2%, 0.25%, 0.3%]. Hereafter, we refer to particles with a d equal to 20 ± 2 μm as 20 μm particles. The suspension was mixed in a vortex mixer (Fisherbrand ZX3) to fully disperse the polysteryne particles in the XG polymer solution. Aggregates were removed by placing the solution in ultrasonication bath for 2-minutes.

3.2.4 Microfludic Apparatus and Particle Tracking

An inverted microscope (Zeiss Axiovert 135) was utilised to analyse particle flow in a hydrophilic glass T-junction chip (Dolomite, microfluidics) with a circular 100 μm diameter cross-section. The T-junction chip was connected to a 4-way Linear Connec-

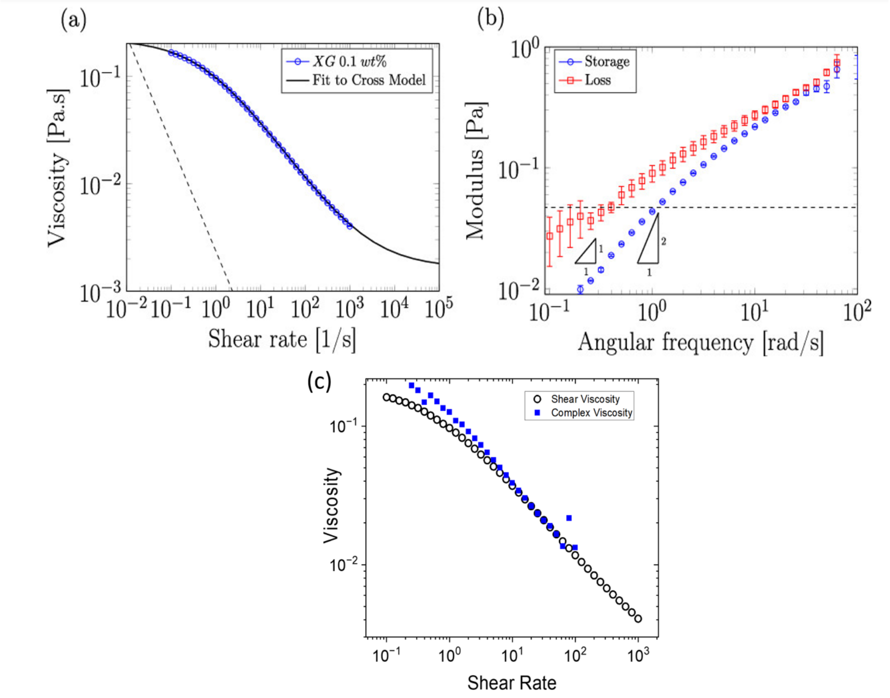

Figure 3.1: Rheological properties of 0.1 wt% Xanthan gum XG in dionized water. (a) Shear viscosity η as a function of shear rate $\dot{\gamma}$ in shear rate range $\dot{\gamma} \sim 10^{-1}$ to 10^{3}. Xanthan Gum displayed shear thinning behaviour above the critical shear rate $\dot{\gamma} \sim 10$/s. (b) Storage G' and loss G'' modulus as function of angular frequency (ω) for deformation $\gamma = 5$ %. The reference value for the relaxation time was evaluated to be 1.55 ms. Dashed-dotted lines in figures a and b shows the minimum value η_{min} and G_{min} detectable by the rheometer due to torque limit [199]. (c) Comparison between shear viscosity η and complex viscosity η^* for 0.1 wt% XG. According to Cox-Merz rule in equation 3.9, η equals η^* above shear rate $\dot{\gamma} \sim 10^1$/s. Dashed-line shown in Figure 3.1a is ηmin at T_{min} = 1 μ N·m and dashed-dotted line shown in Figure 3.1b is for G_{min} at T_{min} = 0.1 μN·m. This figure was adapted from Jeyasountharan et al 2021 [26].

tor (Dolomite, microfluidics), which was connected to a 8 mm Fluorinated ethylene propylene (FEP) tube (Dolomite, microfluidics) with an external diameter of 1.6 mm and an internal diameter of 0.25 mm. The tubing was linked to a flow rate sensor (Dolomite, microfluidics) and a mitos pressure pump (Dolomite, microfluidics) was utilised to impose the required pressure drop ΔP and the corresponding flow rate Q was translated. A schematic representation of the microchip is shown in Figure 3.2a. A video of particles flowing in the microchip was captured with a fast camera (Photron, fastcam Mini UX50) at a frame rate 2000-4000 frames per second.

The suspension was pumped at various pressure drops ΔP with a pressure pump (Mitos p-pump) and the evolution of the the flow rate Q was observed. Firstly, a Q = 20 μL/min was imposed until the flow through the channel was stabilised on the flow sensor. Then, ΔP is lowered, which translated into flow rate $Q = 5$ μL/min and images were recorded. Thereafter, ΔP was increased, which translated into $Q = 7.5$, 10, 15, 20, and 25 μL/min. Images were recorded, after the corresponding flow rate stabilisation was observed with the (flow rate software). Then, videos were captured. For each ΔP and corresponding flow rate, a video of 18600 frames was captured with duration of 4.65 s.

3.2.5 Particle Tracking Analysis

Acquired videos was analyzed with a MatLab software to determine the center to center distance between adjacent particles (Figure 3.2b). Normalized distance S^* between adjacent particles was obtained by center-to-center distance between adjacent particles divided by the particle diameter, $S^* = s/d$, where s is the center-to-center distance between adjacent particles and d is the particle diameter. The binning size was set to 1 and the boundary ends were set to 64, which is the total length of the observation window. Inter-particle distance histograms were then evaluated the probability of S^* at various Deborah numbers.

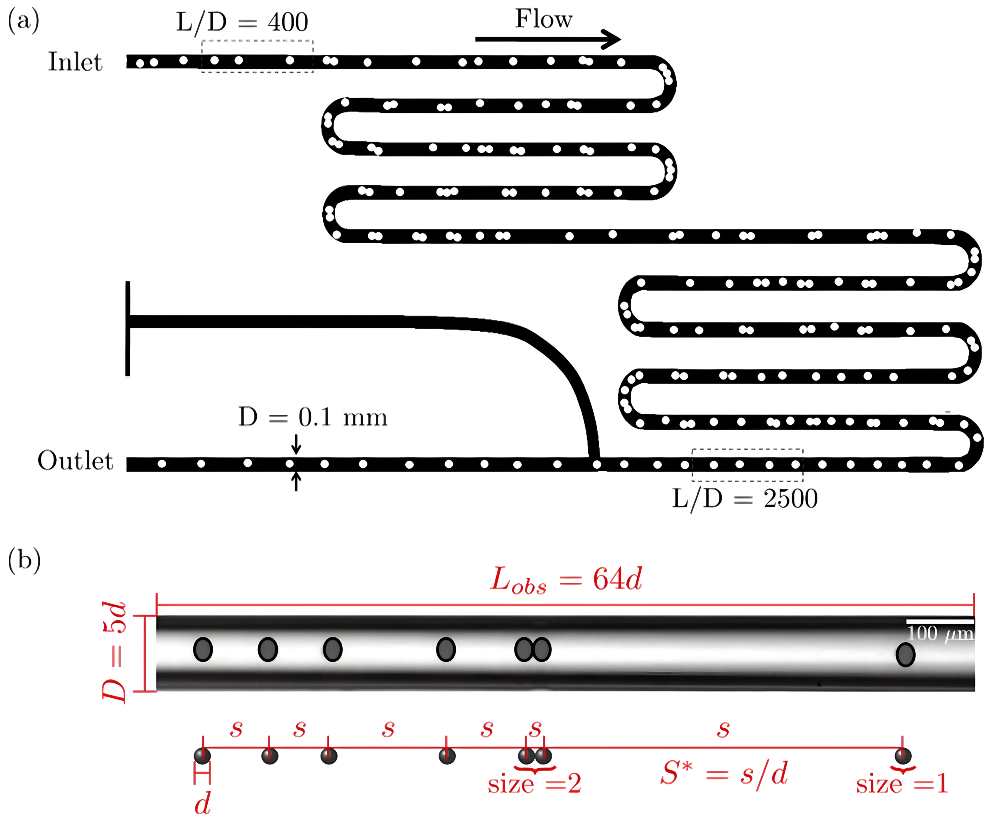

Figure 3.2: Particle flow in the serpentine micro channel. (a) Schematic representation of the micro channel with relevant dimensions. The internal diameter D of the micro channel is 0.1 mm. Polystyrene particles with 20 μm internal diameter was injected into the channel and particle flow was observed at (dimensionless) distance from the channel inlet $L/D = 400$, which corresponds to 4 cm from the channel inlet. The particles migrated through the serpentine channel structure towards $L/D = 2500$. As shown in Figure 3.2a, particles are aligned but not ordered at $L/D = 400$. Then progressive ordering of particles was observed towards $L/D = 2500$. (b) The normalised distance between particles S^* was determined by comparing the ratio between center to center distance of adjacent particles s to particle diameter d, which is represented as S^* = s/d. A binary image thresholding was used to determine the area of the particles, which was used to determine the particle size i.e. isolated particles are represented with a size of 1. Scale bar is 100 μm. Dimensions are not to scale. This figure was reprinted from Jeyasountharan et al 2021 [26].

3.3 Reducing multi-particle string formation and particle self-assembly in microfluidic flow

In this section, we used two fabricated microfluidic devices for the experimental work. The first device consisted of an inlet followed by sixteen trapezoidal elements and an outlet (Figure 3.4a). This device was used to break and reduce the occurrence of particle aggregates. Our second device, had a circular glass capillary with a diameter d of 0.1 mm and length of 30 cm (Figure 3.4b). The evolution of particle ordering dynamics was observed along the length of the glass capillary. First, we rheologically characterised the suspending fluid Xanthan Gum XG at 0.2 wt %. Flow was imposed in the microfluidic device and the particle aggregate occurrence was observed at inlet, trapezoid element sixteen and at the outlet.

Rigid polystyrene particles with two diameters was employed in experiments: (1) polysteryne particle with a diameter $d = 20 \pm 2\ \mu$m at volumetric concentrations ϕ = 0.2 and 0.3 %; (2) polystyrene particles with a diameter $d = 45 \pm 5\ \mu$m at a volumetric concentration ϕ = 0.7 %. Reduction in particle aggregate occurrence was achieved using the first device (Figure 3.4a). The second device was used to observe the ordering dynamics along the length of the glass capillary (Figure 3.4b). Particle flow was imposed with a pressure pump, particle tracking was conducted with the relevant microfluidic apparatus and videos were acquired accordingly. Data from the acquired videos was analysed using a homemade MatLab software, which were presented as frequency distribution to quantify reduction in particle aggregate occurrence. Probability histogram plots was used to quantify the ordering dynamics in the glass capillary.

3.3.1 Sample Preparation

XG solution was prepared at 0.2 wt % by dissolving Xanthomonas campestris (Sigma Aldrich, UK), Xanthan gum XG in deionized water. We studied ordering dynamics in XG at higher mass concentration, 0.2 wt %. As previous works have shown that self-assembly of particles occurs in viscoelastic polymers, with strong shear thinning behaviour [49, 125]. Prepared solution of 0.2 wt % XG was mixed using a magnetic stirrer for 12-16 hours to fully dissolve the polymer in the deionized water.

3.3.2 Rheological Characterisation

A stress-controlled rheometer (TA AR2000ex) with a truncated acrylic cone, diameter of 60 mm, 1° angle) was used for the rheological characterisation of 0.2 wt % at a constant temperature T = 20 $^\circ C$. The characterisation showed that XG solution displayed zero shear viscosity plateau at shear rate values $\dot{\gamma} < 10^{-1}\ s^{-1}$ and shear thinning behaviour at $\dot{\gamma} > 10^{-1}\ s^{-1}$ (Figure 3.3a). Small Amplitude Oscillatory Shear (SAOS) tests was used to determine the storage G' and loss G'' moduli, which was in turn used to characterise the fluid viscoelasticity i.e. longest relaxation time λ. Due to the limitations of the stress controlled rheometer, we did not observe the terminal region at low angular frequencies (Figure 3.3b). Therefore we could not characterise λ based on the intersection of G' and G''. Instead, we employed the intersection point between the power law fit and straight line representing the zero shear viscosity plateau to determine λ [26, 201]. The same method was used by Wyatt and Liberatore to determine λ on aqueous XG solutions [201]. The critical shear rate $\dot{\gamma}_c$, at the intersection point r was used to determine λ, based on the relationship: λ = 1 / $\dot{\gamma}_c$. The resulting value of λ for 0.2 wt% XG was 1.25 s (see Figure 3.3a).

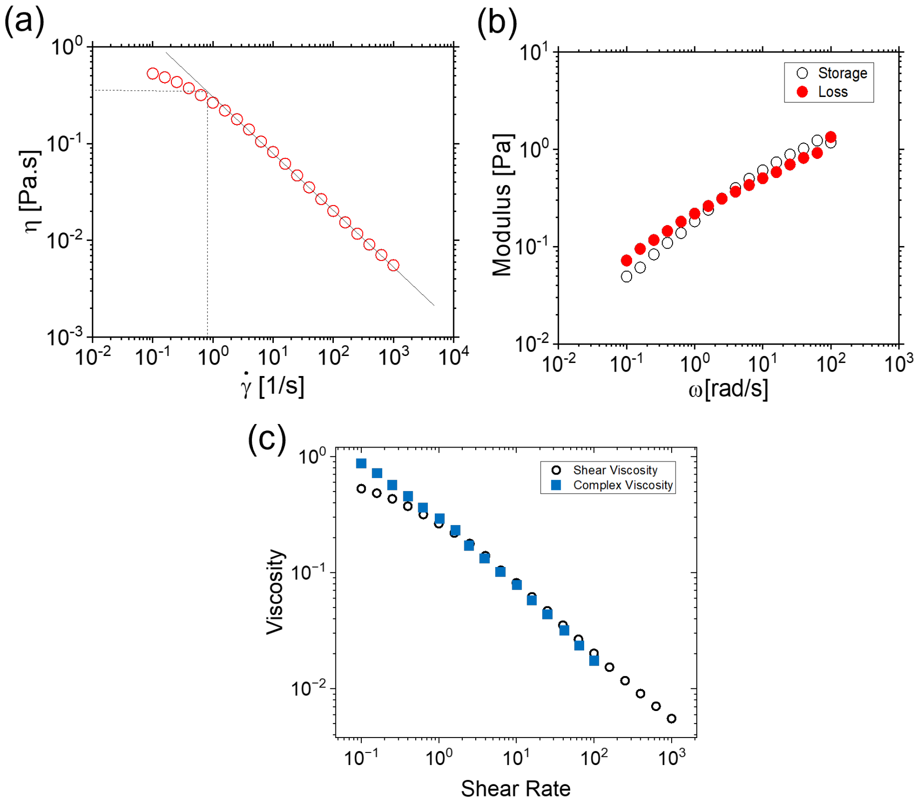

Figure 3.3: Rheological properties of aqueous Xanthan Gum XG at 0.2 wt%. (a) Viscosity curve, where shear viscosity η was a function of shear rate $\dot{\gamma}$ in the range $10^{-1} < \dot{\gamma} < 10^{-3}\ s^{-1}$. The critical shear rate $\dot{\gamma}_c$, representing the onset of shear-thinning regime was determined by intersection between the power-law fit applied in the shear-thinning regime and the straight line representing the zero-shear viscosity plateau. The longest relaxation time λ was determined by the taking the inverse of $\dot{\gamma}_c$ based on the relationship, $\lambda = 1\ /\ \dot{\gamma}_c$. (b) The viscoelastic properties of XG was characterised by Small amplitude oscillatory shear (SAOS) tests, where 5 % deformation was imposed to determine the storage G' and loss G'' moduli as functions of angular frequency ω. G' is represented by solid red circles and G'' with black open circles [202]. (c) Comparison between shear viscosity η and complex viscosity η^* for 0.2 wt% XG. According to Cox-Merz rule in equation 3.9, η equals η^* above shear rate $\dot{\gamma} \sim 10^0$/s This figure was adapted from Jeyasountharan et al 2022 [202].

3.3.3 Particle Characterisation

Rigid polystyrene particles (Polysciences) with diameters of $d = 20 \pm 2\ \mu$m and 45 $\pm$ 5 μm were added to the suspending fluid, 0.2 wt% XG at various concentrations. Hereafter, we refer to particles with a d equal to 20 $\pm$ 2 μm and 45 $\pm$ 5 μm as 20 μm and 45 μm polystyrene particles. Particles with a $d = 20\ \mu$m was added to suspending fluid at volumetric concentrations $\phi = 0.2$ and 0.3 %. The larger particles with a d = 45 μm, was added to the suspending fluid at a volumetric concentration $\phi = 0.7$ %. A vortex stirrer was used to thoroughly mix the particles in the suspending fluid for uniform distribution.

3.3.4 Microfluidic Device Design and Fabrication

As mentioned in Section 3.3, experiments were performed on two different microfluidic devices. The first device consisted of a series of sixteen trapezoidal elements to break particle aggregates formed at the inlet, as displayed in (Figure 3.4a). The second device was a combination of the first device followed by a straight 30 cm long glass capillary with a circular section, which was employed to experimentally evaluate the evolution of the particle self-assembly along the channel axis, as displayed in (Figure 3.4b).

First, computer aided design (CAD) software, Fusion 360 (Autodesk) was used to design the microfludic device with relevant dimensions. A micromilling machine (Minitech CNC Mini-Mill) was used to fabricate the microfluidic device mold from a rigid poly(methyl 194 methacrylate) (PMMA) substrate. The substrate has a length and width of 75 x 25 mm with a thickness of 1.2 mm. The milling process consisted of three main stages. First, a milling tip with a diameter of 2 mm was used to mill the PMAA substrate down to 300 μm for a uniform substrate surface. In the second stage, a tip with a diameter of 1.1 mm was used to mill the microfluidic channel CAD design onto the PMMA substrate. Finally, smaller tip with a diameter of 300 μm was used to mill around the sharp edges of all the sixteen trapezoidal elements for an acute angle. As mentioned above, we fabricated two microflduic channels with different depths. For the channel employed to break particle aggregates, the depth was kept at 100 μm and the depth was 175 μm for the microfluidic device used to observe self-assembly. Following the fabrication process, PMAA substrates were placed in an ultrasonic bath for 15-30 minutes to clean the substrates fully. Then, PMAA substrates were dried using pressurized air. Next stage involved the preparation and fabrication of polydymethyl siloxane silicone (PDMS) elastomer channel from the PMMA substrate. PDMS elastomer and curing agent (SLYGARD) was prepared at a ratio of 1:10 and mixed in a falcon tube with a vortex mixer. Resulting solution was poured onto the PMMA mold. A desiccator was employed to remove excess air bubbles in the viscous solution. The viscous PDMS and elastomer solution was poured onto the PMMA substrate and was placed in an oven at 72 $^{\circ}C$ for 1 hour to allow the PDMS to cross-link and form a hard mold. After 1 hour, a sharp blade was used to carefully cut the hardened PDMS device from the PMMA substrate. The PDMS device was placed in an ultrasonic bath for 10 minutes to remove impurities. Pressurized air was used to dry the device. The inlet and outlet holes were created by a plunger with a diameter of 1.2 mm to allow flow. A glass base with a double-sided tape (Adhesives Research, Inc) was bonded onto the PDMS device to produce the first device, as displayed in (Figure 3.4a). For the second device, which had a depth of 175 μm, a round glass capillary (Vitrocom, CM Scientific) with an internal diameter of 100 μm and an external diameter of 175 μm was attached to PDMS device. Then, the glass base with the double-sided tape was placed on top produce the second device, as displayed in (Figure 3.4b). A viscous glue (Gorilla Inc.) was put onto the interface between the PDMS mold and the glass capillary to prevent leaks from the microfluiduc device. The glue was left to dry for 24 hours. Self-assembly of particles was observed along the length of the glass capillary.

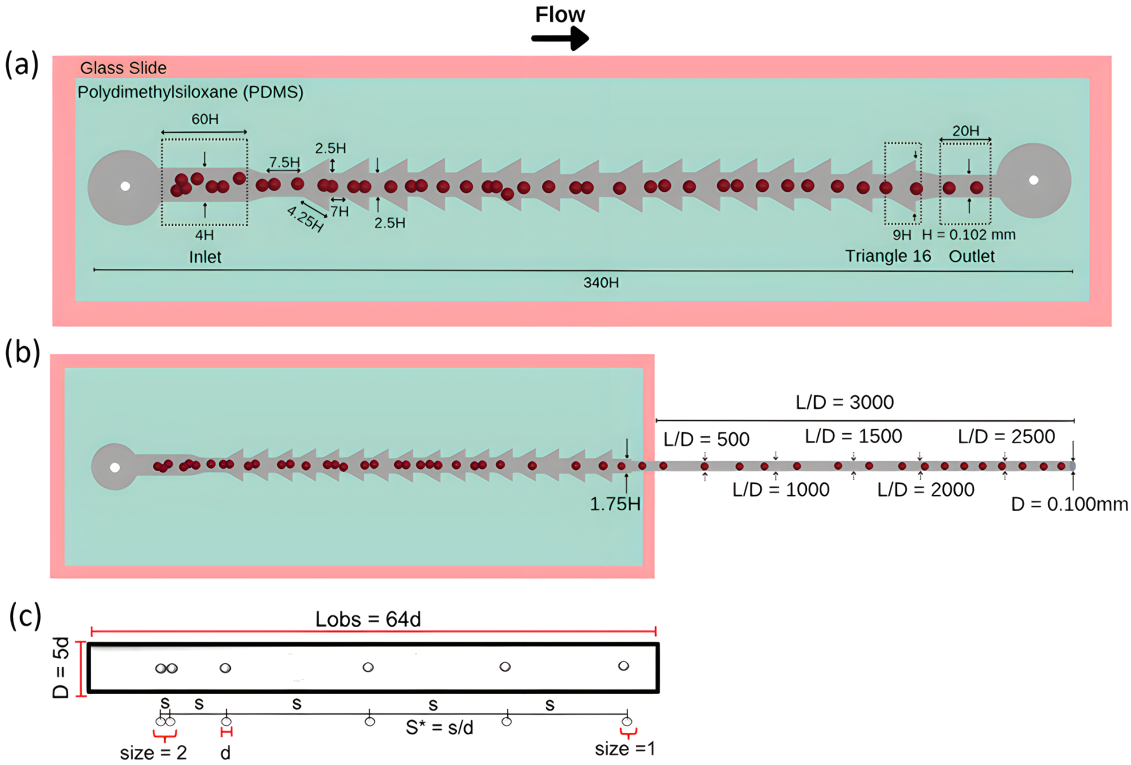

Figure 3.4: Schematic representation of the microfluidic devices used for the experiments either to break particle aggregates or to observe the evolution of particle self-assembly. (a) Microfluidic device employed to break particle aggregates, which consists of a series of trapezoidal elements with section increasing along the flow direction. The channel depth is 100 μm. All the dimensions are given in terms of the width of the last part of the channel, H = 102 μm. (b) Microfluidic device used to observe the evolution of particle self-assembly. The device was obtained by combining the channel displayed in panel (a) with a 30 cm long glass capillary, which had a circular section with diameter $D = 100$ μm employed to study particle ordering. (c) represents observation window considered in the experiments with the relevant dimensions. The normalized distance between the particles S^* is defined as the center to center distance s of adjacent particles divided by the particle diameter d. Dimensions in (a) and (b) are not to scale [202]. This figure was reprinted from Jeyasountharan et al 2022 [202].

3.3.5 Microfluidic apparatus Set up

At the device inlet, both devices shown in (Figure 3.4) were connected to a 4 mm fluorinated ethylene propylene tube (Dolomite, Microfluidics) with an external diameter of 1.6 mm and an internal diameter of 0.25 mm. Flow of liquid into the devices was modulated by a pressure pump (Dolomite Microfluidics) connected to an external compressor (Balbi) for air supply. To conduct the experiments, a pressure drop ΔP = 1000 mbar was imposed to initially flow the suspension into the channel. Then, for the particles with a diameter $d = 20\ \mu$m pressure drop was lowered to ΔP = 600 mbar, 500 mbar, 400 mbar, and 300 mbar to flow the particles with suspension and videos were acquired. For the particles with a diameter d equal 45 μm, an initial pressure drop ΔP = 2000 mbar was imposed to flow the suspension into the channel. Then the pressure drop was lowered to ΔP = 1000 mbar, 900 mbar, 800 mbar, and 700 mbar to record videos. For both microfluidic devices, an inverted microscope (Zeiss Axiovert 135) connected to a fast camera (Photron Mini UX50) was used to record all videos to observe particle flow in the suspension. The ΔP values and the corresponding volumetric flow rate Q values for both devices are shown in (Table 3.1).

ΔP(mbar)	Q(μL/min) in device 1	Q(μL/min) in device 2
300	8.4	0.50
400	14.34	0.70
500	24.05	1.50
600	35.00	2.30
700	46.71	2.90
800	58.00	3.33
900	72.00	4.35
1000	85.00	5.50

Table 3.1: Flow rate values measured via a flow sensor from the imposed pressure drop in both microfluidic devices employed for the experiments. The labels “device 1” and “device 2” refer to the channels shown in (Figure 3.4a and b), respectively.

3.3.6 Particle Tracking And Analysis

Particle tracking was conduced with a Matlab program. To quantify the particle string or aggregate occurrence. Frequency distribution was computed for particle string size at both particle diameters, where d equals particle diameter. The bin size was set to equal 1, which corresponds to one particle diameter. To quantify particle ordering, particles center to center distance s was divided by the particle diameter d to obtain the normalized distance between particles $S^* = s/d$, as shown in our previous work [26].

3.4 Viscoelastic droplet generation and particle encapsulation in a T-junction device

In this section, we focus on droplet formation and particle encapsulation in a T-junction microfluidic device. We fabricated a T-junction device with sixteen trapezoidal elements to reduce particle aggregate formation at the channel inlet [202]. As demonstrated previously, we employed a long serpentine structure prior to the T-junction encapsulation area to give sufficient length for particle ordering dynamics to occur [27, 26]. The dispersed phase, that is either Newtonian phosphate buffer saline PBS (Sigma Aldrich, Japan) or non-Newtonian 0.1 wt % Hyaluronic acid HA (Sigma Aldrich) was injected through inlet 1 for droplet generation experiments. For particle encapsulation experiments particles suspended in HA was injected through inlet 1. For all experiments, the continuous phase, that is the mineral oil (Sigma Aldrich, UK) was always injected through inlet 2. Droplet formation and particle encapsulation was observed at the T-junction. Particle flow was tracked using microfluidic apparatus and videos were taken at T-junction (droplet formation and encapsulation site). Data was analysed using a homemade MatLab software and presented as plots to characterise droplet size, frequency. Particle encapsulation was counted manually and was presented as column bar charts.

3.4.1 Microfluidic device design and fabrication

Experiments were performed in a square shaped microfluidic device designed to facilitate the encapsulation of particles with efficiency above the stochastic Poisson value (Figure 3.5). Specifically, particles suspended in the polymer solution entered the channel via Inlet 1 where they went through sixteen trapezoidal elements where potential aggregates could be broken down to individual particles, as recently shown by Jeyasountharan et al 2022, [202]. Afterwords, particles travelled along the serpentine channel to facilitate the formation of equally-spaced particle trains, as reported previously [26, 27]. The continuous phase entered the microfluidic device via Inlet 2 (Figure 3.5), and met the dispersed phase at the T-junction, leading to the formation of a droplet containing encapsulated particles (Figure 3.5).

A micromilling machine (Minitech CNC Mini-Mill) was used to fabricate the microfluidic device on a rigid polymethylmethacrylate (PMMA) substrate with a thickness of 1.2 mm, using the same approach employed in previous works [169]. Firstly, a 2-mm-wide tip was used to mill the substrate down to 300 μm to obtain a uniform surface. A 100 μm metal tip was used to mill the channel onto the PMAA substrate. Then, a 0.5 mm wide tip was used to mill the inlet and outlet holes, which had a diameter of 1.6 mm. The channel depth was kept constant to 100 μm and the width of the square shaped microfluidic device was equal to 100 μm. Following device fabrication, the PMMA substrate was placed in an ultrasonic bath for 30 minutes to remove excess material. Pressurized air was used to fully dry the PMMA substrate. A double-sided tape (Adhesives Research, Inc.) was employed to bond the PMAA substrate onto a glass slide. Home-made adapters were attached to the two inlets of the microfluidic device using a double-sided tape (Adhesives Research, Inc.).

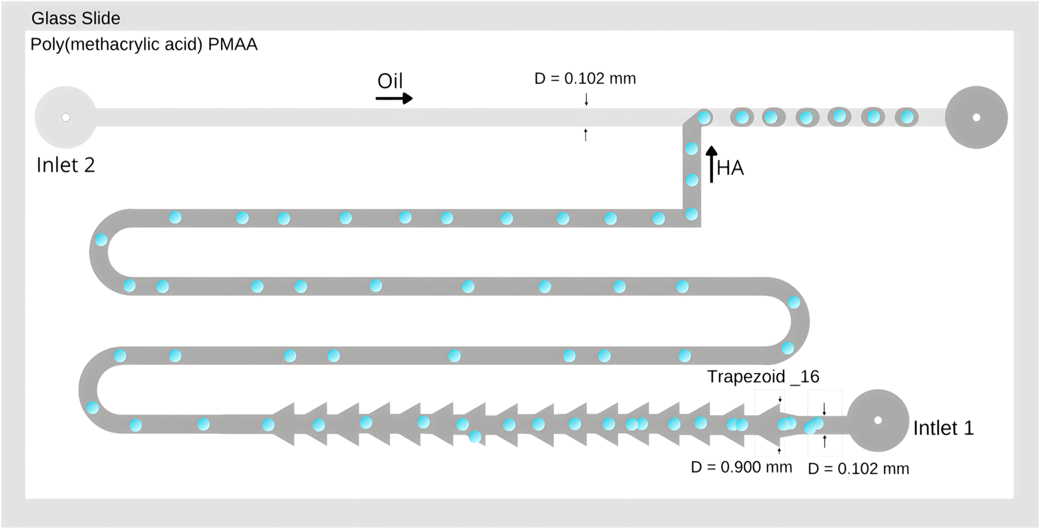

Figure 3.5: Schematic representation of the T-junction device employed in this work. The dispersed viscoelastic phase entered the device via Inlet 1. The trapezoidal structures were added in order to break down potential particle aggregates, in agreement with previous works [202]. After the trapezoidal structure, particles first aligned on the channel centerline and then self-ordered before approaching the encapsulation area. The continuous phase entered the device via Inlet 2, and the droplets containing flowing particles were formed at the T-junction.

3.4.2 Sample Preparation and Characterization

A solution of hyaluronic acid (HA, Sigma Aldrich UK) having molecular weight in the range 1.5-1.8 MDa at a mass concentration of 0.1 wt% in phosphate buffer saline (PBS, Sigma Aldrich) was used as the dispersed phase in all the experiments on viscoelastic flows. The HA concentration was chosen such that the fluid still presented shear thinning properties, but the zero-shear viscosity was not too large to affect particle mixing. The polymer powder was added directly to the PBS, and the resulting solution was stirred with a magnetic stirrer (Fisherbrand) for 12 hours to allow full dissolution of the polymer. A stress-controlled rheometer (TA AR2000ex) with a truncated acrylic cone (60 mm diameter, 1° angle) was used for the rheological measurements at a constant temperature of $T = 22°$C. The fluid presented a near constant-viscosity region for shear rate values $\dot{\gamma} \leq 30$ s^{-1}, while exhibiting shear thinning properties at larger shear-rate values (Figure 3.6). The presence of shear thinning is very important to obtain particle trains, as liquids displaying a near constant-viscosity are more likely to lead to string of attached particles rather than trains of equally-spaced objects [49, 27]. To quantify the fluid elasticity, we attempted to measure the longest relaxation time λ of the solution via conventional small angle oscillatory shear (SAOS) measurements; however, the rheometer was not sufficiently sensitive to detect such small values of λ. For this reason, we determined λ by using the μ-rheometer microfluidic rheometer recently introduced, [203, 204] obtaining a value of $\lambda = 7.27 \pm 1.73$ ms.

Mineral oil (Sigma Aldrich) was used as the continuous phase in all the experiments. Span 80 (Sigma Aldrich, UK), a non-ionic surfactant, was added at a concentration of 1 wt % to the oil to stabilize the interface between HA and oil, in agreement with previous works [24, 169]. The viscosity of the mineral oil taken from the same batch employed here was previously measured to be 29 mPa·s [24, 169]. The interfacial tension values between 0.1 wt % HA in PBS and mineral oil was here measured using a force tensiometer (Sigma 702, Biolin Scientific) equipped with a du Nouy ring. In this methodology, the du Nouy ring was first submerged in the HA solution (heavier phase), while mineral oil (lighter phase) was poured on top. The ring was brought into contact with the interface using the microbalance embedded in the instrument and the interfacial tension was obtained by measuring the force required to separate the ring from the interface. The measured value of interfacial tension was $\gamma = 3.35 \pm 0.13$ mN/m, in line with the values previously obtained for aqueous HA solutions in contact with the mineral oil [169], thus suggesting that the presence of the PBS had no effect on the interfacial tension value.

For the encapsulation experiments, polystyrene particles (Polysciences Inc.) with diameter of 20 ± 2 μm were added to the 0.1 wt% HA polymer solution in PBS at a volumetric concentration $\phi = 0.2$ vol%. The suspension was mixed in a vortex mixer

(Fisherbrand ZX3) to fully disperse the polystyrene particles in the HA polymer solution.

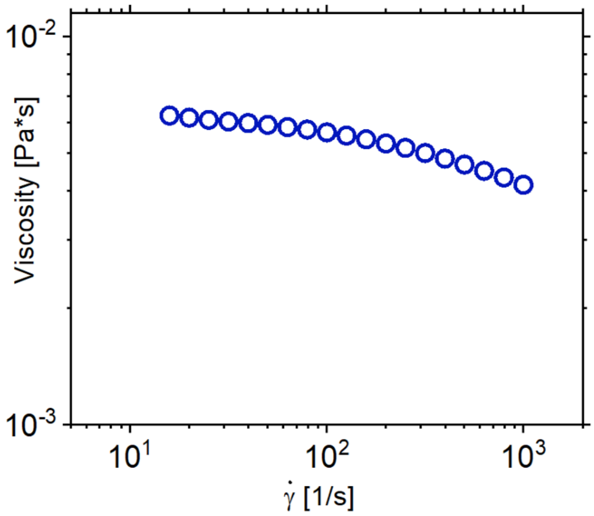

Figure 3.6: Linear rheological characterisation of 0.1 wt % Hyaluronic acid HA in Phosphate-buffered saline (PBS). Shear viscosity η_0 of 0.1wt % as function of the shear rate $\dot{\gamma}$. HA solution displays shear thinning behaviour in the $\dot{\gamma}$ range 10^2 to 10^3.

3.4.3 Suspension Preparation

Polystyrene particles (Polysciences Inc.) with 20 ±2 μm diameter was added to 0.1 wt % HA polymer solution at two different volumetric concentrations ϕ = [0.1% and 0.2%]. The suspension was mixed in a vortex mixer (Fisherbrand ZX3) to fully disperse the polystyrene particles in the HA polymer solution.

3.4.4 Experimental apparatus and particle tracking

The microfluidic device was connected to glass syringes (Hamilton) having a 1/4-28 male thread via a 10-cm long fluorinated ethylene propylene tube (Dolomite, Microfluidics) with an external diameter of 1.6 mm and an internal diameter of 0.25 mm. The tubing was connected to a syringe pump (KD Scientific). The flow rate values of continuous phase was kept constant at either Q =10,8,6,4,2 or 1 μL/min. The flow rate of dispersed phase for droplet generation and encapsulation experiments was varied in the range Q =10,8,6,4,2 or 1 μL/min for each constant value of oil flow rate.

An inverted microscope (Zeiss Axio A1) connected to a fast camera (Photron Mini UX50), which was used to acquire all the videos of droplet formation and particle encapsulation. Videos were captured at a frame rate of 250 fps. The acquired videos were analysed using a home-made code written in Matlab to determine size and frequency of droplet generation. For the particle encapsulation experiments, the number of particle per each droplet was counted manually.

Chapter 4

Viscoelastic Particle Train Formation in Microfluidic Flows Using a Xanthan Gum Aqueous Solution

4.1 Motivation

To date, there have been only a limited number of experimental studies that have utilized viscoelastic fluids to facilitate the self-assembly of particles in microfluidic flows [27, 126]. In both of these studies, hyaluronic acid was employed as the primary suspending fluid, and it was determined that the viscoelastic properties of the fluid, specifically its shear thinning behavior, were necessary to achieve the self-assembly of particles in microfluidic flows [27, 126]. There has been a lack of experimental investigation into the impact of other types of shear thinning fluids on particle self-assembly in microfluidic flows. In this chapter, we demonstrated that by, employing an inexpensive viscoelastic suspending fluid, namely 0.1 wt % xanthan gum XG. We can achieve self-assembly of particles in microfluidic flow. We also introduced a concept of local particle concentration to quantify data without the effect of the particle concentration fluctuation, which is a common issue in microfluidics [31].

4.2 Preliminary particle focusing is needed to achieve train formation in microfluidic flow

Longitudinal particle ordering in viscoelastic flow, requires adjacent flowing particles to interact hydrodynamically with each other [27, 49, 85, 126]. This condition is fulfilled when sufficiently large particle concentration leads to hydrodynamic interactions between consecutive particles. In addition, particles should also be aligned along a single streamline of the flow field for longitudinal particle ordering to occur. To date, limited experimental studies have focused on longitudinal particle ordering. Recently, an experimental work by Del Giudice et al 2018, demonstrated the self-assembly of particles in a suspending liquid with shear thinning features, namely hyaluronic acid [27]. They suggested that shear thinning behaviour is essential for self-assembly of particles on channel centerline. In accordance with Del Giudice et al 2018, we experimentally demonstrated that in Newtonian liquids under inertialess conditions, particles do not focus on a single streamline i.e. channel centerline nor self-assemble (Figure 4.1). Our findings are in line with numerical simulation by D'Avino and colleagues, who suggest that adjacent particles will experience a substantial attractive force that results in particle string formation rather than particle trains in Newtoinian liquids, whereas in shear thinning liquids particles repel and form trains (Figure 2.4 and Figure 2.5) [49, 123]. To achieve particle focusing on the centerline of the microfluidic channel in shear thinning liquids, Del Giudice et al, 2017 demonstrated that the confinement ratio β should be $\beta \geq 0.15$ (refer to equation (3.4)) [59]. In their work, lower β values led to particles being driven toward the lateral walls. In our work, we employed particles with a diameter $d = 20$ μm suspended in shear thinning liquid 0.1 wt % xanthan gum XG. The microfluidic channel had a diameter of $D = 100$ μm. The resulting confinement ratio value was $\beta = 0.2$. In agreement with previous work by Del Giudice et al 2017, we successfully demonstrated that particles focus on the channel centerline at $\beta \geq 0.2$ [59].

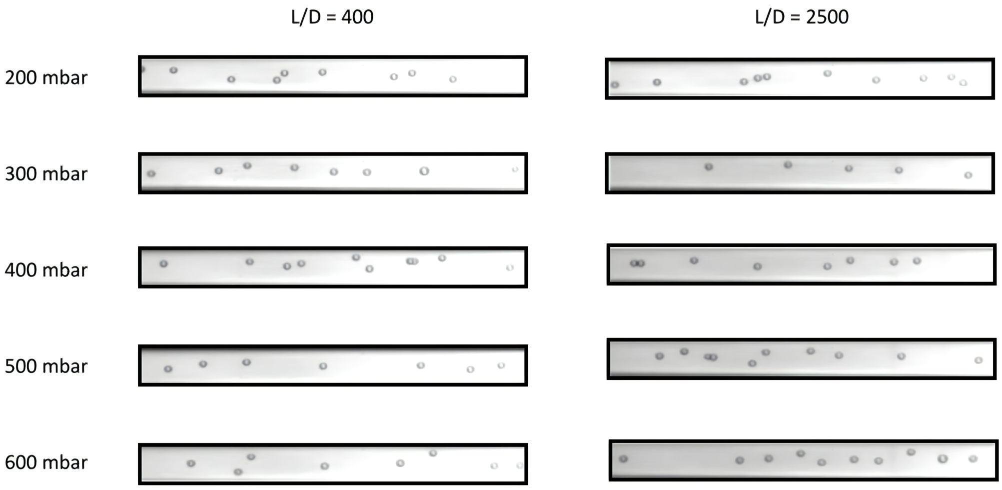

Figure 4.1: Particles suspended in a Newtonian liquid do not focus nor self-order. Experimental snapshots of flowing particles suspended in a Newtonian 25 wt % Glycerol-water solution, at bulk particle concentration $\phi = 0.2$ wt % for different imposed pressure drop values. We did not observe ordering nor any focusing at both $L/D = 400$ and $L/D = 2500$ in the whole range of imposed pressure drop values. This figure was reprinted from Jeyasountharan et al 2021 [26].

Polystyrene particles at two bulk volumetric concentrations of $\phi = 0.2$ wt % and $\phi = 0.3$ wt % were suspended in 0.1 wt % XG. We observed particle flow at length L of 4 cm from the inlet of the microfluidic device, which corresponds to a dimensionless distance of $L/D = 400$ (L is the length and D is the channel diameter). At, $L/D = 400$ particles were focused on the channel centerline (see experimental snap shots in Figure 4.2a and b). However, particles were not ordered nor equally spaced, which is confirmed by the low probability of normalised inter-particle distance S^* (center-to-center distance between adjacent particles divided by the particle diameter) distribution at $L/D = 400$ for all Deborah De number values, as displayed in Figure 4.2a and b). However, there were peaks in the probability function at $S^* = 1$, meaning that particles were forming strings of particles in contact, mainly doublets at $L/D = 400$. Our work has attributed the formation of particle strings or doublets to the existence of multiple connections with varying internal diameters between the reservoir and the microfluidic channel. Specifically, we have found that these differences in diameter size play a crucial role in the formation of the doublets [26]. For example, when a large concentration of particles experience a series of geometrical contractions and expansions, particle overcrowding might occur between the connections, this results in doublet formation. Numerical simulations have demonstrated that as the distance between adjacent particles becomes smaller than a critical value, particles experience an attractive force that leads to doublet formation (Figure 2.4 and Figure 2.5). We did not have optical access to observe particle flow in different connections; therefore, we could not make a clear conclusion on this point. However, since particle strings tended to form mostly doublets at $L/D = 400$, this suggests that particle overcrowding at consecutive connections may have led to string formation [205].

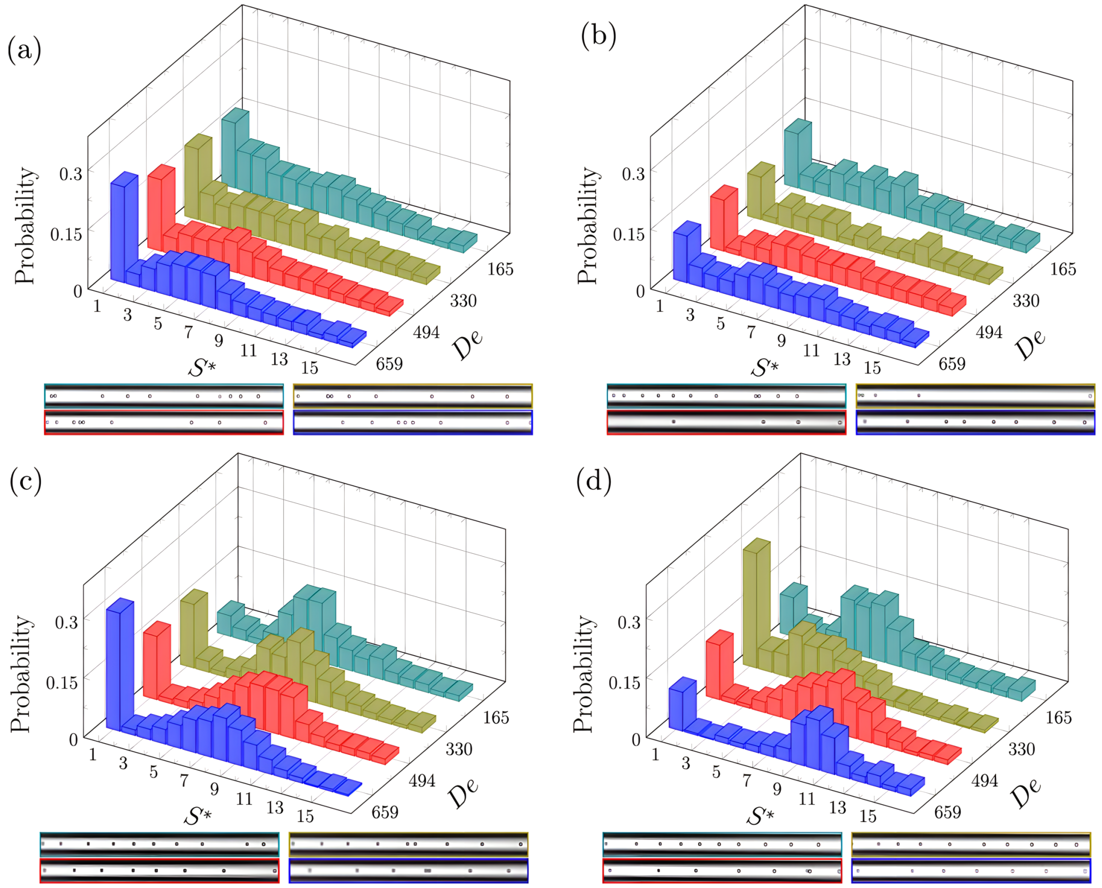

Figure 4.2: Histograms of the normalized distance $S^* = s/d$ for different Deborah numbers De: 659, 494, 330 and 165. (a) $L/D = 400$ and (c) $L/D = 2500$, for a particle bulk concentration of $\phi = 0.2$ wt %. (b) $L/D = 400$ and (d) $L/D = 2500$, for $\phi = 0.3$ wt %. For both ϕ values, no clear peak distribution was observed at $L/D = 400$ except the one at $S^* = 1$, which denotes the formation of doublets or triplets of particles in contact. Particles exhibit self-assembly at $L/D = 2500$ for all De values. The inter-particle distance depends upon the Deborah number De. As displayed in colour coded experimental snapshots for different De values. This figure was reprinted from Jeyasountharan et al 2021 [26].

Our results showed that at $L/D = 400$ particles focused quickly on channel centerline but no self-assembled structures were observed. But doublets were present at $L/D = 400$, represented by $S^* = 1$. In contrast, particles formed self-assembled trains at $L/D = 2500$, which is displayed in Figure 4.2c and d. This suggests that preliminary particle focusing with sufficient channel length is needed to achieve self-assembled particles in microfluidic flow, which is in agreement with previous studies on both viscoelastic [26, 27, 126] and inertial ordering [36, 85]. In section 4.3, we describe the formation of particle train in XG solution.

4.3 Particle train formation in a shear thinning XG aqueous solution

As described in the previous section, we observed relatively quick particle focusing on the channel centerline at $L/D = 400$, but particles were not self-assembled (Figure 4.2a and b). However, at a distance of 25 cm from channel inlet (represented as $L/D = 2500$) there were significant peaks in the distribution of S^* at all De values (Figure 4.2c and d). Such peak distribution denotes the existence of a preferential inter-particle distance and the formation of self-assembled particle trains, as displayed in the experimental snapshots in Figure 4.2c and d. Our results are in good agreement with previous experimental work by Del Giudice et al 2018 [27], Liu et al 2020 [126] and numerical simulation by D'Avino and colleagues [49, 123].

We employed two bulk particle concentrations $\phi = 0.2$ and 0.3 wt %. For $\phi = 0.2$ wt %, we observed peaks in the S^* distributions at $L/D = 2500$ between $7 < S^* < 8$ for all De values (Figure 4.2c). This is in agreement with previous the experimental results by Del Giudice et al, 2018 [27], where the inter-particle distance was found to be independent of *De* values. For increasing values of *De*, the preferential distance moved from $S^* = 7$ to $S^* = 8$ and the peak at $S^* = 1$ also increased (Figure 4.2c). Since there is an increase in the number of particles that form doublets or triplets denoted as $S^* = 1$, the equilibrium distance of the particles in the train must also increase. Taken together, these observations suggest that the equilibrium distributions at $L/D = 2500$ are unaffected by the Deborah number and slight deviations are due to the presence of a different amount of particles forming strings that, in turn, depend on the initial inter-particle distances (see discussion below).

For a higher bulk particle concentration $\phi = 0.3$ wt %, the peak in the inter-particle distance distribution was still visible at $L/D = 2500$ but the value of S^* strongly depended on the Deborah number (Figure 4.2d). The peak progressively moved to higher inter-particle distances as *De* increases. A possible explanation for this behaviour is that the particle train did not reach a stable regime yet, by further increasing the distance from the channel inlet, the S^* distributions in Figure 4.2d would change. As previously shown, train dynamics is strongly affected by inter-particle distance variation and is more relevant at high particle concentrations as the particles are on average closer to each other, which enhances the hydrodynamic interactions [123]. Another explanation for an increase in S^* as De values increase is related to the concentration fluctuations that cause variations in inter-particle distances (Figure 4.2d), which is discussed in the following section [31].

Overall, the S^* distributions reported in Figure 4.2c and d also showed the existence of a relevant peak at $S^* = 1$, which denotes the formation of doublets and triplets of particles in contact. We observed peaks at $S^* = 1$ for all the investigated conditions in Figure 4.2, the peaks were also present relatively close to the channel inlet (L/D = 400), suggesting that this was related to the initial particle distribution rather than an effect of the particle ordering. Since, particle overcrowding occurs at $L/D = 400$. In addition, numerical simulations have reported that for two aligned particles with a distance smaller than a critical value, fluid viscoelasticity generated an attractive force leading to doublet formation (Figure 2.4). The doublet could be hardly separated during the flow [49, 123]. This was confirmed by our experimental distributions where (except the case at $\phi = 0.2$ wt % and De = 165) the peak at $S^* = 1$ remained nearly constant or increased from $L/D = 400$ to $L/D = 2500$ (Figure 4.2a-d). The formation of doublets and triplets is detrimental for particle ordering and should be avoided. For example, downstream applications concerning particle encapsulation for single-cell analysis requires isolated particles [55]. In this regard, designing a microfluidic device aimed at increasing the distance between particles and reducing the occurrence of doublets and triplets might help. An example of such a device was recently reported by Liu et al 2020 [126] where a complex serpentine-like microfluidic channel was developed to prevent doublet and triplet formation. In addition, an experimental apparatus with less microfluidic connections between the sample reservoir and the device would be beneficial to reduce the occurrence of doublet and triplet formation, which currently accounts for about 20 % of the overall particles in our experiments (Figure 4.3). Furthermore, minimising the number of consecutive connections may be beneficial for train dynamics. Since particle overcrowding will be less likely to occur as a result of reduced geometrical expansions and contractions between microfluidic connections. This aspect is later investigated in section 4.6.

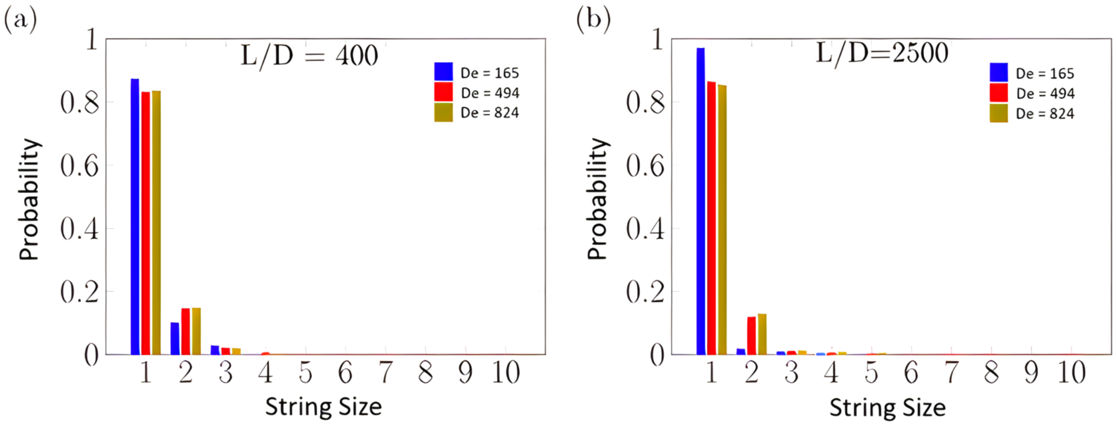

Figure 4.3: Probability distribution of string size as a function of Deborah numbers: 165, 494 and 824 for $L/D = 400$ (a) and (b) $L/D = 2500$. Most particles (≥ 80 %) are isolated, represented by string size = 1 and only a minority (≤ 20 %) form strings of doublets (string size = 2) or 3 triplets (string size = 3). This figure was reprinted from Jeyasountharan et al 2021 [26].

4.4 Effect of local particle concentration on particle train formation

Particle concentration has a relevant effect on the train dynamics. Particle concentration can be modified by simply increasing or reducing the number of particles in the stock solution, and this results in a higher or lower preferential inter-particle distance. However, this is not true in microfluidic applications involving the flow of solid particulate because of the well-known problem of concentration fluctuations in flow [26, 31]. As we observed in the experimental work, there is fluctuations in the number of particles per frame. This is despite our efforts to uniformly mix the particle stock solution in a vortex stirrer prior to introducing the particles in the micro channel. In general, concentration fluctuations mean that flowing particles may experience different ordering dynamics because the number of interacting particles over time is different [27, 123]. For a fixed nominal bulk concentration, the actual concentration of particles observed in a frame may vary over time, thus making it not possible to understand the overall dynamics of the particle train for each bulk concentration.

To clarify the effect of particle concentration on the train formation as if there were no concentration fluctuations, we introduced the concept of local particle concentration ϕ_l (see equation (3.5)). Due to the fluctuations of particles flowing in the microfluidic device per unit time, we observed that the local concentration was in general different from the bulk concentration (Figure 4.4). We identified all the independent frames with the same number of particles (i.e. the same local concentration) for all videos analysed. For each local concentration, we evaluated the average distribution of S^* as a function of the Deborah number De (Figure 4.5).

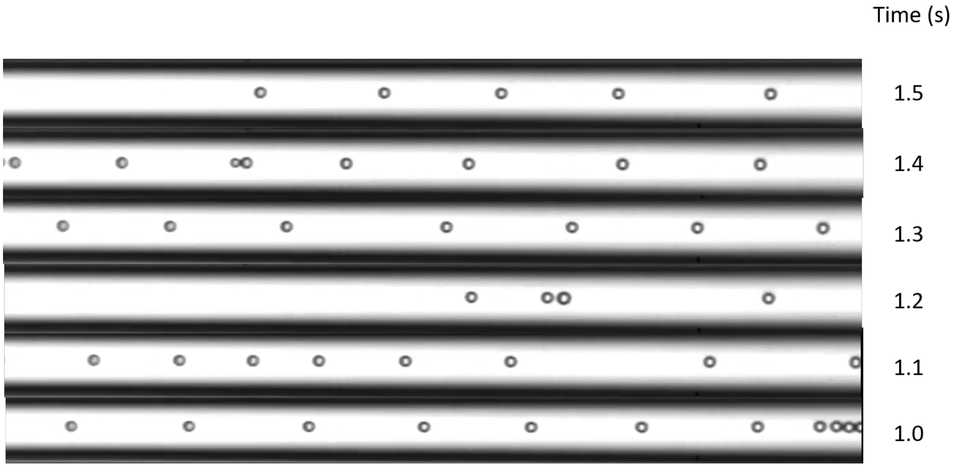

Figure 4.4: Experimental snapshots of concentration fluctuation observed in flowing particles at a bulk volumetric concentration $\phi = 0.25$wt % suspended in 0.1wt % Xanthan Gum XG at various times (seconds). This figure was reprinted from Jeyasountharan et al 2021 [26].

As shown in Figure 4.5. we did not observe any clear peak in the distribution of inter-particle distances S^* at $L/D = 400$. This is in agreement with our previous observations for different bulk concentrations at $L/D = 400$ (Figure 4.2a and b). There was not enough length for train dynamics to occur at $L/D = 400$ [202]. However, when moving the observation point to $L/D = 2500$, there were peaks in the inter-particle distance at $S^* = 1$ and $6 < S^* < 8$ (Figure 4.5c and d). This is in line with results shown in (Figure 4.2c and d). In addition, by increasing the local particle concentration, the peak at $S^* = 1$ increased as well. This suggests that that a higher local particle concentration enhanced the formation of doublets and triplets. These results, together with recent numerical simulations [123] and other experiments, [27, 126] let us conclude that larger particle concentrations have to be avoided in the interest of a more uniform train formation. There may be a range of favorable particle concentrations for which a train can be formed: if the particle concentration is too low, then no train would formed due to weak hydrodynamic interactions between adjacent particles; on the other hand, if the particle concentration is too large, then particle doublets or triplets can form and disrupt the continuity of the train. This is also in line with similar observations on particle trains formed in inertial flows [33, 35, 31]. In section 4.5, we demonstrate the effect of Deborah number on particle sting formation. For example how does an increase or decrease in Deborah number increase or reduce the formation of particle strings in flow.

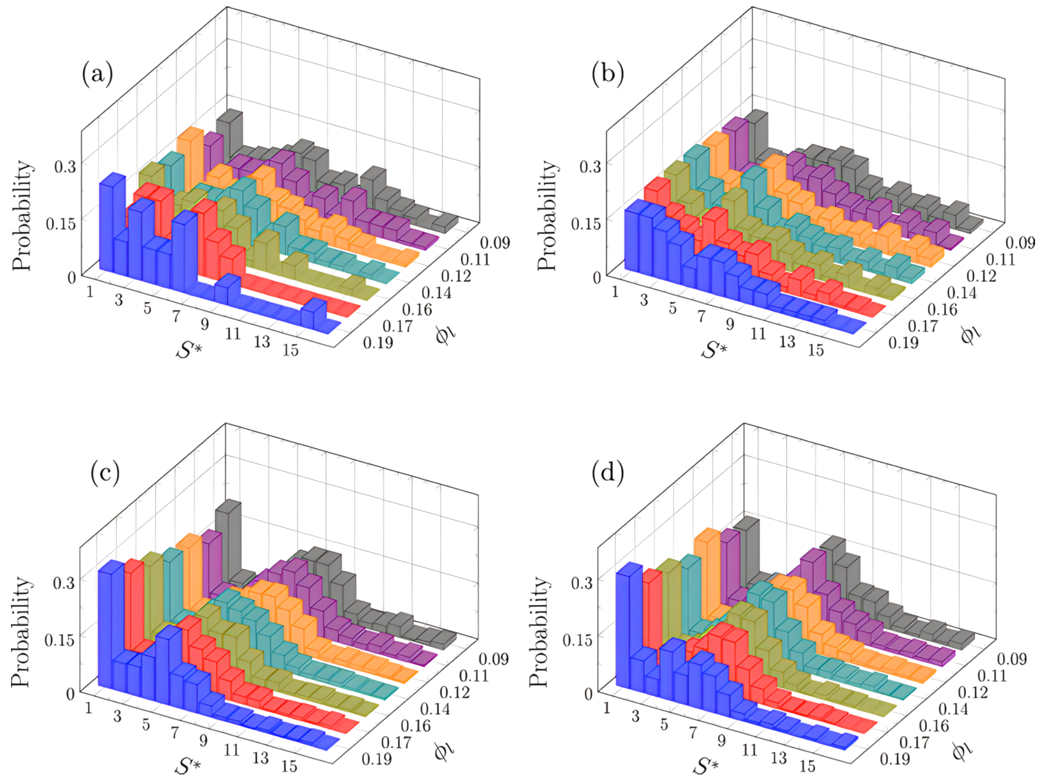

Figure 4.5: Histograms of the normalized distance $S^* = s/d$ for different local particle concentrations ϕ_l and for $De = 165$ at volumetric flow rate ($Q = 5\ \mu$L/min). (a) $L/D = 400$ and (c) $L/D = 2500$, respectively for a particle bulk concentration of $\phi = 0.2$ wt %. (b) $L/D = 400$ and (d) $L/D = 2500$, respectively and for $\phi = 0.3$ wt %. Higher ϕ_l increased the probability of doublet and triplet formation ($S^* = 1$) [123]. This figure was reprinted from Jeyasountharan et al 2021 [26].

4.5 The effect of Deborah Number on multi-particle string formation at various local particle concentrations

In the following section, we proceed to study the effect of the Deborah number on multi-particle string (i.e., doublets, triplets, etc.) formation as a function of the local particle concentration. First, we plot a master chart to represent the probability of forming multi-particle strings at different local particle concentrations for the three Deborah numbers De: 165, 494 and 822 (Figure 4.6). From Figure 4.6 it is clear that as De values increased, we observed an increase in the probability of doublet and triplet formation for each local particle concentration. When the bulk particle concentration is fixed, an increase of the Deborah number results in a higher probability of doublet or triplet formation. For instance, at $\phi_l = 0.09$ and at $De = 165$, we observed less than 10% of the particles forming doublets or triplets; an increase of Deborah to $De = 822$ resulted in around 20% multi-string particles. This can be elucidated by the fact that when De values increase, the volumetric rate increases, (see equation (3.2)). Therefore, particles in flow may experience greater attractive forces and form multi-stings at large particle concentration i.e. doublets and triplets, ect Figure 4.3 [49]. Our results demonstrate that large particle concentrations result in the formation of multi-strings of particles such as doublets and triplets. This phenomenon is further accentuated when increasing the Deborah number even for relatively low values of the local particle concentration.

Overall, the results so far confirmed that elastic fluids with shear thinning features (0.1 wt % XG) can be used to form particle train in microfluidic flow. This is in line with previous experimental findings [27, 126]. In addition, numerical simulations have demonstrated the dynamics of train formation for particle pairs and triplets suspended in shear thinning liquids [49, 123]. For a suspending liquid, either shear thinning or near constant-viscosity, determine the "likeliness" of experiencing attraction or repulsion, which was also found to depend on the critical distance between the two adjacent particles, as displayed in Figure 2.4 and Figure 2.5. In other words, particles can form multi-strings i.e. doublets or triplets when they become closer than the critical distance required to "activate" the attractive forces; otherwise, particles would repel and likely form particle trains. Our observations are in line with previous findings, as we observed particle focusing at $L/D = 400$ then self-assembly of particle trains at $L/D = 2500$. Together with the presence of doublets and triplets ($S^* = 1$), as reported in Figure 4.2. As previously remarked, it is important to control the way adjacent particles interact with each other by properly designing a simple microfluidic channel with minimal connections. This may reduce particle overcrowding between consecutive connections, which may ultimately lower multi-particle i.e. doublet and triplets formation in flow [205]. In section 4.6 we investigate how a simplified microfluidic device set up can reduce multi-particle strings and improve the continuity of trains.

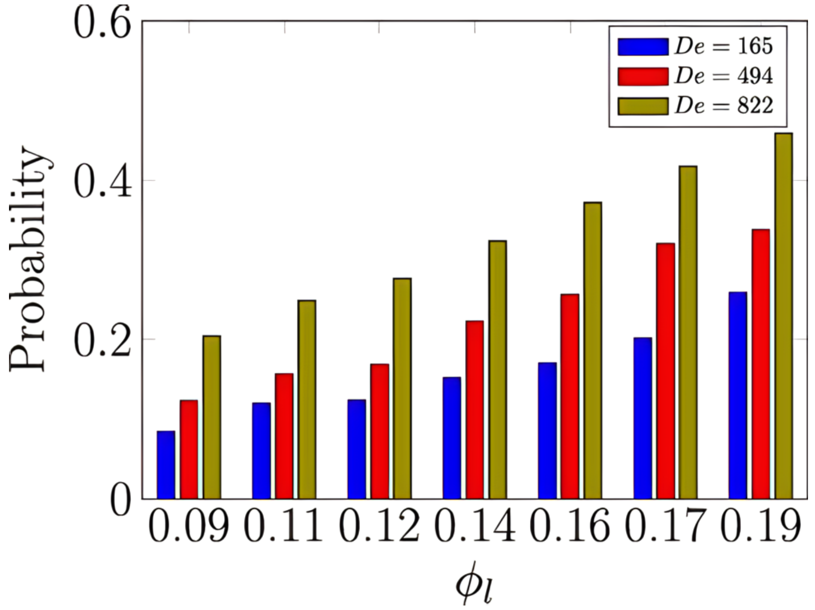

Figure 4.6: Master chart represents probability of multi-particle string (doublets and triplets) formation as a function of local particle concentration ϕ_l at different Deborah De numbers: 165, 494 and 822. An increase of both the *De* number and the ϕ_l promotes doublet and triplet formation. This figure was reprinted from Jeyasountharan et al 2021 [26].

4.6 Simplified microfluidic connections result in a drastic reduction of particle doublets

In previous section, we discussed the occurrence of multi-particle string formation and demonstrated the effect of Deborah number and local particle concentration on multi-particle string formation. We argued that a better designed microfluidic device with less connections could potentially lead to a reduction of such multi-particle strings, improving the continuity of the particle trains. In this section, we carried out experiments with a simplified set-up, where we removed the flow sensor from the pressure pump. Even though we could not read the volumetric flow rate without the flow sensor, the advantage of this approach was a reduction of connections between tubes having different internal diameters, thus reducing the occurrence of flow perturbations that could result in particle aggregation. The configuration without the flow sensor presented a single connecting tube from the vial containing the particle suspension directly to the microfluidic device (Figure 4.7). This means that if particles were properly mixed and no aggregates were present, no multi-particle strings should form unless the distance between adjacent particles fell below the critical distance for particle attraction, which is true at very high bulk particle concentrations, where attractive forces tend to dominate [49].

We used a simplified experimental apparatus to study particle train formation in

0.1 wt % XG at a higher bulk particle concentration, ϕ = 0.4 wt % (Figure 4.7). We employed a higher concentration to investigate whether the continuity of train dynamics improve in the simplified channel. We carried out experiments by imposing the pressure drop in the range 200 < ΔP < 400 mbar. An estimate of the flow rate has been done by measuring the velocity of aligned particles. Specifically, we run numerical simulations of the fluid without particles using the Cross model in to derive the fluid velocity at the axis for an imposed flow rate. Then, we corrected such velocity to account for the presence of a confinement [49] and verified at which flow rate the corrected fluid velocity matched the experimental one [206]. The estimated flow rate range was $0.4 < Q < 3.1$ 20 μL/min resulting in the Deborah number range of $10 < De < 80$.

As displayed in Figure 4.7b. In the whole range of imposed pressure drop, we observed a drastic reduction in multi-particle strings, with more uniform particle trains across the whole ΔP range. The peak in S^* distribution was independent of the imposed pressure drop ΔP and Deborah number values *De*, this in agreement with the results presented previously in Section 4.2 and 4.3. Our results also confirmed that the multi-particle strings observed in Figure 4.2c and d were the result of the initial distribution of particles where doublets and triplets of particles were observed. Most importantly, our results confirmed the fact that both channel design and experimental apparatus are essential to achieve more uniform particle trains in viscoelastic liquids such as XG.

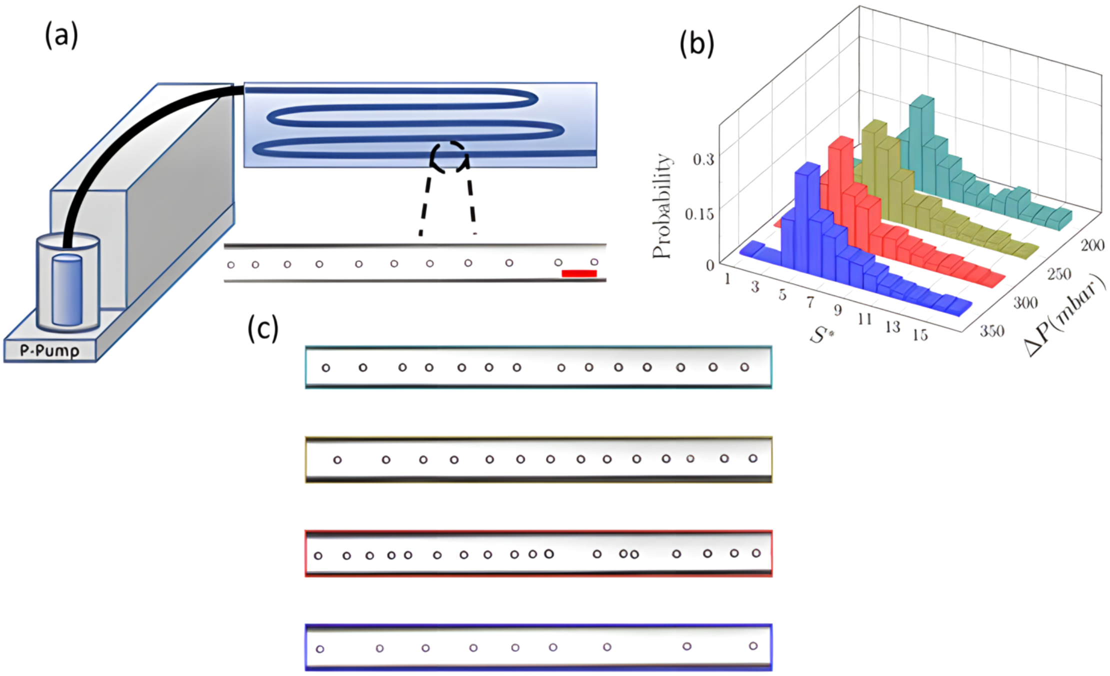

Figure 4.7: (a) Schematic representation of the simplified microfluidic configuration. Scale bar is 100 µm. (b) Histograms of the normalized distance $S^* = s/d$ for different values of the pressure drop ΔP for $L/D = 2500$ and for a particle bulk concentration of $\phi = 0.4$ wt %. (c) Experimental snapshots at different Δ are with the same color coded as the histograms. This figure was reprinted from Jeyasountharan et al 2021 [26].

4.6.1 Summary of the findings

In this chapter we successfully demonstrated that a viscoelastic shear thinning aqueous XG solution 0.1 wt % can be used to self-assemble particles on channel centerline in a commercial serpentine microfluidic device. First, we showed that the particles focused relatively quickly at $L/D = 400$ without the formation of self-assembled structures. Given enough length for particles to interact with each other. Particle train formation was found at $L/D = 2500$, making particle focusing the “prelude” to particle ordering. This is in agreement with previous numerical simulations in viscoelastic liquids [49, 123] and previous studies in inertial flows [36, 207]. Although, we demonstrated self-assembly of particles in microfluidic flow. We did not investigate the progression of self-assembly from $L/D = 400$ to $L/D = 2500$ at various points. Furthermore, it would be interesting to observe how particles train dynamics evolve along the channel length in viscoelastic flow.

To account for particle concentration fluctuations in flow, we developed the concept of local particle concentration, which considers the number of particles in each experimental frame instead of whole system to better understand train dynamics. We found that the preferential distance observed through the distributions of the inter-particle distances depend on the particle concentration and the Deborah number. The distributions were also characterized by a peak at a distance equal to the particle diameter (S^* = 1), denoting the presence of several particles forming doublets or triplets. The peaks at (S^* = 1) was a result of adjacent particles with initial inter-particle distances below a critical value subjected to attractive forces and these particles were hardly separated during flow, this is in agreement with previous numerical simulations [49, 123]. Also, the formation of doublets and triplets were associated with the existence of multiple connections with varying diameters between sample reservoir and microfluidic device. We designed a simplified microfluidic configuration and drastically reduced doublet and triplet formation in flow. In future works, in addition to, simplifying microfluidic device configuration. It may be worth investigating the effect of microfluidic device design on reducing multi-particle string formation in flow.

Chapter 5

Microfluidic device to reduce multi-particle string formation and self-assemble particles in microfluidic flow

5.1 Motivation

In the previous chapter, we successfully demonstrated the self-assembly of particles with a diameter of 20 μm suspended in 0.1 wt % Xanthan Gum (XG). We found that particles tend to focus on channel centerline at $L/D = 400$ and self-assemble at $L/D = 2500$ in a commercial device (Figure 4.2). We also introduced the concept of local particle concentration to account for fluctuations in bulk concentration over time [31]. In addition, we encountered multi-particle string formation in flow, which was detrimental for the continuity of particle trains [27, 49]. Therefore, we simplified the microfluidic configuration and found that the ordering dynamics improved, as we observed dominant S^* peaks for all pressure drops (Figure 4.7b). We suggested that modifying the intrinsic design of the microfluidic device may reduce multi-string formation, as previously shown in experiments [126, 208]. Since, simplifying the external configuration may not be applicable for applications such as micro flow cytometry that require multiple connections to the device [78]. In this chapter, we designed, fabricated and employed a microfluidic device with sixteen trapezoidal elements to reduce the formation of multi-particle strings. Similar to the one proposed by Liu et al, 2020 made of an array of inverted triangle elements [126]. The flow field computed by Liu et al, 2020 revealed that the velocity profile first decreases when the fluid enters each element and subsequently increases, leading to the break-up of multi-particle strings. However, Liu et al 2020 did not quantify the breaking efficiency of multi-particle strings

[126]. In this chapter, we report the quantified efficiency of the device with trapezoidal elements to break multi-particle strings for particles with diameters of 20 and 45 μm suspended in 0.2 wt % XG. The aqueous 0.2 wt % XG is both elastic and shear thinning (Figure 3.3), which essential for particle focusing and self-assembly, as described in Chapter 4. Thus, once we reduce the formation of multi-particle in flow we proceeded to observe the progressive self-assembly of particles along the channel length, which has not been done in any previous studies.

5.2 Microfluidic device to reduce multi-particle strings in Microfluidic flows

In this chapter, we employed a microfluidic device with sixteen trapezoidal elements (Figure 3.4a). After preliminary experiments and iterative designs. We noticed that sixteen trapezoid elements led to the most optimal efficiency in breaking particle aggregates, while a large number of trapezoidal elements (> 16) led to particles sticking to the narrow corners of trapezoidal elements, which disturbed fluid flow. In addition, a complex microfluidic device with large number of trapezoidal elements may be difficult to use for applications such as micro flow cytometry, which benefits from simpler designs. On the contrary, a lower number (< 16) of trapezoidal elements did not break the particle aggregates efficiently.

5.2.1 Quantified breaking efficiency of multi-particle strings for particles with a diameter of 20 μm

For the 20 μm particles, we observed several aggregates at the device inlet, i.e. before entering the series of trapezoidal elements (Figure 5.1a); at the end of the series (trapezoid sixteen), we observed a significant decrease in particle aggregates (Figure 5.1b); subsequently, at the straight section (outlet) there was further decrease in particle aggregates (Figure 5.1c). We quantified the breaking efficiency of the microfluidic device for various imposed pressure drops ΔP: 300, 400, 500 and 600 mbar corresponding to Deborah number *De* values: 271, 478, 800 and 1167 at two different particle bulk concentrations, namely, ϕ = 0.2 wt % and ϕ = 0.3 wt %. We plotted particle frequency as a function of particle string size. For example, particle string size equal 1 represents isolated particles, string size of 2 represents doublets and so on.

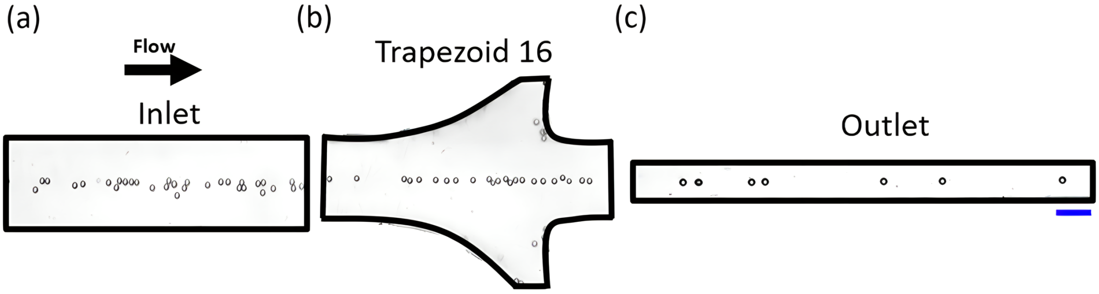

Figure 5.1: Experimental snapshots of suspension of particles with a diameter of 20 μm in 0.2 wt % aqueous Xanthan gum XG solution. We observed particle flow at various points: inlet; trapezoid sixteen and outlet. Particles aggregates were significantly reduced at trapezoid 16 and outlet. Scale bar is 100 μm. This figure was reprinted from Jeyasountharan et al 2022 [202].

For ϕ = 0.2 wt %, at the device inlet (Figure 5.2a), isolated particles accounted for 60–80% of the overall number, depending on the imposed pressure drop. An increase in pressure drop was found to increase the number of aggregates, this is in line with the fact that a larger number of particles would pass from a large tube to a contraction, thus increasing the chances of aggregate formation. While moving towards the outlet of the microfluidic device, we observed a drastic reduction in the number of particle aggregates (Figure 5.2 c), with more than 90% of the particles being isolated.

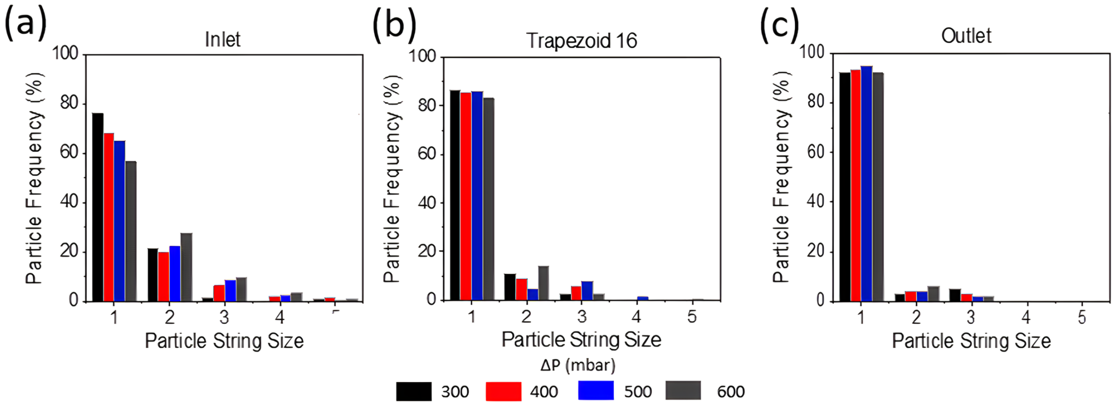

Figure 5.2: Particle frequency as a function of string size for various pressure drops ΔP evaluated at the three observation points: inlet; trapezoid 16 and outlet. For particles at a bulk concentration of ϕ = 0.2 wt %, with a diameter of 20 μm suspended in 0.2 wt % XG. Color-coded legend representing the employed ΔP values are shown below. See Table 3.1 for the corresponding volumetric flow rates for device 1. This figure was reprinted from Jeyasountharan et al 2022 [202].

For a higher particle concentration ϕ = 0.3 wt %, we observed a similar trend, with the only difference that the larger particle concentration resulted in an increased number of aggregates at the inlet. In trapezoidal element sixteen, frequency of isolated particle was 10% lower as compared to trapezoid sixteen for ϕ = 0.2 wt % at all pressure drops (Figure 5.2b). This may be due to an increase in particle aggregates formed at a higher particle concentration, namely ϕ = 0.3 wt % at the inlet. A significant amount of particle aggregates i.e. doublets and triplets was observed at ϕ = 0.3 wt % (Figure 5.3a). Furthermore, regardless of the particle concentration, around 90% of particles were isolated at the end of the device in the outlet section (Figure 5.3c).

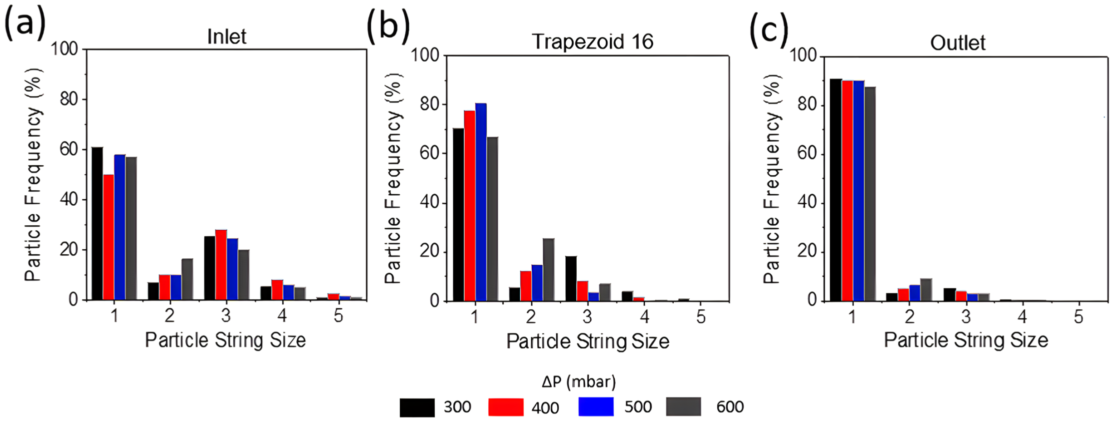

Figure 5.3: Particle frequency as a function of string size for various pressure drops ΔP evaluated at three observation points: inlet; trapezoid 16 and outlet. For particles at a bulk concentration of ϕ = 0.3 wt %, with a diameter of 20 μm suspended in 0.2 wt % XG. Color-coded legend representing the employed ΔP values are shown below. See Table 3.1 for the corresponding volumetric flow rate values for device 1. This figure was reprinted from Jeyasountharan et al 2022 [202].

5.2.2 Quantified breaking efficiency of multi-particle strings for particles with a diameter of 45 μm

Next, we demonstrated that the microfluidic device can also be employed to break particle aggregates for particles with a larger diameter. For particles with a diameter of 45 μm, we quantified the breaking efficiency of the microfluidic device for various imposed pressure drops ΔP: 700, 800, 900 and 1000 mbar corresponding to Deborah number *De* values: 1560, 1933, 2400 and 2833 at bulk particle concentration, ϕ = 0.7 wt %. Similar to the 20 μm particles, we found that the number isolated particles significantly increased from the inlet (see Figure 5.4a) towards the outlet (Figure 5.4c). When particle frequency was quantified as a function of particle string size. We observed 60-80 % isolated particles with 10-20 % aggregates at the inlet (Figure 5.5a) . However at trapezoid element sixteen and outlet there was an even higher percentage of isolated particles (up to 95%) (Figure 5.5b and c).

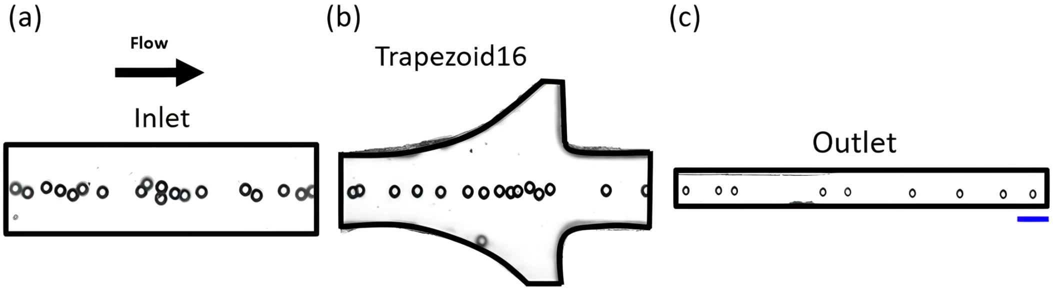

Figure 5.4: Experimental snapshots of suspension of particles with a diameter of 45 μm 0.2 wt % aqueous Xanthan gum XG solution. We observed particle flow at various points: inlet; trapezoid sixteen and outlet. Scale bar is 100 μm. This figure was reprinted from Jeyasountharan et 2022 [202].

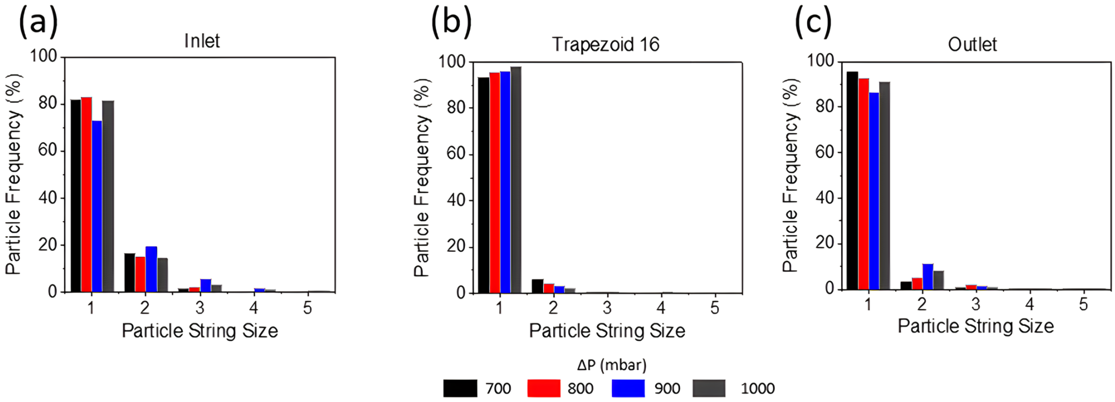

Figure 5.5: Particle frequency as a function of string size for various pressure drops ΔP: 700; 800; 900 and 1000 mbar evaluated at the three observation points: inlet; trapezoid 16 and outlet. Particles at a bulk concentration of ϕ = 0.7 wt %, with a diameter of 45 μm suspended in 0.2 wt % XG. Color-coded legend representing the employed ΔP values are shown below. See Table 3.1 for the corresponding volumetric flow rate values for device 1. This figure was reprinted from Jeyasountharan et al 2022 [202].

5.2.3 Summary of the findings

In summary, we experimentally demonstrated that an array of trapezoidal elements can aid the breaking of particle aggregates regardless of particle size, concentration and imposed pressure drop. We observed that around 90-95 % of overall particles were isolated at the end of the microfluidic device. However, for particles with a diameter of 20 μm we found that an increase in the linear concentration from $\phi = 0.2$ wt % to $\phi = 0.3$ wt % led to an increase in particle aggregate formation i.e. doublets and triplets (Figure 5.2 and 5.3), also in agreement with recent experiments [26]. Numerical simulations by D'Avino and colleagues explain particle aggregate formation in flow, where three aligned particles experience attractive forces below a critical distance (See Figure 2.5) [49, 123]. For example, when the linear particle concentration increase, greater number of particles are present in the micro channel the channel grows, this leads to the possibility of having particles closer to each other, where attractive forces are favoured over repulsive ones [202]. Previous numerical simulations also confirm that particle aggregates are formed when an attractive force exists between consecutive particles at distances below the critical value [49, 123]. A simulation by Liu et al, 2020 [126] elucidates the mechanism behind trapezoid elements on breaking particle aggregates. They demonstrated that fluid velocity in trapezoidal elements is slower than the fluid velocity in the straight channel. Therefore, when the aggregated particles flow into the elements, the velocity of particles slow down. For instance, when a leading particle of the aggregated doublet enters into the straight section, the velocity of the leading particle tends to increase, while the latter particle is slowed down in the trapezoidal element. Due to a differences in velocity between the leading and trailing particle, a separating force breaks the aggregated doublets [126]. Overall, our results demonstrate that a microfluidic device with a series of trapezoid elements can significantly lower the formation of particle aggregates in flow. Our device can be employed in crucial single cell or particle based biomedical applications such as: micro flow cytometry, which often requires isolated particles or cells to be self-assembled prior to analysis for efficient single particle or cell analysis in a high-throughput manner [78]; drop-sequencing requires isolated particles or cells to be simultaneously encapsulated in droplets for parallel analysis [121]. In section 5.2, we successfully designed and employed a microfluidic device with sixteen trapezoidal elements to break particle aggregates for particles with two different diameters. In general particle aggregate occurrence is detrimental for the continuity of train formation, as shown in previous experimental and numerical works [26, 27, 123]. Based on our results, in the following section, we utilise the device with sixteen trapezoidal elements followed by a straight glass capillary to achieve self-assembly of particles without the interference of particle aggregates i.e. doublets and triplets in flow.

5.3 Dynamics of self-ordered structures along a straight microchannel

In the previous section, we successfully employed a microfluidic device with sixteen trapezoidal elements to break particle aggregates in flow. Logically, we now proceed to present the results on particle ordering at different distances from the inlet of a straight glass capillary. Since particle aggregates have a detrimental effect on particle ordering [123], we employed the device described in Section 5.2 followed by a straight glass (See Figure 3.4b). In this way, we reduced the number of particle aggregates to around 5 % of the overall number, thus being able to evaluate the particle self-assembly dynamics with a reduced disturbance caused by the aggregates.

For particles with a diameter of 20 μm, suspended in 0.2 wt % XG, flow was imposed in a circular glass capillary with an internal diameter equal 100 μm. The corresponding confinement ratio β was 0.2. We observed the evolution of particle self-assembly along the length of the glass capillary at every 5 cm ($L/D = 500$) from the capillary inlet (right after the end of the array of trapezoidal elements) until 25 cm ($L/D = 2500$). In general, there was a progressive self-assembly of particles from $L/D = 500$ to $L/D = 2500$, as displayed in the experimental snapshots (Figure 5.6).

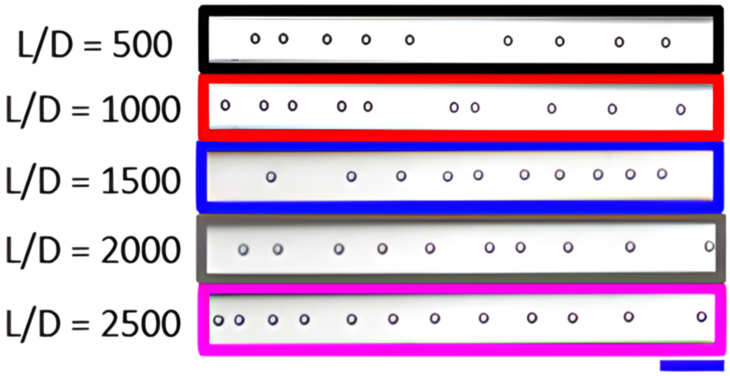

Figure 5.6: Experimental snapshots of 20 μm particles suspended in 0.2 wt % Xanthan Gum XG at different normalized channel length L/D values, where L is the distance from the capillary inlet and D is the capillary diameter (increasing from top to bottom). Progressive self-assembly of particles were along the length of the glass capillary glass from $L/D = 500$ to $L/D = 2500$. Scale bar is 100 μm. This figure was reprinted from Jeyasountharan et al 2022 [202].

At $L/D = 500$ from the capillary inlet, particles were focused on the centerline but were not ordered for all imposed pressure drops and corresponding volumetric flow rate values (Figure 5.6 and 5.7). This is in line with our previous finding, where particles focused on channel centerline relatively quickly at ($L/D = 400$) but formed self-assembled at longer distances from the inlet ($L/D = 2500$) in a serpentine microfluidic device [26]. For example at an imposed pressure of ΔP = 300 mbar corresponding to

(Q ≈ 0.5μL/min, De ≈ 13), particles at L/D: 500; 1000 and 1500 did not display any ordering, as clear from the lack of a peak in the S^* distribution (Figure 5.7a). However, as we observe progression of particle ordering along the length of the glass capillary (Figure 5.6). We saw a clear peak distribution for $S^* \simeq 5$, at $L/D = 2500$ for all pressure drops (Figure 5.7). The same trend was observed when increasing the pressure drop up to 600 mbar (Q ≈ 5.5μL/min, De ≈ 146). In addition to experimental results, present numerical simulations clearly demonstrated that viscoelastic ordering is a slow phenomenon and require long distances from the inlet to attain a self-ordered structure [202].

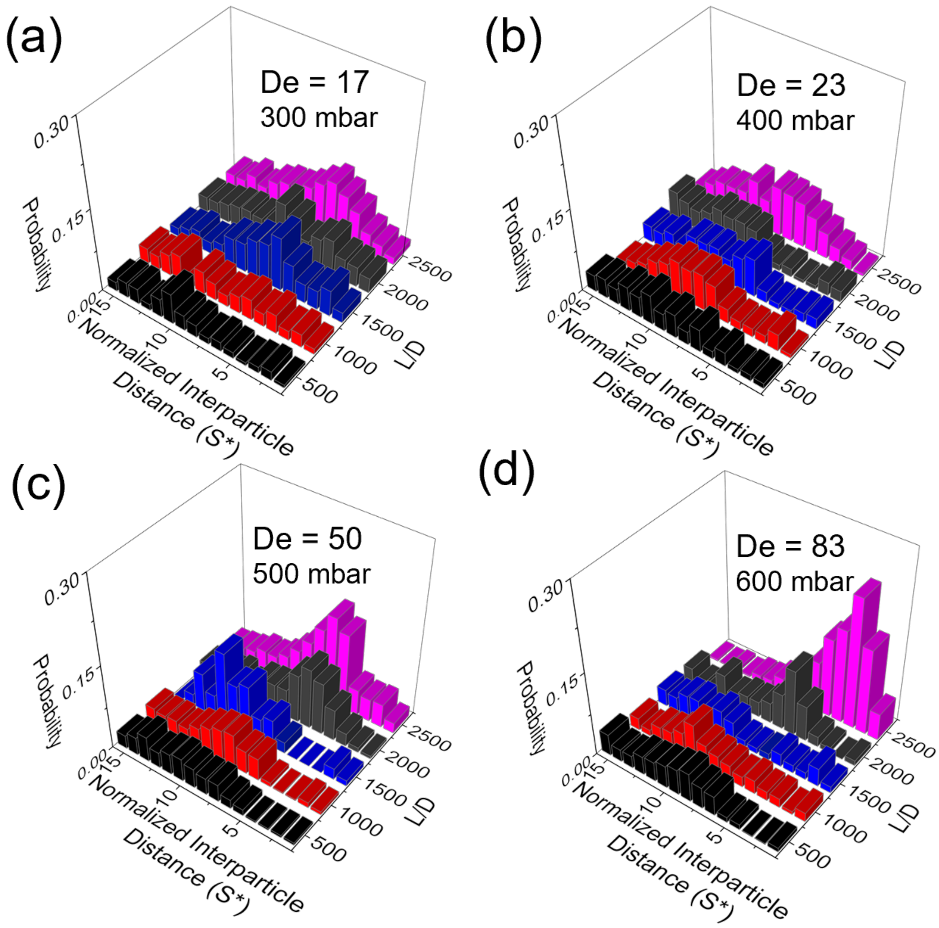

Figure 5.7: Probability distribution of the normalized distance between consecutive particles $S^* = s/d$ (s equals center to center distance and d is the particle diameter) for a bulk particle concentration of $\phi = 0.2$ wt % as a function of L/D at different imposed pressure drops and Deborah numbers. This figure was reprinted from Jeyasountharan et al 2022 [202].

Once we increase the bulk particle concentration to ϕ = 0.3 wt %, we observed similar ordering dynamics to ϕ = 0.2 wt %. For instance self assembly of particles progressively evolves from $L/D = 500$ to $L/D = 2500$. At $L/D = 500$, we notice that particles focus on the centerline but were not ordered. At $L/D = 2500$, we observe clear S^* distribution for all imposed pressure drops and corresponding volumetric flow rate values (Figure 5.8). In addition, we also observe that the spatial distribution of S^* varies less at a higher bulk particle concentration. In general, more particles tend to occupy the same channel volume at a higher particle concentration this can lead to: less variation in spatial distribution; and larger number of particle aggregate formation. Overall our results suggest that, for a confinement ratio β of 0.2, particles focus on the channel centerline relatively quickly. Particles progressively self assemble from the inlet $L/D = 500$ towards the outlet, $L/D = 2500$. However, train of equally spaced particles in viscoelastic liquids may require significant channel length, even larger than $L/D = 2500$ at β value of 0.2 for optimal self-assembly to occur.

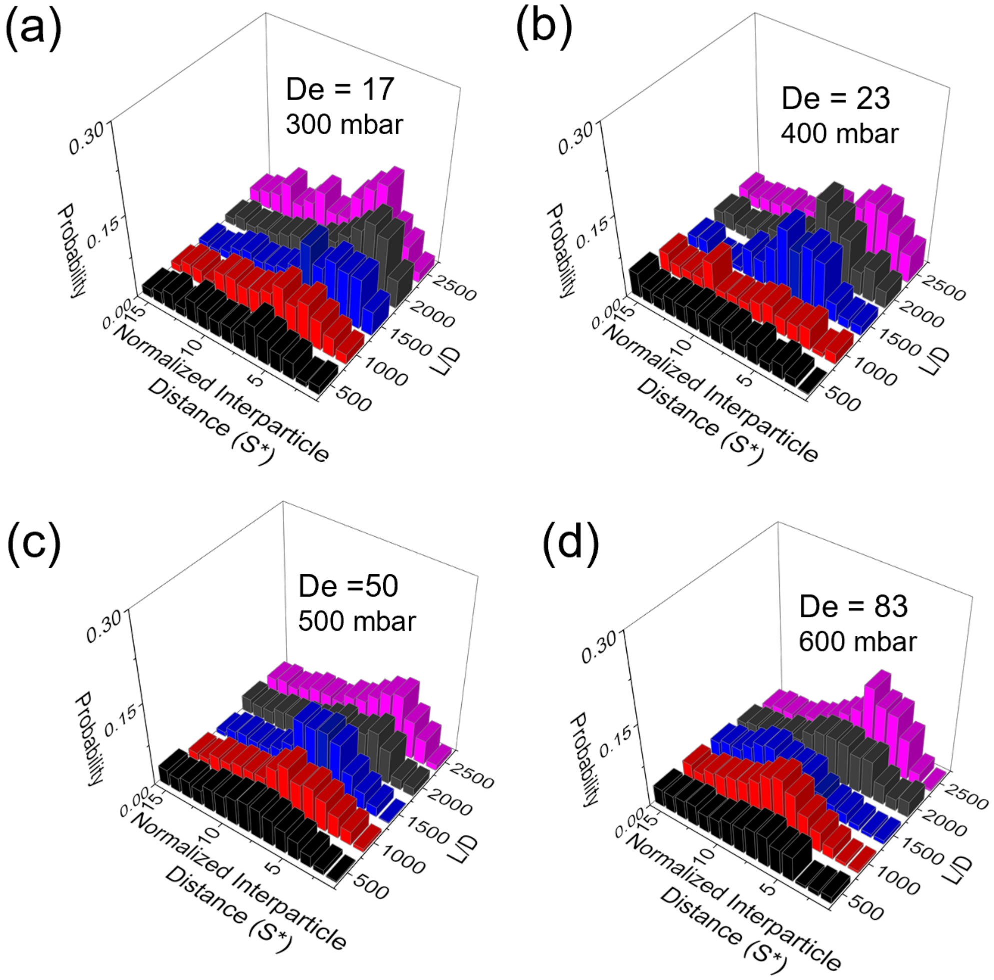

Figure 5.8: Probability distribution of the normalized distance between consecutive particles $S^* = s/d$ (s equals center to center distance and d is the particle diameter). For Particles with a diameter of 20 μm at a bulk particle concentration of $\phi = 0.3$ wt % as a function of L/D at different imposed pressure drops and Deborah numbers. This figure was reprinted from Jeyasountharan et al 2022 [202].

From our results, it is clear that optimal self-ordered structures at $\beta = 0.2$ require sufficient channel lengths even greater than $L/D = 2500$ for optimal ordering dynamics. However, it is not always feasible to increase the length of the glass capillary. As long capillaries with an internal diameter of 100 μm are fragile and tend to break easily. Very recently, numerical simulation has demonstrated that self-ordered structures formed closer to the channel inlet at $\beta = 0.4$ as compared to $\beta = 0.2$ [123, 194, 202]. Based on these findings, we then repeated the same set of experiments to observe evolution of self-assembly for particles with a diameter of 45 μm, which corresponds to $\beta = 0.45$.

At variance with the 20 μm particles, we observed a preferential spacing already at $L/D = 1000$ (10 cm from the capillary inlet), confirming that a larger confinement ratio promoted a faster transition to a self-ordered structure, this is in good agreement with the numerical simulation [202] (Figure 5.9 and 5.10). We also observed that the spatial distribution of S^* varied less significantly with the channel length compared to $\beta = 0.2$. For instance, at ΔP = 900 mbar and ΔP = 1000 mbar, there is no significant difference between the distribution of particle spacing between $L/D = 2000$ and $L/D = 2500$. This is compatible with the fact that the ordering dynamics tend to slow down after achieving a Gaussian-like shape around the S^* peak (Figure 5.10). To form a train of equally spaced particles in viscoelastic liquid requires a significant channel length, even larger than $L/D = 3000$, and such a distance increases for small confinement ratios. In this regard, it should also be mentioned that the migration dynamics of the particles towards the centerline in shear thinning liquids occur before ordering dynamics at β values ≥ 0.2 [26, 59] . However, ordering dynamics itself is affected by the channel length and β [194, 202].

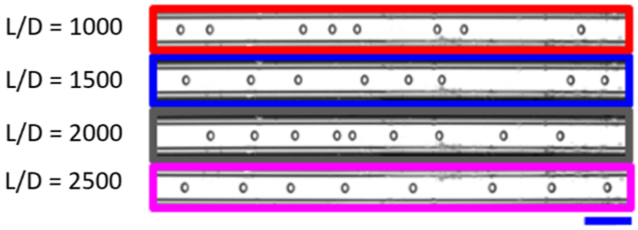

Figure 5.9: Experimental snapshots of 45μm particles suspended in 0.2 wt % Xanthan Gum XG at different normalized channel length L/D values, where L is the distance from the capillary inlet and D is the capillary diameter (increasing from top to bottom). Progressive self-assembly of particle was observed along the length of the glass capillary. Scale bar is 100 μm. This figure was reprinted from Jeyasountharan et al 2022 [202].

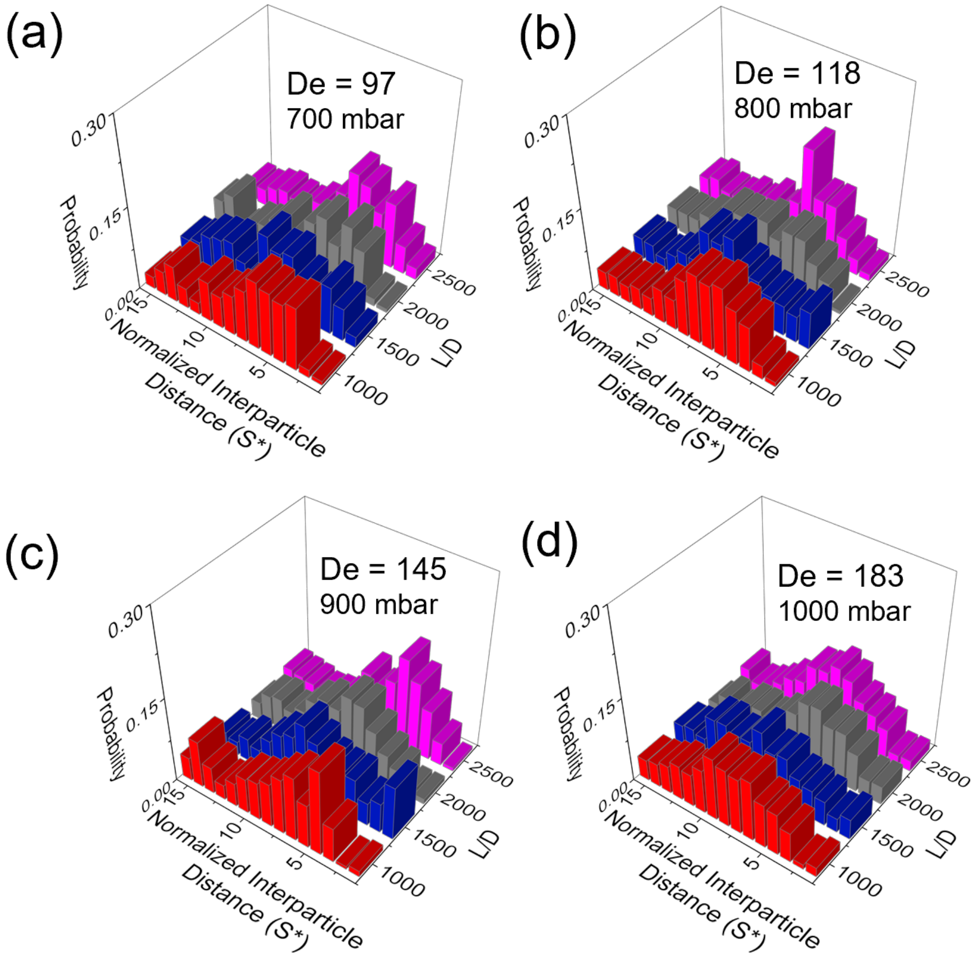

Figure 5.10: Probability distribution of the normalized distance between consecutive particles $S^* = s/d$ (s equals center to center distance and d is the particle diameter). For Particles with a diameter of 45μm at a bulk particle concentration of $\phi = 0.7$ wt % as a function of L/D at different imposed pressure drops and Deborah numbers. This figure was reprinted from Jeyasountharan et al 2022 [202].

From our results, it is evident that confinement ratio has a quantitative effect on the channel length required to achieve particle ordering. In addition, formation of linear particle trains through inertial effects is also affected by varying confinement ratio [37], where the spacing between the particles increases as the confinement ratio increases. This is a direct consequence of the displacement of the lateral equilibrium position attained by a single particle as the confinement ratio is varied. For instance, as $\beta << 1$, the particles approach the Segré and Silberberg equilibrium position [81], whereas, as the confinement ratio increases, the equilibrium position shifts toward the centerline due to steric effects, [92, 207, 209, 210] affecting, in turn, the particle–wall hydrodynamic interactions and the average train velocity. Consequently, the required channel length to achieve ordering and the resulting particle spacing are a non-trivial function of the confinement ratio. In contrast, particles suspended in elastic and shear thinning fluids migrate to the channel centerline regardless of their size for $\beta \geq 0.2$ [59, 116]. In addition, the ordering dynamics is roughly the same as the confinement ratio is varied, allowing to easily estimate the required channel length to achieve a certain ordering efficiency. This is useful in applications concerning single-cell analysis, which requires relatively quick formation of self-assembled cells for an implementable, high-throughput, relatively inexpensive and a parallel approach for compartmentalized analysis of single-cells [211], DNA [212] and drug-screening [213] in droplets [214]. For example optimal encapsulation of circulating tumour cells from blood cells requires non-overlapping ordered structures to reduce reagent demand, sample volume and analysis time [215]. Technologies such as Drop-Sequencing analysing genome transcripts of individual cells in droplets require non-overlapping ordered cells for deterministic encapsulation [122].

5.3.1 Summary of the findings

In summary, we designed a microfluidic device made of an array of trapezoidal elements similar to the one employed by Liu et al 2020 and demonstrated that our device was able to significantly reduce the percentage of particle aggregates in flow for particles with two different diameters (20μm and 45μm) at various bulk particle concentrations. To observe self-assembly of particles without the interference of particle aggregates, we used the device with sixteen trapezoidal elements and attached a 30 cm long circular capillary made of glass. We the observed particle self-assembly at different distances from the inlet of a straight glass capillary, at every 5 cm (L/D = 500). For both particle diameters (20μm and 45μm) we found that particles progressively self-assembled from $L/D = 500$ towards $L/D = 2500$, since there was peak distribution in S^*. In agreement with our experimental results, numerical simulations demonstrated that 45 μm particles with a confinement ratio $\beta = 0.45$ self-assembled at shorter distances from the channel inlet compared to 20 μm particles, which had a β value of 0.2. Overall, our devices can: break particle aggregates and lead to particle self-assembly for two different sized particles. Based on our results, our device consisting of an inlet structure with sixteen trapezoidal elements along with sufficient channel length for particle self-assembly can be employed in compartmentalized analysis of cells or particles. As mentioned previously encapsulation of particles and cells in droplets using microfluidic device is flourishing in fields ranging from biomedicne to tissue engineering. In biomedicine, particle or cell encapsulation in droplets provides a high-throughput platform for single cell and particle analysis [216]. In tissue engineering, preserving temporal resolution of tissues in a droplet for long periods may be important for analytical framework to obtain key biological information [217]. Therefore, in Chapter 6 we incorporated our device inlet consisting of trapezoidal elements to reduce the occurrence of particle aggregates and employed a spiral structure to allow enough length for particle ordering dynamics to occur. Ideally, we want to encapsulate isolated self-assembled particle structures in oil droplets by matching the frequency of droplet generation to particles arriving at the encapsulation site.

Chapter 6

Viscoelastic droplet generation and particle encapsulation in a T-junction microfluidic device

6.1 Motivation

In the previous chapter, we demonstrated that a microfluidic device with sixteen trapezoidal elements can be used to reduce the formation of multi-particle strings for particles with two different diameters, namely 20 μm and 45 μm. In addition, we studied the ordering dynamics for both particle diameters and found that self-assembly of particles depend on channel length and β [202]. For instance, at β of 0.45 particles self-assembled at shorter distances compared to β values of 0.2. In this chapter, we employed a T-junction device with sixteen trapezoidal element to reduce multi-particle string formation, followed by a serpentine channel length for particle ordering dynamics to occur prior to the T-junction site (encapsulation area) (see Figure 3.5). At the T-junction site, we encapsulated particles with a diameter of 20 μm in droplets. The particles were suspended in 0.1 wt % hyaluronic acid HA (dispersed phase) and mineral oil was the continuous phase. We used HA instead of xanthan gum XG as the lead suspending fluid, as we previously observed that XG polymer solution degrades after a short period compared to HA [218]. Our aim was to reduce the occurrence of multi-particle strings and form self-assembled structures prior to the encapsulation area to identify experimental conditions for which the encapsulation efficiency was larger than the Poisson limit.

6.2 Droplet Formation in Newtonian and Non-Newtonian fluids

In this section, we first studied the Newtonian and Non-Newtonian (viscoelastic) droplet formation phenomenon from a qualitative prespective at various imposed flow rate ratios Q_d/Q_c, where Q_d is the flow rate of the dispersed phase (i.e., either PBS or HA) and Q_c is the flow rate of the continuous mineral oil phase [24, 169]. For the same set of imposed volumetric flow rate values, the droplet size did not differ significantly between Newtonian and non-Newtonian droplets, this is in agreement with previous findings on viscoelastic droplet microfluidics [24, 169, 191, 219, 220, 221, 222, 223, 224]. However, we observed a clear difference in the dynamics of droplet formation between Newtonian and non-Newtonian droplets, with the presence of satellite droplet formation only observed for the non-Newtonian case, which is in agreement with previous findings featuring formation of viscoelastic droplets made of aqueous xanthan gum solutions in a commercial T-junction device [225].

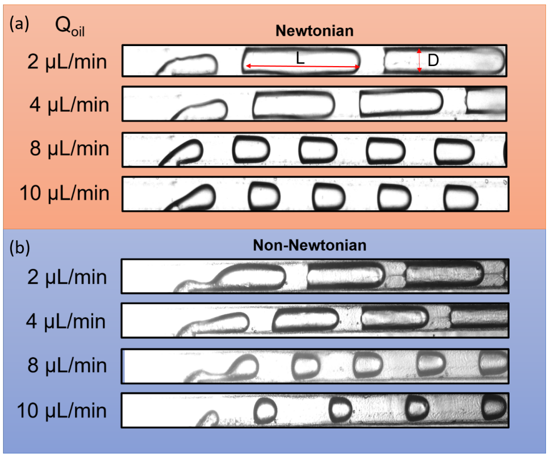

Figure 6.1: Experimental snapshots of droplet generation at various continuous phase (oil) flow rates Q_{oil}. (a) For the Newtonian case, phosphate buffer saline (PBS) is employed as the dispersed phase. (b) For the non-Newtonian case, hyaluronic acid (HA) at a mass concentration of 0.1 wt % is used as dispersed phase. Satellite droplet formation is only observed in the non-Newtonian case. The volumetric flow rate of the dispersed phase is 8 μL/min in both cases.

6.3 The effect of flow rate ratio on Droplet size for Newtonian and non-Newtonian fluids

We quantified the droplet length L normalised by the channel width $W = 100\ \mu$m, as a function of the ratio between the flow rate of the dispersed and the continuous phase (Figure 6.2a-b). For Newtonian droplets (Figure 6.2b), we observed that all the data scaled on a mastercurve given by the expression $L/W = 1 + 2\,(Q_{PBS}/Q_{oil})$, this is in agreement with previous findings [160]. We also observed that the normalised droplet length for non-Newtonian droplets scaled identically to the Newtonian case (Figure 6.2b), which is in line with the qualitative observations in Figure 2.6, and also previous works on viscoelastic droplet microfluidics [24, 169, 191, 219, 220, 221, 222, 223, 224].

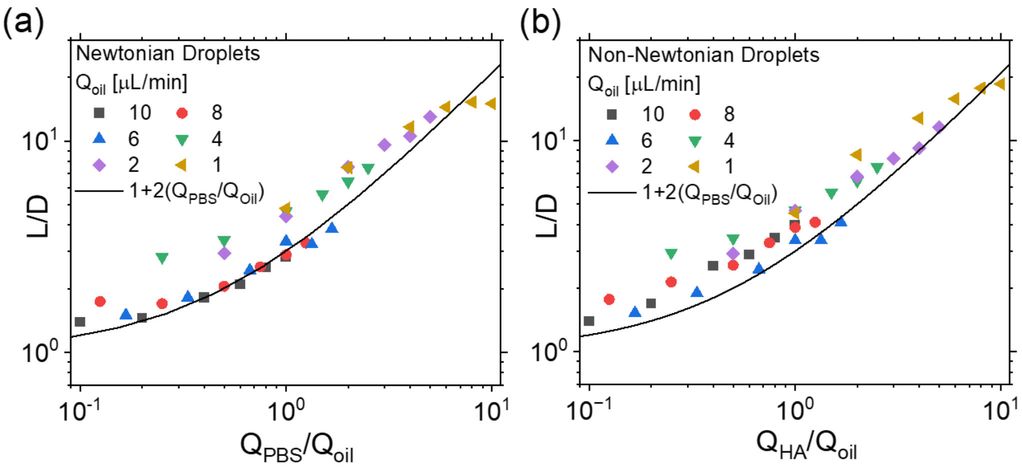

Figure 6.2: Normalised droplet size L/W, where L is the droplet length and $W = 100\ \mu$m is the channel width (see experimental snapshot in Figure 2.6, as a function of the ratio Q_{PBS}/Q_{oil} for the Newtonian droplets (a) and Q_{HA}/Q_{oil} for the non-Newtonian droplets (b). Q_{PBS} and Q_{HA} are the flow rates of PBS and HA, respectively, while Q_{oil} is the flow rate of the mineral oil. The solid line in a) and b) is $L/W = 1 + 2\,(Q_{PBS}/Q_{oil})$, meaning that the non-Newtonian data in b) collapse on the master curve for Newtonian droplets.

6.4 Frequency of Droplet generation for a non-Newtonian fluid

In addition to the normalised droplet size, we quantified the frequency of droplet formation (see Figure 6.3). Manipulating the frequency of droplet generation is an important step in achieving controlled encapsulation of particles [24, 74, 169, 100]. Since the Poisson stochastic limit can be overcome only when the frequency of droplet formation f_d is equal to the constant frequency of equally-spaced particles f_p approaching the encapsulation area. Our experimental data demonstrated that for droplets made of HA in PBS scaled according to the expression, $f_d = A\,(Q_{HA}Q_{oil})^B$ with $A = 1.64 \pm 0.18$ and $B = 2/3$. As displayed in Figure 6.3 our experimental data was highly scattered, this may be due to fluctuations in individual flow rate values of both Q_{HA} and Q_{oil}. The parameter A was obtained by fitting the data set with flow rate values in the units of μL/min, while B was fixed to $B = 2/3$ according to the scaling introduced by Shahrivar and Del Giudice [24] for xanthan gum solutions. The only difference was the value of the parameter A, which corresponded to a vertical shift. In our work A was around 5 times smaller compared to [24]. This discrepancy can be due to factors, including different rheological properties between HA and xanthan gum, or differences in microfluidic device employed by Shahrivar and Del Giudice [24], which was made of glass with a hydrophobic coating, while here we employed PMMA bonded to glass via an adhesive tape. However, the fact that the exponent $B = 2/3$ is identical in both works may suggest a general scaling trend for particle encapsulation in T-junction geometries, but more studies are required to demonstrate this trend in T-junction geometries. For example, studying encapsulation efficiency in other viscoelastic suspending fluids.

Overall, our data on droplet formation suggests that the dynamics of droplet formation was different between the Newtonian and non-Newtonian case, the droplet size remained substantially unchanged. Furthermore, the data related to the frequency of droplet formation scaled with the same exponent as the data presented previously [225]. Future works are required to understand how changes in suspending fluid, micro channel coating and geometry may affect the frequency of droplet generation in microfluidic flow. Manipulating the frequency of droplet generation is crucial for achieving controlled encapsulation of particles in droplets. In section 6.5, we employ the microfluidic device to encapsulate 20 μm particles in droplets. Our aim is achieve controlled encapsulation above the Poisson limit.

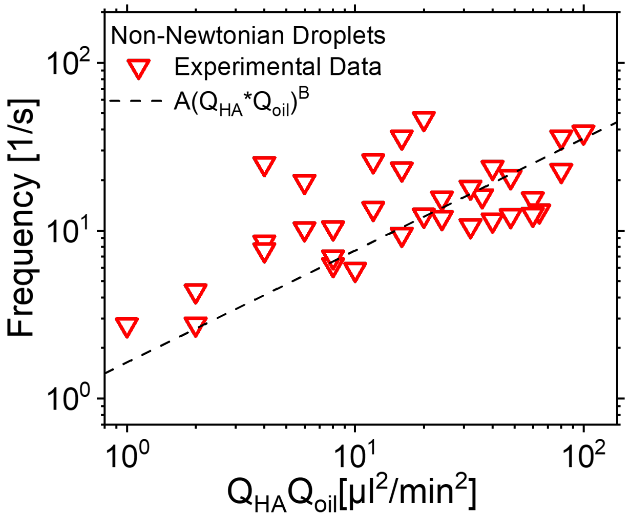

Figure 6.3: Frequency of non-Newtonian droplet generation as a function of the product $Q_{HA}Q_{oil}$. Data points collapse on the master curve $f_{drop} = A\,(Q_{HA} \times Q_{oil})^B$ with $A = 1.64 \pm 0.18$ and $B = 2/3$. The parameter A was obtained by fitting the entire data set with flow rate values in the units of μL/min, while B was fixed to $B = 2/3$ according to the previously introduced by Shahrivar and Del Giudice [24] for xanthan gum solutions.

6.5 Viscoelastic Encapsulation of particles

In this section, we studied the viscoelastic encapsulation of particles in the T-junction device (Figure 6.4). For a purely stochastic encapsulation, the probability $P(k,n)$ of encapsulating a given number of particles n in a droplet is expressed by $P(k,n) = k^n exp(-k)/(n!)$, where k is the average number of particle per droplet [74, 226]. Most desired conditions concerning droplet microfluidic applications such as drop sequencing benefit from the encapsulation of one particle per droplet, which means the number of encapsulated particles $n = 1$ and an average number of particles per droplet $k = 1$ (represented as solid symbols connected by lines in Figure 6.4). Based on previous works, we expect particles suspended in the shear thinning HA solution in PBS to be equally-spaced prior to reaching the T-junction (encapsulation site). This is due to the viscoelasticity mediated hydrodynamic interactions between consecutive particles [24, 27, 169], which means the particles arrive at the T-junction at a constant frequency. Since, we can control the frequency of droplet generation based on flow rate ratios. In theory, if the frequency of droplet generation is synchronised with the frequency of particles arriving at the T-junction. We expect to achieve controlled encapsulation efficiency above Poisson limits. Therefore, we compared the viscoelastic encapsulation data against the stochastic Poisson value to see whether we could ‘beat’ the Poisson limits by taking advantage of the viscoelastic particle ordering, this approach was used in viscoelastic [24, 169] and inertial [100, 190] encapsulation studies.

For a volumetric flow rate of the continuous phase $Q_{Oil} = 2$ μL/min, we observed that the viscoelastic single encapsulation efficiency was always lower than the Poisson limit for all dispersed phase flow rate values (Figure 6.4a). However, when we increased the volumetric flow rate of the dispersed phase to $Q_{Oil} = 4$ μL/min, we observed an improvement in encapsulation efficiency over the Poisson limit for $Q_{HA} = 4$ μL/min (Figure 6.4b). The encapsulation efficiency further improved at $Q_{oil} = Q_{HA} = 8$ μL/min, where we observed an encapsulation efficiency of around 50%, which is significantly larger than the Poisson value at around 36% (Figure 6.4c). At $Q_{Oil} = 8$ μL/min, there was only one value of HA flow rate, namely ($Q_{HA} = 8$ μL/min) for which the encapsulation efficiency was above the Poisson limit. This can be elucidated by the fact that achieving encapsulation efficiencies above the Poisson limit is based on the frequency of droplet formation f_d being synchronised with the frequency of particles approaching the encapsulation area f_p. Since for viscoelastic ordering the volumetric flow rate has only a minor effect on the f_p value [26, 27, 202]. We only observed a single value of Q_{HA} that can significantly beat the Poisson limit for a given value of Q_{Oil}. Furthermore, it is possible that there may not be a volumetric flow rate for which $f_p = f_d$. Since the value of f_d is controlled by volumetric flow rates of both continuous and dispersed phase [24, 160, 169]. Another reason for not achieving encapsulation efficiencies above the Poisson limits may be due to fluctuations in the local concentration of particles approaching the encapsulation area, which is a common unsolved problem encountered when dealing with large particle concentrations [26, 31]. As mentioned in previous works, two consecutive particles could experience different hydrodynamic interactions depending on the initial distance between them. This in turn affects the stability and the continuity of a particle train. It is worth mentioning despite concentration fluctuations, we still managed to achieve encapsulation efficiency larger than the Poisson limit. Finally, we increased the flow rate of oil to $Q_{Oil} = 10$ μL/min, we did not observe any value for HA flow rate, which led to encapsulation efficiency above the Poisson limit. This suggests that at $Q_{Oil} = 10$ μL/min, the frequency of particles arriving at the T-junction did not match the frequency of droplet formation, which may be due variety of reasons mentioned above.

In a previous work by Shahrivar and colleagues on viscoelastic encapsulation in a commercial T-junction device using aqueous xanthan gum solutions as the dispersed phase [24], the authors demonstrated an encapsulation efficiency in the range of 50% to 60%, which beat the Poisson limits. In comparison to Shahrivar and colleagues, we achieved a slightly lower encapsulation efficiency of around 50%. This can be due to a variety of factors. For example, xanthan gum employed by Shahrivar and colleagues presented more shear thinning properties than HA employed in our work. The shear thinning feature of the suspending fluid is important to drive the self-assembly of particles on the channel centerline, as previously shown in numerical simulations [49, 123] as well as in experiments [27]. In our work, the reduction in the shear thinning magnitude of the HA compared to previous works [27, 169] was due to the addition of PBS salt. Since, the addition of salt alters the rheological properties of the suspending solution, which causes a reduction in the shear thinning properties [59, 227]. However, despite a reduction in shear thinning behaviour we still observed particle ordering and achieved an encapsulation efficiency above the Poisson limit. In this case, we employed PBS in HA as opposed to deionized water because PBS is essential for working with cells i.e. culturing cells. This paves the way to design viscoelastic fluids in PBS to study cell ordering and encapsulation dynamics, which may provide insights into optimising single cell-based technologies such as drop sequencing.

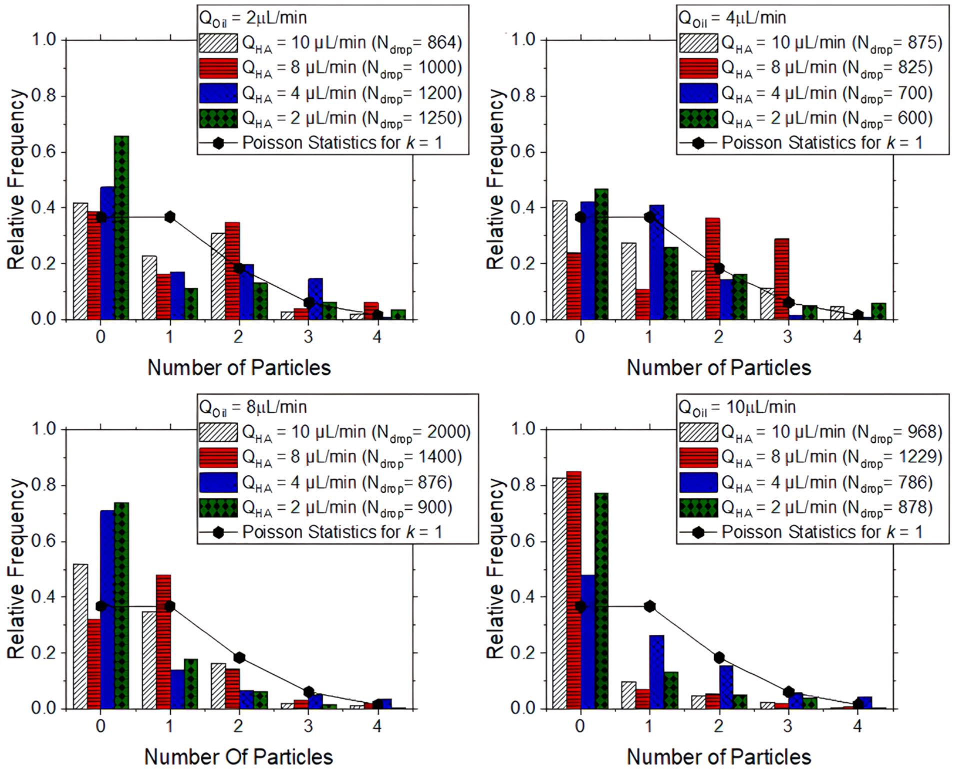

Figure 6.4: Viscoelastic particle encapsulation for a hyaluronic acid (HA) dispersed phase and a mineral oil continuous phase. (a-d) represents histograms of relative frequency as a function of particles per droplet for fixed oil flow rate Q_{oil} values. For each Q_{oil} value, the flow rate of the HA Q_{HA} was varied in the range 2 to 10 μL/min. The Poisson statistics value for $k = n = 1$ is represented by the solid symbols. A single particle encapsulation efficiency above the Poisson stochastic value was obtained for Q_{oil}=Q_{HA} $= 4\mu$L/min (b) and Q_{oil}=Q_{HA} $= 8\mu$L/min (c).

6.5.1 Predicting the optimal conditions to achieve encapsulation efficiency above the Poisson limit

In accordance with previous studies [24, 169], we derived an expression to predict the optimal conditions for particle encapsulation above the Poisson limit. As mentioned previously, the frequency of particles approaching the encapsulation site should match the frequency of droplet generation. The frequency of particles approaching the encapsulation site is given as $f_p = u\phi_l/d$, where u is the particle velocity, d is the particle diameter, and ϕ_l is the local particle concentration defined as [26] $\phi_l = Nd/L$, where N is the number of particles in a given channel length (this is fixed by the experimental observation window) and L is the length of the experimental observation window [24, 26, 27, 169].

The frequency of droplet formation is given by the expression $f_d = A\left(Q_{HA}Q_{oil}\right)^B$, where $A = 1.64 \pm 0.18$ and $B = 2/3$. When the frequency of droplet formation $f_d = A\left(Q_{Oil}Q_{HA}\right)^B$ equals the frequency of particles approaching the encapsulation area $f_p = u\phi_l/d$, this results in the expression:

$$Q_{Oil} = \frac{1}{Q_{HA}}\left(\frac{u\phi_l}{Ad}\right)^{\frac{1}{B}}, \tag{6.1}$$

Based on this expression, we may be able to predict ideal continuous phase flow rate values to achieve encapsulation efficiencies above the Poisson limits. However, variations experimental systems may lead to discrepancies.

6.5.2 Summary of the findings

In summary, we studied the viscoelastic encapsulation phenomenon identifying only two conditions for which the encapsulation efficiency was above the Poisson limit, namely, $Q_{Oil} = Q_{HA} = 4\ \mu$L/min (with efficiency $\simeq 40\%$) and $Q_{Oil} = Q_{HA} = 8\ \mu$L/min (with efficiency $\simeq 50\%$). We also observed that the mathematical expression to evaluate the best conditions for controlled encapsulation was identical to the one proposed earlier [24], with the only difference of a vertical shifting factor for the data.

Chapter 7

Conclusion

In this thesis, several contributions have been made to the area of viscoelastic microfluidics. In Chapter 4: (1) we successfully self-assembled particles in a shear thinning fluid; (2) addressed particle concentration fluctuations in microfluidic flows as if there were no fluctuations, with the concept of local particle concentration; (3) developed an approach to reduce particle aggregate formation in flow i.e. by simplifying the microfluidic configuration. In Chapter 5 we: (1) designed and fabricated a microfluidic device with trapezoid elements to reduce particle aggregate formation; (2) observed progressive self-assembly of particles and also the effect of confinement ratio on particles in viscoelastic flows. In Chapter 6 we: (1) studied the viscoelastic droplet formation and encapsulation of particles in a fabricated T-junction microfluidic device, which consisted of an inlet with sixteen trapezoidal elements followed by sufficient length for particle ordering; (2) Identified only two conditions for which the encapsulation efficiency was above the stochastic Poisson limit, based on frequency of droplet generation matching the frequency of particles arriving at the encapsulation site.

In Chapter 4, we demonstrated that a viscoelastic shear thinning aqueous XG solution 0.1 wt % promoted the self-assembly of particle trains on the centerline of a serpentine microfluidic device. We showed that the particles focused relatively quickly ($L/D = 400$) even though no clear self-assembled structure could be observed. Particle train formation was found at $L/D = 2500$, thus making particle focusing the "prelude" to particle ordering, in agreement with previous numerical simulations in viscoelastic liquids [27, 126] as well as previous studies in inertial flows [36, 207]. We found that the preferential distance observed through the distributions of the inter-particle distances depended on the particle concentration and the Deborah number. The distributions were also characterized by a significant peak at a distance equal to the particle diameter, $S^* = 1$ denoting the presence of several particles forming doublets or triplets. These were ascribed to the fact that adjacent particles with initial inter-particle distances below a critical value were subjected to viscoelasticity-mediated attractive forces and were hardly separated during the flow, this is in agreement with previous numerical simulations [49, 123]. Since the existence of these structures is detrimental for particle ordering, new channel designs need to be developed to avoid their formation. Therefore, we also introduced the concept of local particle concentration to better understand the dynamic of train formation experimentally as if there were no particle concentration fluctuations. We observed that large local particle concentrations resulted in the formation of multi-strings of particles. This phenomenon was accentuated when increasing the Deborah number, even for relatively low values of the particle concentration. Finally, we demonstrated that removing microfluidic connections between the reservoir and the device resulted in a more uniform particle train formation.

In Chapter 5, we designed and fabricated a microfluidic device made of an array of trapezoidal elements similar to Liu et al, 2020 [126] and demonstrated that such structure was able to significantly reduce the percentage of particle aggregate formation. We experimentally demonstrated progressive self-assembly of particles with two diameters, namely 20 μm and 45 μm and provided variations in self-ordering dynamics at two confinement ratios $\beta = 0.2$ and 0.45. We found that for a fixed tube diameter D, larger particles tended to self-order at shorter channel distances compared to smaller particles, which was in agreement with numerical simulations [202].

Finally in Chapter 6, we studied the viscoelastic encapsulation of particles in a T-junction microfluidic device, using hyaluronic acid 0.1 wt% in PBS as suspending liquid. We observed that the data for viscoelastic droplet formation scaled with the same scaling as the Newtonian ones, thus suggesting that the droplet size is not affected by the fluid rheology significantly, in agreement with previous works [24, 219, 221, 223, 224]. We also observed that the frequency of droplet generation scaled as $f_d = A\left(Q_{HA}Q_{oil}\right)^B$ with $A = 1.64 \pm 0.18$ and $B = 2/3$. The parameter A was obtained by fitting the data set with flow rate values in the units of μL/min, while B was fixed to $B = 2/3$ according to the exponent previously introduced by Shahrivar and Del Giudice [24] for xanthan gum solutions. The only difference was the value of the parameter A, which simply corresponded to a vertical shift. We also studied the viscoelastic encapsulation of particles, identifying only two conditions for which the encapsulation efficiency was above the Poisson limit, namely, $Q_{Oil} = Q_{HA} = 4$ μL/min (with efficiency $\simeq 40\%$) and $Q_{Oil} = Q_{HA} = 8$ μL/min (with efficiency $\simeq 50\%$). We also observed that the mathematical expression to evaluate the best conditions for controlled encapsulation was identical to the one proposed by [24], with the only difference of a vertical shifting factor for the data.

Overall, our results from Chapters: 4, 5 and 6 are of interest in many microfluidic applications including flow cytometry [9], single cell-based droplet encapsulation [11, 84] and tissue engineering [68]. Our results can lead to novel optimized methodologies for flow cytometry and particle/cell separation by combining viscoelastic ordering, microfluidic device design with electro-viscoelastic migration [228]. In addition, the formation of isolated self-assembled particle and cell structures may be essential for transforming the single-cell analysis landscape, where controlled encapsulation of cells and particles in a droplet with minimal aggregates is vital for improving applications such as Drop-sequencing. This enables complex single-cell information to be decoded without interference from multiple cells.

7.1 Future Directions

Future works are needed to identify additional viscoelastic liquids where particle trains can be formed. According to the existing literature, [27, 123] shear thinning is a required feature to obtain particle trains, and our findings suggest the same. Future studies regarding viscoelastic particle train formation in other polymer solutions such as polyethylene oxide or polyacrylamide (widely used for particle/cell manipulation are required [107]. Similarly, other studies where fluids with nearly constant-viscosity are employed as suspending liquids would provide additional insights into the particle train formation mechanism. Additionally, it is important to clarify the impact of attractive and repulsive forces between consecutive particles as a function of the fluid rheology, as only limited experiments exist [26, 27, 126, 202]. Additional work is required to understand the potential effect of channel geometry (e.g., different cross sections and overall design) on reducing multi-particle string formation and on the self-ordering dynamics. Furthermore, in droplet microfluidics understanding the dynamics of droplet generation and particle/cell encapsulation has huge potential to improve several biomedical applications. For example, controlled sequences of cells in droplets is desirable in digital polymerase-chain-reaction (PCR) for accurate detection of genetic information in cells and single-cells analysis require encapsulation systems with 100 % efficiency [120]. In tissue engineering, droplet-based microfluidic systems are used to produce building blocks of artificial tissues and organs, such as shape-controlled micro particles and microfibers [229]. We also anticipate that new machine learning algorithms [230] have the potential to optimise experimental parameters to improve single particle encapsulation efficiencies above Poisson limit. For example, developing particle tracking algorithms to predict the experimental conditions such flow rate values required to synchronise the frequency of particles arriving at the encapsulation site to the frequency of droplet generation may improve controlled encapsulation efficiencies above the Poisson limits.

Bibliography

[1] A. Burklund, A. Tadimety, Y. Nie, N. Hao, and J. X. Zhang, "Advances in diagnostic microfluidics," in *Advances in Clinical Chemistry*, pp. 1–72, Elsevier, 2020.

[2] I. Azzouz and K. Bachari, "MEMS devices for miniaturized gas chromatography," in *MEMS Sensors - Design and Application*, InTech, jul 2018.

[3] S. Terry, J. Jerman, and J. Angell, "A gas chromatographic air analyzer fabricated on a silicon wafer," *IEEE Transactions on Electron Devices*, vol. 26, pp. 1880–1886, dec 1979.

[4] J. Chen, D. Chen, Y. Xie, T. Yuan, and X. Chen, "Progress of microfluidics for biology and medicine," *Nano-Micro Letters*, vol. 5, pp. 66–80, mar 2013.

[5] N. Convery and N. Gadegaard, "30 years of microfluidics," *Micro and Nano Engineering*, vol. 2, pp. 76–91, mar 2019.

[6] E. K. Sackmann, A. L. Fulton, and D. J. Beebe, "The present and future role of microfluidics in biomedical research," *Nature*, vol. 507, pp. 181–189, mar 2014.

[7] H. Afsaneh and R. Mohammadi, "Microfluidic platforms for the manipulation of cells and particles," *Talanta Open*, vol. 5, p. 100092, aug 2022.

[8] S. woon Choe, B. Kim, and M. Kim, "Progress of microfluidic continuous separation techniques for micro-/nanoscale bioparticles," *Biosensors*, vol. 11, p. 464, nov 2021.

[9] L. S. Cram, "Flow cytometry, an overview," in *Advanced Flow Cytometry: Applications in Biological Research*, pp. 1–9, Springer Netherlands, 2003.

[10] Y. Zhou, Z. Dong, H. Andarge, W. Li, and D. Pappas, "Nanoparticle modification of microfluidic cell separation for cancer cell detection and isolation," *The Analyst*, vol. 145, no. 1, pp. 257–267, 2020.

[11] C. Beck and M. Goksr, "Microfluidics in single cell analysis," in *Advances in Microfluidics*, InTech, mar 2012.

[12] Y. Chen, P. Li, P.-H. Huang, Y. Xie, J. D. Mai, L. Wang, N.-T. Nguyen, and T. J. Huang, "Rare cell isolation and analysis in microfluidics," *Lab on a Chip*, vol. 14, no. 4, p. 626, 2014.

[13] E. Dzierzak and M. de Bruijn, "Isolation and analysis of hematopoietic stem cells from mouse embryos," in *Hematopoietic Stem Cell Protocols*, pp. 001–014, Humana Press.

[14] B. Bruijns, A. van Asten, R. Tiggelaar, and H. Gardeniers, "Microfluidic devices for forensic DNA analysis: A review," *Biosensors*, vol. 6, p. 41, aug 2016.

[15] J. Wu, R. Kodzius, W. Cao, and W. Wen, "Extraction, amplification and detection of DNA in microfluidic chip-based assays," *Microchimica Acta*, vol. 181, pp. 1611–1631, dec 2013.

[16] Y. Liu and H. Lu, "Microfluidics in systems biology — hype or truly useful?," *Current Opinion in Biotechnology*, vol. 39, pp. 215–220, jun 2016.

[17] A. Manz, D. Harrison, E. M. Verpoorte, J. Fettinger, A. Paulus, H. Lüdi, and H. Widmer, "Planar chips technology for miniaturization and integration of separation techniques into monitoring systems," *Journal of Chromatography A*, vol. 593, pp. 253–258, feb 1992.

[18] A. M. Streets and Y. Huang, "Chip in a lab: Microfluidics for next generation life science research," *Biomicrofluidics*, vol. 7, p. 011302, jan 2013.

[19] G. M. Whitesides, "The origins and the future of microfluidics," *Nature*, vol. 442, pp. 368–373, jul 2006.

[20] K. Oh, "Multidisciplinary role of microfluidics for biomedical and diagnostic applications: Biomedical microfluidic devices," *Micromachines*, vol. 8, p. 343, nov 2017.

[21] N. W. Choi, M. Cabodi, B. Held, J. P. Gleghorn, L. J. Bonassar, and A. D. Stroock, "Microfluidic scaffolds for tissue engineering," *Nature Materials*, vol. 6, pp. 908–915, sep 2007.

[22] M. Karimi, S. Bahrami, H. Mirshekari, S. M. M. Basri, A. B. Nik, A. R. Aref, M. Akbari, and M. R. Hamblin, "Microfluidic systems for stem cell-based neural tissue engineering," *Lab on a Chip*, vol. 16, no. 14, pp. 2551–2571, 2016.

[23] J. P. Conde, N. Madaboosi, R. R. Soares, J. T. S. Fernandes, P. Novo, G. Moulas, and V. Chu, "Lab-on-chip systems for integrated bioanalyses," *Essays in Biochemistry*, vol. 60, pp. 121–131, jun 2016.

[24] K. Shahrivar and F. Del Giudice, “Controlled viscoelastic particle encapsulation in microfluidic devices,” *Soft Matter*, vol. 17, no. 35, p. 8068–8077, 2021.

[25] T. Tsuji, Y. Matsumoto, R. Kugimiya, K. Doi, and S. Kawano, “Separation of nano- and microparticle flows using thermophoresis in branched microfluidic channels,” *Micromachines*, vol. 10, p. 321, may 2019.

[26] A. Jeyasountharan, K. Shahrivar, G. D’Avino, and F. Del Giudice, “Viscoelastic particle train formation in microfluidic flows using a xanthan gum aqueous solution,” *Analytical Chemistry*, vol. 93, no. 13, p. 5503–5512, 2021.

[27] F. D. Giudice, B. V. Cunning, R. S. Ruoff, and A. Q. Shen, “Filling the gap between transient and steady shear rheology of aqueous graphene oxide dispersions,” *Rheologica Acta*, vol. 57, no. 4, p. 293–306, 2018.

[28] L. Wang, L. A. Flanagan, N. L. Jeon, E. Monuki, and A. P. Lee, “Dielectrophoresis switching with vertical sidewall electrodes for microfluidic flow cytometry,” *Lab on a Chip*, vol. 7, no. 9, p. 1114, 2007.

[29] D. D. Carlo, D. Irimia, R. G. Tompkins, and M. Toner, “Continuous inertial focusing, ordering, and separation of particles in microchannels,” *Proceedings of the National Academy of Sciences*, vol. 104, pp. 18892–18897, nov 2007.

[30] K. Zhang, Y. Ren, L. Hou, T. Jiang, and H. Jiang, “Flexible particle focusing and switching in continuous flow via controllable thermal buoyancy convection,” *Analytical Chemistry*, vol. 92, no. 3, p. 2778–2786, 2020.

[31] S. Kahkeshani, H. Haddadi, and D. D. Carlo, “Preferred interparticle spacings in trains of particles in inertial microchannel flows,” *Journal of Fluid Mechanics*, vol. 786, nov 2015.

[32] C. Dietsche, B. R. Mutlu, J. F. Edd, P. Koumoutsakos, and M. Toner, “Dynamic particle ordering in oscillatory inertial microfluidics,” *Microfluidics and Nanofluidics*, vol. 23, may 2019.

[33] Y. Gao, P. Magaud, L. Baldas, C. Lafforgue, M. Abbas, and S. Colin, “Self-ordered particle trains in inertial microchannel flows,” *Microfluidics and Nanofluidics*, vol. 21, sep 2017.

[34] X. Hu, J. Lin, D. Chen, and X. Ku, “Stability condition of self-organizing staggered particle trains in channel flow,” *Microfluidics and Nanofluidics*, vol. 24, mar 2020.

[35] K. J. Humphry, P. M. Kulkarni, D. A. Weitz, J. F. Morris, and H. A. Stone, “Axial and lateral particle ordering in finite reynolds number channel flows,” *Physics of Fluids*, vol. 22, p. 081703, aug 2010.

[36] W. Lee, H. Amini, H. A. Stone, and D. D. Carlo, “Dynamic self-assembly and control of microfluidic particle crystals,” *Proceedings of the National Academy of Sciences*, vol. 107, pp. 22413–22418, dec 2010.

[37] J. Liu and Z. Pan, “Self-ordering and organization of in-line particle chain in a square microchannel,” *Physics of Fluids*, vol. 34, p. 023309, feb 2022.

[38] X. Zhang, A. Kim, and D. Garmire, “Particle-train dynamics in curved microfluidic channels at intermediate reynolds numbers,” *Chemical Engineering Science*, vol. 98, pp. 69–76, jul 2013.

[39] J. Zhang, S. Yan, D. Yuan, G. Alici, N.-T. Nguyen, M. E. Warkiani, and W. Li, “Fundamentals and applications of inertial microfluidics: a review,” *Lab on a Chip*, vol. 16, no. 1, pp. 10–34, 2016.

[40] K. Goda, A. Ayazi, D. R. Gossett, J. Sadasivam, C. K. Lonappan, E. Sollier, A. M. Fard, S. C. Hur, J. Adam, C. Murray, C. Wang, N. Brackbill, D. D. Carlo, and B. Jalali, “High-throughput single-microparticle imaging flow analyzer,” *Proceedings of the National Academy of Sciences*, vol. 109, pp. 11630–11635, jul 2012.

[41] J. Zhou, P. V. Giridhar, S. Kasper, and I. Papautsky, “Modulation of aspect ratio for complete separation in an inertial microfluidic channel,” *Lab on a Chip*, vol. 13, no. 10, p. 1919, 2013.

[42] M. E. Warkiani, B. L. Khoo, L. Wu, A. K. Tay, A. A. Bhagat, J. Han, and C. T. Lim, “Ultra-fast, label-free isolation of circulating tumor cells from blood using spiral microfluidics,” *Nature Protocols*, vol. 11, no. 1, p. 134–148, 2015.

[43] A. A. S. Bhagat, S. S. Kuntaegowdanahalli, D. D. Dionysiou, and I. Papautsky, “Spiral microfluidic nanoparticle separators,” in *Microfluidics, BioMEMS, and Medical Microsystems VI* (W. Wang and C. Vauchier, eds.), SPIE, feb 2008.

[44] D. Liu, M. Sun, J. Zhang, R. Hu, W. Fu, T. Xuanyuan, and W. Liu, “Single-cell droplet microfluidics for biomedical applications,” *The Analyst*, vol. 147, no. 11, pp. 2294–2316, 2022.

[45] J. Zhou, P. Mukherjee, H. Gao, Q. Luan, and I. Papautsky, “Label-free microfluidic sorting of microparticles,” *APL Bioengineering*, vol. 3, p. 041504, dec 2019.

[46] M. E. Rosti and S. Takagi, “Shear-thinning and shear-thickening emulsions in shear flows,” *Physics of Fluids*, vol. 33, p. 083319, aug 2021.

[47] G. D’Avino and P. Maffettone, “Particle dynamics in viscoelastic liquids,” *Journal of Non-Newtonian Fluid Mechanics*, vol. 215, pp. 80–104, jan 2015.

[48] M. M. Denn, “Fifty years of non-newtonian fluid dynamics,” *AIChE Journal*, vol. 50, no. 10, pp. 2335–2345, 2004.

[49] G. D’Avino, M. Hulsen, and P. Maffettone, “Dynamics of pairs and triplets of particles in a viscoelastic fluid flowing in a cylindrical channel,” *Computers & Fluids*, vol. 86, pp. 45–55, nov 2013.

[50] S. Yang, J. Y. Kim, S. J. Lee, S. S. Lee, and J. M. Kim, “Sheathless elasto-inertial particle focusing and continuous separation in a straight rectangular microchannel,” *Lab Chip*, vol. 11, no. 2, pp. 266–273, 2011.

[51] A. M. Leshansky, A. Bransky, N. Korin, and U. Dinnar, “Tunable nonlinear viscoelastic “focusing” in a microfluidic device,” *Physical Review Letters*, vol. 98, jun 2007.

[52] F. Del Giudice, S. Sathish, G. D’Avino, and A. Q. Shen, ““from the edge to the center”: Viscoelastic migration of particles and cells in a strongly shear-thinning liquid flowing in a microchannel",” *Analytical Chemistry*, vol. 89, no. 24, p. 13146–13159, 2017.

[53] A. R. Kang, S. W. Ahn, S. J. Lee, B. Lee, S. S. Lee, and J. M. Kim, “Medium viscoelastic effect on particle segregation in concentrated suspensions under rectangular microchannel flows,” *Korea-Australia Rheology Journal*, vol. 23, pp. 247–254, dec 2011.

[54] N. Xiang, X. Zhang, Q. Dai, J. Cheng, K. Chen, and Z. Ni, “Fundamentals of elasto-inertial particle focusing in curved microfluidic channels,” *Lab on a Chip*, vol. 16, no. 14, pp. 2626–2635, 2016.

[55] F. Tang, C. Barbacioru, Y. Wang, E. Nordman, C. Lee, N. Xu, X. Wang, J. Bodeau, B. B. Tuch, A. Siddiqui, and et al., “Mrna-seq whole-transcriptome analysis of a single cell,” *Nature Methods*, vol. 6, no. 5, p. 377–382, 2009.

[56] R. J. Kimmerling, G. Lee Szeto, J. W. Li, A. S. Genshaft, S. W. Kazer, K. R. Payer, J. de Riba Borrajo, P. C. Blainey, D. J. Irvine, A. K. Shalek, and et al., “A microfluidic platform enabling single-cell rna-seq of multigenerational lineages,” *Nature Communications*, vol. 7, no. 1, 2016.

[57] P. Huang and D. Joseph, “Effects of shear thinning on migration of neutrally buoyant particles in pressure driven flow of newtonian and viscoelastic fluids,” *Journal of Non-Newtonian Fluid Mechanics*, vol. 90, no. 2-3, p. 159–185, 2000.

[58] F. Del-Giudice, G. D’Avino, M. M. Villone, F. Greco, and P. L. Maffettone, “Particle manipulation through polymer solutions in microfluidic processes,” AIP Publishing LLC, 2015.

[59] F. D. Giudice, S. J. Haward, and A. Q. Shen, “Relaxation time of dilute polymer solutions: A microfluidic approach,” *Journal of Rheology*, vol. 61, pp. 327–337, feb 2017.

[60] J. M. Martel and M. Toner, “Inertial focusing in microfluidics,” *Annual Review of Biomedical Engineering*, vol. 16, pp. 371–396, jul 2014.

[61] A. M. Klein and E. Macosko, “InDrops and drop-seq technologies for single-cell sequencing,” *Lab on a Chip*, vol. 17, no. 15, pp. 2540–2541, 2017.

[62] S. S. Kuntaegowdanahalli, A. A. Bhagat, G. Kumar, and I. Papautsky, “Inertial microfluidics for continuous particle separation in spiral microchannels,” *Lab on a Chip*, vol. 9, no. 20, p. 2973, 2009.

[63] S. Cha, T. Shin, S. S. Lee, W. Shim, G. Lee, S. J. Lee, Y. Kim, and J. M. Kim, “Cell stretching measurement utilizing viscoelastic particle focusing,” *Analytical Chemistry*, vol. 84, no. 23, p. 10471–10477, 2012.

[64] J. Nam, H. Lim, D. Kim, H. Jung, and S. Shin, “Continuous separation of microparticles in a microfluidic channel via the elasto-inertial effect of non-newtonian fluid,” *Lab on a Chip*, vol. 12, no. 7, p. 1347, 2012.

[65] F. Petersson, L. Åberg, A.-M. Swärd-Nilsson, and T. Laurell, “Free flow acoustophoresis: microfluidic-based mode of particle and cell separation,” *Analytical Chemistry*, vol. 79, no. 14, p. 5117–5123, 2007.

[66] N. Pamme and A. Manz, “On-chip free-flow magnetophoresis: continuous flow separation of magnetic particles and agglomerates,” *Analytical Chemistry*, vol. 76, no. 24, p. 7250–7256, 2004.

[67] M. D. Krebs, R. M. Erb, B. B. Yellen, B. Samanta, A. Bajaj, V. M. Rotello, and E. Alsberg, “Formation of ordered cellular structures in suspension via label-free negative magnetophoresis,” *Nano Letters*, vol. 9, no. 5, p. 1812–1817, 2009.

[68] B. Mattix, T. R. Olsen, Y. Gu, M. Casco, A. Herbst, D. T. Simionescu, R. P. Visconti, K. G. Kornev, and F. Alexis, “Biological magnetic cellular spheroids

as building blocks for tissue engineering," *Acta Biomaterialia*, vol. 10, no. 2, p. 623–629, 2014.

[69] F. Lin, F. Baldessari, C. C. Gyenge, T. Sato, R. D. Chambers, J. G. Santiago, and E. C. Butcher, "Lymphocyte electrotaxis in vitro and in vivo," *The Journal of Immunology*, vol. 181, no. 4, p. 2465–2471, 2008.

[70] J. Li and F. Lin, "Microfluidic devices for studying chemotaxis and electrotaxis," *Trends in Cell Biology*, vol. 21, no. 8, p. 489–497, 2011.

[71] J. Li, S. Nandagopal, D. Wu, S. F. Romanuik, K. Paul, D. J. Thomson, and F. Lin, "Activated t lymphocytes migrate toward the cathode of dc electric fields in microfluidic devices," *Lab on a Chip*, vol. 11, no. 7, p. 1298, 2011.

[72] J. Oakey, R. W. Applegate, E. Arellano, D. D. Carlo, S. W. Graves, and M. Toner, "Particle focusing in staged inertial microfluidic devices for flow cytometry," *Analytical Chemistry*, vol. 82, pp. 3862–3867, may 2010.

[73] W. Lee, P. Tseng, and D. Di Carlo, "Microfluidic cell sorting and separation technology," *Microsystems and Nanosystems*, p. 1–14, 2016.

[74] E. W. M. Kemna, R. M. Schoeman, F. Wolbers, I. Vermes, D. A. Weitz, and A. van den Berg, "High-yield cell ordering and deterministic cell-in-droplet encapsulation using dean flow in a curved microchannel," *Lab on a Chip*, vol. 12, no. 16, p. 2881, 2012.

[75] J. Patel, B. Maji, N. S. Moorthy, and S. Maiti, "Xanthan gum derivatives: Review of synthesis, properties and diverse applications," *RSC Advances*, vol. 10, no. 45, p. 27103–27136, 2020.

[76] E. n. Macosko, A. Basu, R. Satija, J. Nemesh, K. Shekhar, M. Goldman, I. Tirosh, A. n. Bialas, N. Kamitaki, E. n. Martersteck, and et al., "Highly parallel genome-wide expression profiling of individual cells using nanoliter droplets," *Cell*, vol. 161, no. 5, p. 1202–1214, 2015.

[77] B. Martel, "Preface," in *Chemical Risk Analysis*, pp. 13–15, Elsevier, 2004.

[78] Y. Zhang, B. Watts, T. Guo, Z. Zhang, C. Xu, and Q. Fang, "Optofluidic device based microflow cytometers for particle/cell detection: A review," *Micromachines*, vol. 7, no. 4, p. 70, 2016.

[79] E. Sollier, M. Masaeli, H. Amini, K. Camacho, N. Doshi, S. Mitragotri, and D. Di Carlo, "Effect of particle shape on inertial focusing," vol. 2, 01 2011.

[80] S. C. Hur, N. K. Henderson-MacLennan, E. R. McCabe, and D. Di Carlo, "Deformability-based cell classification and enrichment using inertial microfluidics," *Lab on a Chip*, vol. 11, no. 5, p. 912, 2011.

[81] G. Segré and A. Silberberg, "Radial particle displacements in poiseuille flow of suspensions," *Nature*, vol. 189, pp. 209–210, jan 1961.

[82] B. Chun and A. J. C. Ladd, "Inertial migration of neutrally buoyant particles in a square duct: An investigation of multiple equilibrium positions," *Physics of Fluids*, vol. 18, p. 031704, mar 2006.

[83] Y. Gou, Y. Jia, P. Wang, and C. Sun, "Progress of inertial microfluidics in principle and application," *Sensors*, vol. 18, p. 1762, jun 2018.

[84] S. Köster, F. E. Angilè, H. Duan, J. J. Agresti, A. Wintner, C. Schmitz, A. C. Rowat, C. A. Merten, D. Pisignano, A. D. Griffiths, and D. A. Weitz, "Drop-based microfluidic devices for encapsulation of single cells," *Lab on a Chip*, vol. 8, no. 7, p. 1110, 2008.

[85] J.-P. Matas, V. Glezer, É. Guazzelli, and J. F. Morris, "Trains of particles in finite-reynolds-number pipe flow," *Physics of Fluids*, vol. 16, pp. 4192–4195, nov 2004.

[86] L.-L. Fan, Q. Yan, J. Zhe, and L. Zhao, "Single particle train ordering in microchannel based on inertial and vortex effects," *Journal of Micromechanics and Microengineering*, vol. 28, p. 065011, apr 2018.

[87] Y.-S. Choi, K.-W. Seo, and S.-J. Lee, "Lateral and cross-lateral focusing of spherical particles in a square microchannel," *Lab Chip*, vol. 11, no. 3, pp. 460–465, 2011.

[88] R. S. Varma and M. Varma, "ChemInform abstract: Alumina-mediated condensation. a simple synthesis of aurones.," *ChemInform*, vol. 24, pp. no–no, aug 2010.

[89] S. Torino, M. Iodice, I. Rendina, G. Coppola, and E. Schonbrun, "Self-hydrodynamic focusing in a parallel microfluidic device," in *2015 XVIII AISEM Annual Conference*, IEEE, feb 2015.

[90] A. A. S. Bhagat, S. S. Kuntaegowdanahalli, N. Kaval, C. J. Seliskar, and I. Papautsky, "Inertial microfluidics for sheath-less high-throughput flow cytometry," *Biomedical Microdevices*, vol. 12, pp. 187–195, nov 2009.

[91] Z. Zhou, Y. Chen, S. Zhu, L. Liu, Z. Ni, and N. Xiang, “Inertial microfluidics for high-throughput cell analysis and detection: a review,” *The Analyst*, vol. 146, no. 20, pp. 6064–6083, 2021.

[92] S. C. Hur, H. T. K. Tse, and D. D. Carlo, “Sheathless inertial cell ordering for extreme throughput flow cytometry,” *Lab Chip*, vol. 10, no. 3, pp. 274–280, 2010.

[93] A. J. Mach and D. D. Carlo, “Continuous scalable blood filtration device using inertial microfluidics,” *Biotechnology and Bioengineering*, vol. 107, pp. 302–311, jun 2010.

[94] M. Robinson, H. Marks, T. Hinsdale, K. Maitland, and G. Coté, “Rapid isolation of blood plasma using a cascaded inertial microfluidic device,” vol. 11, p. 024109, mar 2017.

[95] D. D. Carlo, J. F. Edd, D. Irimia, R. G. Tompkins, and M. Toner, “Equilibrium separation and filtration of particles using differential inertial focusing,” *Analytical Chemistry*, vol. 80, pp. 2204–2211, feb 2008.

[96] W. C. Lee, A. A. S. Bhagat, S. Huang, K. J. V. Vliet, J. Han, and C. T. Lim, “High-throughput cell cycle synchronization using inertial forces in spiral microchannels,” *Lab on a Chip*, vol. 11, no. 7, p. 1359, 2011.

[97] M. E. Warkiani, G. Guan, K. B. Luan, W. C. Lee, A. A. S. Bhagat, P. K. Chaudhuri, D. S.-W. Tan, W. T. Lim, S. C. Lee, P. C. Y. Chen, C. T. Lim, and J. Han, “Slanted spiral microfluidics for the ultra-fast, label-free isolation of circulating tumor cells,” *Lab Chip*, vol. 14, no. 1, pp. 128–137, 2014.

[98] S. Shen, C. Ma, L. Zhao, Y. Wang, J.-C. Wang, J. Xu, T. Li, L. Pang, and J. Wang, “High-throughput rare cell separation from blood samples using steric hindrance and inertial microfluidics,” *Lab Chip*, vol. 14, no. 14, pp. 2525–2538, 2014.

[99] A. Abdulla, W. Liu, A. Gholamipour-Shirazi, J. Sun, and X. Ding, “High-throughput isolation of circulating tumor cells using cascaded inertial focusing microfluidic channel,” *Analytical Chemistry*, vol. 90, pp. 4397–4405, mar 2018.

[100] J. F. Edd, D. Di Carlo, K. J. Humphry, S. Köster, D. Irimia, D. A. Weitz, and M. Toner, “Controlled encapsulation of single-cells into monodisperse picolitre drops,” *Lab on a Chip*, vol. 8, no. 8, pp. 1262–1264, 2008.

[101] J. Young Kim, S. Won Ahn, S. Sik Lee, and J. Min Kim, "Lateral migration and focusing of colloidal particles and dna molecules under viscoelastic flow," *Lab on a Chip*, vol. 12, no. 16, p. 2807, 2012.

[102] F. Tian, W. Zhang, L. Cai, S. Li, G. Hu, Y. Cong, C. Liu, T. Li, and J. Sun, "Microfluidic co-flow of newtonian and viscoelastic fluids for high-resolution separation of microparticles," *Lab on a Chip*, vol. 17, no. 18, p. 3078–3085, 2017.

[103] H. Lim, S. M. Back, M. H. Hwang, D.-H. Lee, H. Choi, and J. Nam, "Sheathless high-throughput circulating tumor cell separation using viscoelastic non-newtonian fluid," *Micromachines*, vol. 10, no. 7, p. 462, 2019.

[104] C. Liu, J. Guo, F. Tian, N. Yang, F. Yan, Y. Ding, J. Wei, G. Hu, G. Nie, J. Sun, and et al., "Field-free isolation of exosomes from extracellular vesicles by microfluidic viscoelastic flows," *ACS Nano*, vol. 11, no. 7, p. 6968–6976, 2017.

[105] I. De Santo, G. D'Avino, G. Romeo, F. Greco, P. A. Netti, and P. L. Maffettone, "Microfluidic lagrangian trap for brownian particles: Three-dimensional focusing down to the nanoscale," *Physical Review Applied*, vol. 2, no. 6, 2014.

[106] A. Karnis and S. G. Mason, "Particle motions in sheared suspensions. XIX. viscoelastic media," *Transactions of the Society of Rheology*, vol. 10, pp. 571–592, sep 1966.

[107] X. Lu, C. Liu, G. Hu, and X. Xuan, "Particle manipulations in non-newtonian microfluidics: A review," *Journal of Colloid and Interface Science*, vol. 500, pp. 182–201, aug 2017.

[108] P. Fischer, "Understanding viscoelasticity - an introduction to rheology (nhan phan-thien)," *Applied Rheology*, vol. 23, no. 6, p. 329–329, 2013.

[109] S. E. Mall-Gleissle, W. Gleissle, G. H. McKinley, and H. Buggisch, "The normal stress behaviour of suspensions with viscoelastic matrix fluids," *Rheologica Acta*, vol. 41, pp. 61–76, jan 2002.

[110] W. R. Schowalter, "Dynamics of polymeric liquids.volume i : Fluid mechanics by r. byron bird, robert c. armstrong, and ole hassager, eds. john wiley; sons, inc., new york, 2nd ed., 1987," *AIChE Journal*, vol. 34, no. 6, p. 1052–1053, 1988.

[111] J. Magda, J. Lou, S. Baek, and K. DeVries, "Second normal stress difference of a boger fluid," *Polymer*, vol. 32, no. 11, p. 2000–2009, 1991.

[112] B. P. Ho and L. G. Leal, "Inertial migration of rigid spheres in two-dimensional unidirectional flows," *Journal of Fluid Mechanics*, vol. 65, no. 2, p. 365–400, 1974.

[113] G. Li, G. H. McKinley, and A. M. Ardekani, "Dynamics of particle migration in channel flow of viscoelastic fluids," *Journal of Fluid Mechanics*, vol. 785, pp. 486–505, nov 2015.

[114] B. P. Ho and L. G. Leal, "Migration of rigid spheres in a two-dimensional unidirectional shear flow of a second-order fluid," *Journal of Fluid Mechanics*, vol. 76, pp. 783–799, aug 1976.

[115] M. A. Tehrani, "An experimental study of particle migration in pipe flow of viscoelastic fluids," *Journal of Rheology*, vol. 40, no. 6, p. 1057–1077, 1996.

[116] M. Villone, G. D'Avino, M. Hulsen, F. Greco, and P. Maffettone, "Particle motion in square channel flow of a viscoelastic liquid: Migration vs. secondary flows," *Journal of Non-Newtonian Fluid Mechanics*, vol. 195, p. 1–8, 2013.

[117] F. Del-Giudice, G. Romeo, G. D'Avino, F. Greco, P. A. Netti, and P. L. Maffettone, "Particle alignment in a viscoelastic liquid flowing in a square-shaped microchannel," *Lab on a Chip*, vol. 13, no. 21, p. 4263, 2013.

[118] H. Lim, J. Nam, and S. Shin, "Lateral migration of particles suspended in viscoelastic fluids in a microchannel flow," *Microfluidics and Nanofluidics*, vol. 17, pp. 683–692, feb 2014.

[119] K. Kang, S. S. Lee, K. Hyun, S. J. Lee, and J. M. Kim, "DNA-based highly tunable particle focuser," *Nature Communications*, vol. 4, oct 2013.

[120] Y.-Q. FAN, M. WANG, F. GAO, J. ZHUANG, G. TANG, and Y.-J. ZHANG, "Recent development of droplet microfluidics in digital polymerase chain reaction," *Chinese Journal of Analytical Chemistry*, vol. 44, pp. 1300–1307, aug 2016.

[121] R. Zilionis, J. Nainys, A. Veres, V. Savova, D. Zemmour, A. M. Klein, and L. Mazutis, "Single-cell barcoding and sequencing using droplet microfluidics," *Nature Protocols*, vol. 12, pp. 44–73, dec 2016.

[122] J. Bageritz and G. Raddi, "Single-cell rna sequencing with drop-seq," *Methods in Molecular Biology*, p. 73–85, 2019.

[123] G. D'Avino and P. L. Maffettone, "Numerical simulations on the dynamics of a particle pair in a viscoelastic fluid in a microchannel: effect of rheology, particle shape, and confinement," *Microfluidics and Nanofluidics*, vol. 23, may 2019.

[124] C. Liu, C. Xue, X. Chen, L. Shan, Y. Tian, and G. Hu, "Size-based separation of particles and cells utilizing viscoelastic effects in straight microchannels," *Analytical Chemistry*, vol. 87, pp. 6041–6048, may 2015.

[125] F. Del-Giudice, G. D'Avino, F. Greco, P. L. Maffettone, and A. Q. Shen, "Fluid viscoelasticity drives self-assembly of particle trains in a straight microfluidic channel," *Physical Review Applied*, vol. 10, dec 2018.

[126] L. Liu, H. Xu, H. Xiu, N. Xiang, and Z. Ni, "Microfluidic on-demand engineering of longitudinal dynamic self-assembly of particles," *The Analyst*, vol. 145, no. 15, pp. 5128–5133, 2020.

[127] X. Hu, P. Lin, J. Lin, Z. Zhu, and Z. Yu, "On the polydisperse particle migration and formation of chains in a square channel flow of non-newtonian fluids," *Journal of Fluid Mechanics*, vol. 936, 2022.

[128] S. M. McFaul, B. K. Lin, and H. Ma, "Cell separation based on size and deformability using microfluidic funnel ratchets," *Lab on a Chip*, vol. 12, no. 13, p. 2369, 2012.

[129] Y. Xie, Z. Mao, H. Bachman, P. Li, P. Zhang, L. Ren, M. Wu, and T. J. Huang, "Acoustic cell separation based on density and mechanical properties," *Journal of Biomechanical Engineering*, vol. 142, no. 3, 2020.

[130] P. Zhu and L. Wang, "Passive and active droplet generation with microfluidics: A review," *Lab on a Chip*, vol. 17, no. 1, p. 34–75, 2017.

[131] M. R. Hamblin and M. Karimi, *Biomedical applications of microfluidic devices*. Academic press.

[132] S. Halldorsson, E. Lucumi, R. Gómez-Sjöberg, and R. M. Fleming, "Advantages and challenges of microfluidic cell culture in polydimethylsiloxane devices," *Biosensors and Bioelectronics*, vol. 63, p. 218–231, 2015.

[133] R. Seemann, M. Brinkmann, T. Pfohl, and S. Herminghaus, "Droplet based microfluidics," *Reports on Progress in Physics*, vol. 75, no. 1, p. 016601, 2011.

[134] D. M. Headen, J. R. García, and A. J. García, "Parallel droplet microfluidics for high throughput cell encapsulation and synthetic microgel generation," *Microsystems & amp; Nanoengineering*, vol. 4, no. 1, 2018.

[135] L. Shang, Y. Cheng, and Y. Zhao, "Emerging droplet microfluidics," *Chemical Reviews*, vol. 117, pp. 7964–8040, may 2017.

[136] L. Amirifar, M. Besanjideh, R. Nasiri, A. Shamloo, F. Nasrollahi, N. R. de Barros, E. Davoodi, A. Erdem, M. Mahmoodi, V. Hosseini, and et al., “Droplet-based microfluidics in biomedical applications,” *Biofabrication*, vol. 14, no. 2, p. 022001, 2022.

[137] Z. Chen, S. Kheiri, E. W. Young, and E. Kumacheva, “Trends in droplet microfluidics: From droplet generation to biomedical applications,” *Langmuir*, vol. 38, no. 20, p. 6233–6248, 2022.

[138] A. n. Klein, L. Mazutis, I. Akartuna, N. Tallapragada, A. Veres, V. Li, L. Peshkin, D. n. Weitz, and M. n. Kirschner, “Droplet barcoding for single-cell transcriptomics applied to embryonic stem cells,” *Cell*, vol. 161, no. 5, p. 1187–1201, 2015.

[139] J. Ma, G. Tran, A. M. Wan, E. W. Young, E. Kumacheva, N. N. Iscove, and P. W. Zandstra, “Microdroplet-based one-step rt-pcr for ultrahigh throughput single-cell multiplex gene expression analysis and rare cell detection,” *Scientific Reports*, vol. 11, no. 1, 2021.

[140] S. Damiati, U. Kompella, S. Damiati, and R. Kodzius, “Microfluidic devices for drug delivery systems and drug screening,” *Genes*, vol. 9, no. 2, p. 103, 2018.

[141] W.-L. Chou, P.-Y. Lee, C.-L. Yang, W.-Y. Huang, and Y.-S. Lin, “Recent advances in applications of droplet microfluidics,” *Micromachines*, vol. 6, no. 9, p. 1249–1271, 2015.

[142] P. Dimitriou, J. Li, G. Tornillo, T. McCloy, and D. Barrow, “Droplet microfluidics for tumor drug-related studies and programmable artificial cells,” *Global Challenges*, vol. 5, no. 7, p. 2000123, 2021.

[143] L. Mazutis, J. Gilbert, W. L. Ung, D. A. Weitz, A. D. Griffiths, and J. A. Heyman, “Single-cell analysis and sorting using droplet-based microfluidics,” *Nature Protocols*, vol. 8, pp. 870–891, apr 2013.

[144] S. L. Sjostrom, Y. Bai, M. Huang, Z. Liu, J. Nielsen, H. N. Joensson, and H. A. Svahn, “High-throughput screening for industrial enzyme production hosts by droplet microfluidics,” *Lab Chip*, vol. 14, no. 4, pp. 806–813, 2014.

[145] S. Santesson, E. Degerman, P. Rorsman, T. Johansson, S. Lemos, and S. Nilsson, “Cell–cell communication between adipocytes and pancreatic cells in acoustically levitated droplets,” *Integrative Biology*, vol. 1, no. 10, p. 595, 2009.

[146] S. Sohrabi, N. kassir, and M. Keshavarz Moraveji, "Droplet microfluidics: Fundamentals and its advanced applications," *RSC Advances*, vol. 10, no. 46, p. 27560–27574, 2020.

[147] A. Shams Khorrami and P. Rezai, "Oscillating dispersed-phase co-flow microfluidic droplet generation: Multi-droplet size effect," *Biomicrofluidics*, vol. 12, no. 3, p. 034113, 2018.

[148] L. Wang, C. Niu, C. Zhang, and Z. Wang, "Steady flow of pressure-driven water-in-oil droplets in closed-open-closed microchannels," *AIP Advances*, vol. 9, no. 12, p. 125040, 2019.

[149] P. He, H. Kim, D. Luo, M. Marquez, and Z. Cheng, "Low-frequency ac electro-flow-focusing microfluidic emulsification," *Applied Physics Letters*, vol. 96, no. 17, p. 174103, 2010.

[150] S.-H. Tan, N.-T. Nguyen, L. Yobas, and T. G. Kang, "Formation and manipulation of ferrofluid droplets at a microfluidict-junction," *Journal of Micromechanics and Microengineering*, vol. 20, no. 4, p. 045004, 2010.

[151] L. Schmid and T. Franke, "Acoustic modulation of droplet size in a t-junction," *Applied Physics Letters*, vol. 104, no. 13, p. 133501, 2014.

[152] J. Azimi-Boulali, M. Madadelahi, M. J. Madou, and S. O. Martinez-Chapa, "Droplet and particle generation on centrifugal microfluidic platforms: A review," *Micromachines*, vol. 11, no. 6, p. 603, 2020.

[153] M. Stacey, J. Stickley, P. Fox, V. Statler, K. Schoenbach, S. Beebe, and S. Buescher, "Differential effects in cells exposed to ultra-short, high intensity electric fields: Cell survival, dna damage, and cell cycle analysis," *Mutation Research/Genetic Toxicology and Environmental Mutagenesis*, vol. 542, no. 1-2, p. 65–75, 2003.

[154] T. Glawdel, C. Elbuken, and C. L. Ren, "Droplet generation in microfluidics," *Encyclopedia of Microfluidics and Nanofluidics*, p. 1–12, 2013.

[155] S. L. Anna, N. Bontoux, and H. A. Stone, "Formation of dispersions using "flow focusing" in microchannels," *Applied Physics Letters*, vol. 82, no. 3, p. 364–366, 2003.

[156] R. Dreyfus, P. Tabeling, and H. Willaime, "Ordered and disordered patterns in two-phase flows in microchannels," *Physical Review Letters*, vol. 90, no. 14, 2003.

[157] C. Cramer, P. Fischer, and E. J. Windhab, “Drop formation in a co-flowing ambient fluid,” *Chemical Engineering Science*, vol. 59, no. 15, p. 3045–3058, 2004.

[158] T. Thorsen, R. W. Roberts, F. H. Arnold, and S. R. Quake, “Dynamic pattern formation in a vesicle-generating microfluidic device,” *Physical Review Letters*, vol. 86, no. 18, p. 4163–4166, 2001.

[159] F. Y. Ushikubo, F. S. Birribilli, D. R. Oliveira, and R. L. Cunha, “Y- and t-junction microfluidic devices: Effect of fluids and interface properties and operating conditions,” *Microfluidics and Nanofluidics*, vol. 17, no. 4, p. 711–720, 2014.

[160] P. Garstecki, M. J. Fuerstman, H. A. Stone, and G. M. Whitesides, “Formation of droplets and bubbles in a microfluidic t-junction—scaling and mechanism of break-up,” *Lab on a Chip*, vol. 6, no. 3, p. 437, 2006.

[161] X.-B. Li, F.-C. Li, J.-C. Yang, H. Kinoshita, M. Oishi, and M. Oshima, “Study on the mechanism of droplet formation in t-junction microchannel,” *Chemical Engineering Science*, vol. 69, no. 1, p. 340–351, 2012.

[162] J. H. Xu, S. W. Li, J. Tan, and G. S. Luo, “Correlations of droplet formation in t-junction microfluidic devices: From squeezing to dripping,” *Microfluidics and Nanofluidics*, vol. 5, no. 6, p. 711–717, 2008.

[163] J. Collins and A. P. Lee, “Control of serial microfluidic droplet size gradient by step-wise ramping of flow rates,” *Microfluidics and Nanofluidics*, vol. 3, no. 1, p. 19–25, 2006.

[164] T. Ward, M. Faivre, M. Abkarian, and H. A. Stone, “Microfluidic flow focusing: Drop size and scaling in pressureversus flow-rate-driven pumping,” *ELECTROPHORESIS*, vol. 26, no. 19, p. 3716–3724, 2005.

[165] M. Saqib, O. B. Şahinoğlu, and E. Y. Erdem, “Alternating droplet formation by using tapered channel geometry,” *Scientific Reports*, vol. 8, no. 1, 2018.

[166] J. Yao, F. Lin, H. Kim, and J. Park, “The effect of oil viscosity on droplet generation rate and droplet size in a t-junction microfluidic droplet generator,” *Micromachines*, vol. 10, no. 12, p. 808, 2019.

[167] J. D. Tice, A. D. Lyon, and R. F. Ismagilov, “Effects of viscosity on droplet formation and mixing in microfluidic channels,” *Analytica Chimica Acta*, vol. 507, no. 1, p. 73–77, 2004.

[168] L. Peng, M. Yang, S.-s. Guo, W. Liu, and X.-z. Zhao, “The effect of interfacial tension on droplet formation in flow-focusing microfluidic device,” *Biomedical Microdevices*, vol. 13, no. 3, p. 559–564, 2011.

[169] K. Shahrivar and F. Del Giudice, “Beating poisson stochastic particle encapsulation in flow-focusing microfluidic devices using viscoelastic liquids,” *Soft Matter*, 2022.

[170] W. Zeng, Z. Tong, X. Shan, H. Fu, and T. Yang, “Monodisperse droplet formation for both low and high capillary numbers in a t-junction microdroplet generator,” *Chemical Engineering Science*, vol. 243, p. 116799, 2021.

[171] X. Li, L. He, Y. He, H. Gu, and M. Liu, “Numerical study of droplet formation in the ordinary and modified t-junctions,” *Physics of Fluids*, vol. 31, no. 8, p. 082101, 2019.

[172] M. DE MENECH, P. GARSTECKI, F. JOUSSE, and H. A. STONE, “Transition from squeezing to dripping in a microfluidic t-shaped junction,” *Journal of Fluid Mechanics*, vol. 595, p. 141–161, 2008.

[173] M. R. Fielden and T. R. Zacharewski, “Challenges and limitations of gene expression profiling in mechanistic and predictive toxicology,” *Toxicological Sciences*, vol. 60, no. 1, p. 6–10, 2001.

[174] Y. Imai, K. Kanie, and R. Kato, “Morphological heterogeneity description enabled early and parallel non-invasive prediction of t-cell proliferation inhibitory potency and growth rate for facilitating donor selection of human mesenchymal stem cells,” *Inflammation and Regeneration*, vol. 42, no. 1, 2022.

[175] Q. Li, Y. Wang, W. Deng, Y. Liu, J. Geng, Z. Yan, F. Li, B. Chen, Z. Li, R. Xia, and et al., “Heterogeneity of cell composition and origin identified by single-cell transcriptomics in renal cysts of patients with autosomal dominant polycystic kidney disease,” *Theranostics*, vol. 11, no. 20, p. 10064–10073, 2021.

[176] S. J. Altschuler and L. F. Wu, “Cellular heterogeneity: Do differences make a difference?,” *Cell*, vol. 141, no. 4, p. 559–563, 2010.

[177] M. Manchia, J. Cullis, G. Turecki, G. A. Rouleau, R. Uher, and M. Alda, “The impact of phenotypic and genetic heterogeneity on results of genome wide association studies of complex diseases,” *PLoS ONE*, vol. 8, no. 10, 2013.

[178] Q. Zhao, A. Eichten, A. Parveen, C. Adler, Y. Huang, W. Wang, Y. Ding, A. Adler, T. Nevins, M. Ni, and et al., “Single-cell transcriptome analyses reveal

endothelial cell heterogeneity in tumors and changes following antiangiogenic treatment," *Cancer Research*, vol. 78, no. 9, p. 2370–2382, 2018.

[179] D. Lambrechts, E. Wauters, B. Boeckx, S. Aibar, D. Nittner, O. Burton, A. Bassez, H. Decaluwé, A. Pircher, K. Van den Eynde, and et al., "Phenotype molding of stromal cells in the lung tumor microenvironment," *Nature Medicine*, vol. 24, no. 8, p. 1277–1289, 2018.

[180] M. Jamal-Hanjani, "Abstract sy39-03: Lung cancer evolution and its prognostic impact," *Cancer Research*, vol. 82, no. 12Supplement, 2022.

[181] L. Keller and K. Pantel, "Unravelling tumour heterogeneity by single-cell profiling of circulating tumour cells," *Nature Reviews Cancer*, vol. 19, no. 10, p. 553–567, 2019.

[182] E. Wolmarans, J. Mellet, M. Ambele, C. Durandt, and M. S. Pepper, "Heterogeneity of cell therapy products," *South African Medical Journal*, vol. 109, no. 8b, p. 24, 2019.

[183] K. Davey, D. Wong, F. Konopacki, E. Kwa, H. Fiegler, and C. R. Sibley, "A flexible microfluidic system for single-cell transcriptome profiling elucidates phased transcriptional regulators of cell cycle," jan 2020.

[184] H. Jayamohan, H. J. Sant, and B. K. Gale, "Applications of microfluidics for molecular diagnostics," in *Microfluidic Diagnostics*, pp. 305–334, Humana Press, nov 2012.

[185] L. Warren, D. Bryder, I. L. Weissman, and S. R. Quake, "Transcription factor profiling in individual hematopoietic progenitors by digital RT-PCR," *Proceedings of the National Academy of Sciences*, vol. 103, pp. 17807–17812, nov 2006.

[186] N. R. Beer, B. J. Hindson, E. K. Wheeler, S. B. Hall, K. A. Rose, I. M. Kennedy, and B. W. Colston, "On-chip, real-time, single-copy polymerase chain reaction in picoliter droplets," *Analytical Chemistry*, vol. 79, pp. 8471–8475, oct 2007.

[187] B. J. Hindson, K. D. Ness, D. A. Masquelier, P. Belgrader, N. J. Heredia, A. J. Makarewicz, I. J. Bright, M. Y. Lucero, A. L. Hiddessen, T. C. Legler, T. K. Kitano, M. R. Hodel, J. F. Petersen, P. W. Wyatt, E. R. Steenblock, P. H. Shah, L. J. Bousse, C. B. Troup, J. C. Mellen, D. K. Wittmann, N. G. Erndt, T. H. Cauley, R. T. Koehler, A. P. So, S. Dube, K. A. Rose, L. Montesclaros, S. Wang, D. P. Stumbo, S. P. Hodges, S. Romine, F. P. Milanovich, H. E. White, J. F. Regan, G. A. Karlin-Neumann, C. M. Hindson, S. Saxonov, and B. W. Colston, "High-throughput droplet digital pcr system for absolute quantitation of dna copy number," *Analytical Chemistry*, vol. 83, no. 22, pp. 8604–8610, 2011.

[188] S. Battat, D. A. Weitz, and G. M. Whitesides, "Nonlinear phenomena in microfluidics," *Chemical Reviews*, vol. 122, no. 7, pp. 6921–6937, 2022.

[189] J. Nunes, S. Tsai, J. Wan, and H. A. Stone, "Dripping and jetting in microfluidic multiphase flows applied to particle and fibre synthesis," *Journal of physics D: Applied physics*, vol. 46, no. 11, p. 114002, 2013.

[190] E. W. Kemna, R. M. Schoeman, F. Wolbers, I. Vermes, D. A. Weitz, and A. Van Den Berg, "High-yield cell ordering and deterministic cell-in-droplet encapsulation using dean flow in a curved microchannel," *Lab on a Chip*, vol. 12, no. 16, pp. 2881–2887, 2012.

[191] A. Abate, A. Poitzsch, Y. Hwang, J. Lee, J. Czerwinska, and D. Weitz, "Impact of inlet channel geometry on microfluidic drop formation," *Physical Review E*, vol. 80, no. 2, p. 026310, 2009.

[192] A. J. Chung, D. R. Gossett, and D. D. Carlo, "Three dimensional, sheathless, and high-throughput microparticle inertial focusing through geometry-induced secondary flows," *Small*, vol. 9, pp. 685–690, nov 2012.

[193] M. Cho, S. O. Hong, S. H. Lee, K. Hyun, and J. M. Kim, "Effects of ionic strength on lateral particle migration in shear-thinning xanthan gum solutions," *Micromachines*, vol. 10, p. 535, aug 2019.

[194] G. D'Avino, F. Greco, and P. L. Maffettone, "Particle migration due to viscoelasticity of the suspending liquid and its relevance in microfluidic devices," *Annual Review of Fluid Mechanics*, vol. 49, pp. 341–360, jan 2017.

[195] "The deborah number," *Physics Today*, sep 2011.

[196] A. B. Metzner, J. L. White, and M. M. Denn, "Constitutive equations for viscoelastic fluids for short deformation periods and for rapidly changing flows: Significance of the deborah number," *AIChE Journal*, vol. 12, pp. 863–866, sep 1966.

[197] G. D'Avino, T. Tuccillo, P. Maffettone, F. Greco, and M. Hulsen, "Numerical simulations of particle migration in a viscoelastic fluid subjected to shear flow," *Computers & Fluids*, vol. 39, pp. 709–721, apr 2010.

[198] K.-W. Song, Y.-S. Kim, and G.-S. Chang, "Rheology of concentrated xanthan gum solutions: Steady shear flow behavior," *Fibers and Polymers*, vol. 7, no. 2, p. 129–138, 2006.

[199] R. H. Ewoldt, M. T. Johnston, and L. M. Caretta, “Experimental challenges of shear rheology: How to avoid bad data,” in *Complex Fluids in Biological Systems*, pp. 207–241, Springer New York, oct 2014.

[200] W. P. Cox and E. H. Merz, “Correlation of dynamic and steady flow viscosities,” *Journal of Polymer Science*, vol. 28, pp. 619–622, apr 1958.

[201] N. B. Wyatt and M. W. Liberatore, “Rheology and viscosity scaling of the polyelectrolyte xanthan gum,” *Journal of Applied Polymer Science*, vol. 114, no. 6, p. 4076–4084, 2009.

[202] A. Jeyasountharan, G. D’Avino, and F. Del Giudice, “Confinement effect on the viscoelastic particle ordering in microfluidic flows: Numerical simulations and experiments,” *Physics of Fluids*, vol. 34, no. 4, p. 042015, 2022.

[203] F. Del Giudice, “Simultaneous measurement of rheological properties in a microfluidic rheometer,” *Physics of Fluids*, vol. 32, no. 5, p. 052001, 2020.

[204] F. D. Giudice and C. Barnes, “Rapid temperature-dependent rheological measurements of non-newtonian solutions using a machine-learning aided microfluidic rheometer,” *Analytical Chemistry*, vol. 94, pp. 3617–3628, feb 2022.

[205] E. Dressaire and A. Sauret, “Clogging of microfluidic systems,” *Soft Matter*, vol. 13, no. 1, p. 37–48, 2017.

[206] J. J. Higdon and G. P. Muldowney, “Resistance functions for spherical particles, droplets and bubbles in cylindrical tubes,” *Journal of Fluid Mechanics*, vol. 298, p. 193–210, 1995.

[207] D. Yuan, Q. Zhao, S. Yan, S.-Y. Tang, G. Alici, J. Zhang, and W. Li, “Recent progress of particle migration in viscoelastic fluids,” *Lab on a Chip*, vol. 18, no. 4, pp. 551–567, 2018.

[208] X. Qiu, J.-H. Huang, T. M. Westerhof, J. A. Lombardo, K. M. Henrikson, M. Pennell, P. P. Pourfard, E. L. Nelson, P. Nath, J. B. Haun, and et al., “Microfluidic channel optimization to improve hydrodynamic dissociation of cell aggregates and tissue,” *Scientific Reports*, vol. 8, no. 1, 2018.

[209] H. Amini, W. Lee, and D. Di Carlo, “Inertial microfluidic physics,” *Lab on a Chip*, vol. 14, no. 15, p. 2739, 2014.

[210] W. Mao and A. Alexeev, “Hydrodynamic sorting of microparticles by size in ridged microchannels,” *Physics of Fluids*, vol. 23, no. 5, p. 051704, 2011.

[211] M. He, J. S. Edgar, G. D. Jeffries, R. M. Lorenz, J. P. Shelby, and D. T. Chiu, "Selective encapsulation of single cells and subcellular organelles into picoliter- and femtoliter-volume droplets," *Analytical Chemistry*, vol. 77, no. 6, p. 1539–1544, 2005.

[212] R. Tewhey, J. B. Warner, M. Nakano, B. Libby, M. Medkova, P. H. David, S. K. Kotsopoulos, M. L. Samuels, J. B. Hutchison, J. W. Larson, and et al., "Microdroplet-based pcr enrichment for large-scale targeted sequencing," *Nature Biotechnology*, vol. 27, no. 11, p. 1025–1031, 2009.

[213] E. Brouzes, M. Medkova, N. Savenelli, D. Marran, M. Twardowski, J. B. Hutchison, J. M. Rothberg, D. R. Link, N. Perrimon, M. L. Samuels, and et al., "Droplet microfluidic technology for single-cell high-throughput screening," *Proceedings of the National Academy of Sciences*, vol. 106, no. 34, p. 14195–14200, 2009.

[214] L. Mazutis, J. Gilbert, W. L. Ung, D. A. Weitz, A. D. Griffiths, and J. A. Heyman, "Single-cell analysis and sorting using droplet-based microfluidics," *Nature Protocols*, vol. 8, no. 5, p. 870–891, 2013.

[215] A. Farahinia, W. Zhang, and I. Badea, "Circulating tumor cell separation of blood cells and sorting in novel microfluidic approaches: A review," 2020.

[216] Z. Cao, F. Chen, N. Bao, H. He, P. Xu, S. Jana, S. Jung, H. Lian, and C. Lu, "Droplet sorting based on the number of encapsulated particles using a solenoid valve," *Lab Chip*, vol. 13, no. 1, p. 171–178, 2013.

[217] J. Clausell-Tormos, D. Lieber, J.-C. Baret, A. El-Harrak, O. J. Miller, L. Frenz, J. Blouwolff, K. J. Humphry, S. Köster, H. Duan, and et al., "Droplet-based microfluidic platforms for the encapsulation and screening of mammalian cells and multicellular organisms," *Chemistry & Biology*, vol. 15, no. 5, p. 427–437, 2008.

[218] H. Saleh, M. Annuar, and K. Simarani, "Ultrasound degradation of xanthan polymer in aqueous solution: Its scission mechanism and the effect of NaCl incorporation," *Ultrasonics Sonochemistry*, vol. 39, pp. 250–261, nov 2017.

[219] Q. Chen, J. Li, Y. Song, B. Chen, D. M. Christopher, and X. Li, "Pressure-driven microfluidic droplet formation in newtonian and shear-thinning fluids in glass flow-focusing microchannels," *International Journal of Multiphase Flow*, vol. 140, p. 103648, 2021.

[220] W. Du, T. Fu, Q. Zhang, C. Zhu, Y. Ma, and H. Z. Li, "Breakup dynamics for droplet formation in a flow-focusing device: Rupture position of viscoelastic thread from matrix," *Chemical Engineering Science*, vol. 153, pp. 255–269, 2016.

[221] M. Fatehifar, A. Revell, and M. Jabbari, "Non-newtonian droplet generation in a cross-junction microfluidic channel," *Polymers*, vol. 13, no. 12, p. 1915, 2021.

[222] Y. Ren, Z. Liu, and H. C. Shum, "Breakup dynamics and dripping-to-jetting transition in a newtonian/shear-thinning multiphase microsystem," *Lab on a Chip*, vol. 15, no. 1, pp. 121–134, 2015.

[223] B. Rostami and G. L. Morini, "Generation of newtonian and non-newtonian droplets in silicone oil flow by means of a micro cross-junction," *International Journal of Multiphase Flow*, vol. 105, pp. 202–216, 2018.

[224] V.-L. Wong, K. Loizou, P.-L. Lau, R. S. Graham, and B. N. Hewakandamby, "Numerical studies of shear-thinning droplet formation in a microfluidic t-junction using two-phase level-set method," *Chemical Engineering Science*, vol. 174, pp. 157–173, 2017.

[225] K. Shahrivar and F. D. Giudice, "Controlled viscoelastic particle encapsulation in microfluidic devices," *Soft Matter*, vol. 17, no. 35, pp. 8068–8077, 2021.

[226] D. J. Collins, A. Neild, A. DeMello, A.-Q. Liu, and Y. Ai, "The poisson distribution and beyond: methods for microfluidic droplet production and single cell encapsulation," *Lab on a Chip*, vol. 15, no. 17, pp. 3439–3459, 2015.

[227] R. H. Colby, "Structure and linear viscoelasticity of flexible polymer solutions: comparison of polyelectrolyte and neutral polymer solutions," *Rheologica acta*, vol. 49, no. 5, pp. 425–442, 2010.

[228] M. Serhatlioglu, Z. Isiksacan, M. Özkan, D. Tuncel, and C. Elbuken, "Electro-viscoelastic migration under simultaneously applied microfluidic pressure-driven flow and electric field," *Analytical Chemistry*, vol. 92, no. 10, p. 6932–6940, 2020.

[229] B. G. Chung, K.-H. Lee, A. Khademhosseini, and S.-H. Lee, "Microfluidic fabrication of microengineered hydrogels and their application in tissue engineering," *Lab on a Chip*, vol. 12, no. 1, pp. 45–59, 2012.

[230] A. Lashkaripour, C. Rodriguez, N. Mehdipour, R. Mardian, D. McIntyre, L. Ortiz, J. Campbell, and D. Densmore, "Machine learning enables design automa-

tion of microfluidic flow-focusing droplet generation," *Nature communications*, vol. 12, no. 1, pp. 1–14, 2021.